# Vortex Formation Resulting from Solitary Wave Interaction With a Breakwater

by

Dorlisa L. Hommel, James T. Kirby and Fengyan Shi

RESEARCH REPORT NO. CACR-01-03
July, 2001

Center for Applied Coastal Research
Ocean Engineering Laboratory
University of Delaware
Newark, DE 19716

# Acknowledgments

This work was supported by the Army Research Office, Terrestrial Sciences Program, Grant DAAG55-98-1-0173 and the Office of Naval Research, Base Enhancement Program, Grant N00014-97-1-0283.

**Abstract**

A solitary wave which interacts with a vertical breakwater at a normal angle of incidence results in the formation and shedding of a single vortex. In the present study, experiments were conducted which involved generating a solitary wave in a long, narrow, uniform depth wave flume which propagated past a thin, vertical, breakwater. Both velocity and surface elevation data were collected. A numerical Boussinesq model with Smagorinsky subgrid mixing was then employed to simulate the experimental data. Comparisons of the model data to the experimental data revealed the capability of the model to simulate wave-induced vorticies.

# Contents

# List of Figures

# Chapter 1

# INTRODUCTION

A single solitary wave, interacting at normal incidence with a structure, in particular a vertical wall, which extends half way across the width of the tank, results in the formation of a single vortex which is subsequently shed from the structure and propagates downstream. Figure 1.1 shows the formation of a vortex from experiments conducted in the present study resulting from this type of interaction. The ability to numerically model this phenomenon with increasing accuracy is important for a number of reasons. Measurement of the strength of the vortex (the magnitude of the velocities in the vortex) is important because the energy that is required for vortex formation corresponds to a loss of energy from the incident wave. This may have important consequences i.e. for waves entering a harbor, as suggested by Liu (1984). Both the magnitude of the vortex and whether or not the vortex persists in the generation region or moves away from the structure may have significant consequences. One possible consequence is that the area surrounding the structure may suffer from notable erosion depending upon both the residence time and strength of the vortex. Sumer and Fredsøe (1996) conducted a study to investigate the effect of regular waves interacting with a vertical breakwater on the scour occurring at the head of the breakwater. They found that the major flow structures which cause scour are vortices and that only one lee-wake vortex forms at the tip of the breakwater in each half cycle of the waves. They consider a vertical wall which has a round head and they note that the scour is increased when the head shape is changed to a sharp-edged one which is the type used in the present study. Additionally, this type of study may provide useful information for improving the design of breakwaters.

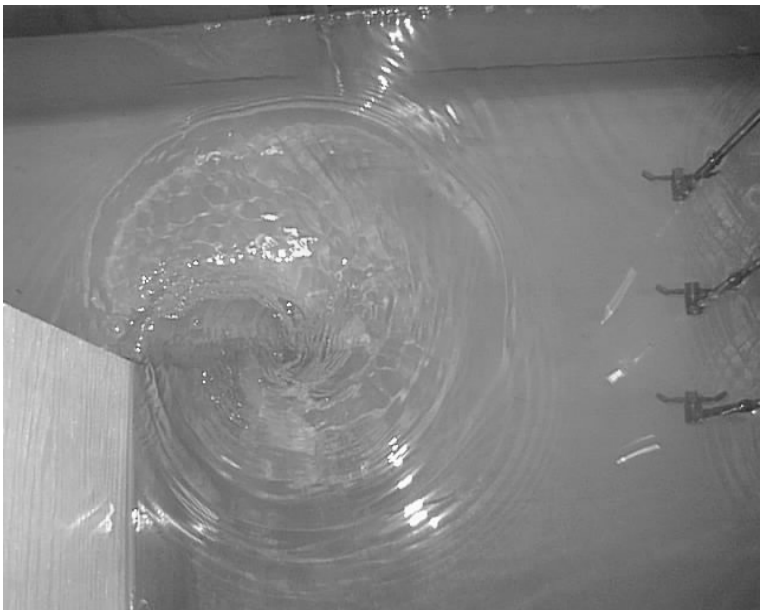

Figure 1.1: Vortex formed during the experiments.

## 1.1 Boussinesq Modeling of Solitary Waves

The Boussinesq equations describe nonlinear, longwave motion under the assumption that the waves are both weakly nonlinear and weakly dispersive. The parameter used to measure the degree of nonlinearity is $\delta = H/h$ and for weakly nonlinear motions $\delta << 1$. Dispersion is measured by the parameter $\mu^2 = (kh)^2$ and for weakly dispersive phenomena $\mu^2 << 1$. The Ursell number ($U_r = \delta/\mu^2$) is used to relate the the degree of nonlinearity to the degree of dispersion of the wave motion and has a value of $U_r = O(1)$ for the standard Boussinesq equations (Wei et al., 1995). The Boussinesq equations have been used to model wave transformation for a range of depths because of their ability to represent shoaling, refraction, diffraction, and reflection. There are, generally speaking, two classes of Boussinesq models (Madsen and Schäffer, 1999). The first class of models are developed using Laplace's equation. Mei and Méhauté (1966) and Mei (1983) conducted several of the studies which followed this approach. Wu (1981) developed a two equation Boussinesq model from Laplace's equations, assuming an inviscid, incompressible fluid of uniform density. The two equation model expresses mass continuity in terms of $\eta$ and the momentum equation, written using Bernoulli's equation, in terms of the velocity potential $\phi$. Because the velocity potential was used in the derivation the fluid is irrotational. It will be shown in a subsequent chapter that

no vorticity could be generated or advected using this type of model. Nwogu (1993) also derived a set of Boussinesq equations from Laplace's equations and the horizontal velocity at an arbitrary depth was used as the dependent variable. Subsequently, Wei et al. (1995) derived a set of fully nonlinear Boussinesq equations in terms of the velocity potential following the approach of Nwogu (1993). A depth specific velocity was used as the dependent variable in their derivations. Full nonlinearity was obtained in the boundary conditions and the resulting equations had improved linear dispersion properties in intermediate depth water and were no longer limited to small nonlinearity. The strongly nonlinear portions of the numerical solution, i.e. wave evolution near wave breaking, show significantly improved predictions of wave heights as compared to the weakly nonlinear Boussinesq model developed by Nwogu (1993).

The second class of models were developed using Euler's equations of motion. Peregrine (1967) derived a set of equations in two dimensions which were valid for variable water depth. The model was applied to a solitary wave approaching a beach having a uniform slope. Peregrine used the depth averaged velocity in his derivations. Mei and Méhauté (1966) used the bottom velocity as the dependent variable and applied this set of equations to long waves over an uneven bottom. Abbott et al. (1984) alternatively derived the Boussinesq equations using the volume flux instead of the depth-averaged velocity as the dependent variable. The model is applied to the simulation of short wave propagation in shallow water.

The Boussinesq equations were initially only applicable to shallow water depths. Witting (1984) developed a model which used a set of equations to describe mass flux (in terms of the surface elevation and vertically averaged velocity), the equation of motion and the kinematic surface condition (both in terms of the surface elevation, surface slope, and surface velocities). A longwave expansion of linear theory took the solution to fourth order accuracy in $k^2h_o^2$ which was higher order than Boussinesq theories so both shallow water and deep water waves could then be incorporated into the model. No test of wave propagation from deep water to shallow water was carried out in this study, however. The model was developed into a one dimensional model in order to be able to implement a fast, fully vectorized numerical algorithm. Inspired by Witting's work, Madsen et al. (1991) developed a two dimensional model based on the system of equations derived by Abbott (1984) using the depth integrated velocity as the dependent variable. Comparisons are first made between phase and group velocities computed using $\overline{U}$, $U_s$, $U_b$, and expanded forms of $\overline{U}$ and $U_s$ by Witting

(1984). The phase and group velocities were expressed in terms of a constant, $B$, by the following

$$\frac{c^2}{gh} = \frac{1 + Bk^2h^2}{1 + (B + \frac{1}{3})k^2h^2} \tag{1.1}$$

and

$$c_g = c[1 + \frac{Bk^2h^2}{1 + Bk^2h^2} - \frac{(B + \frac{1}{3})k^2h^2}{1 + (B + \frac{1}{3})k^2h^2}] \tag{1.2}$$

Comparisons of these constants from the phase velocity relation (Figure 1.2) were plotted as determined from each of the four methods. $B$ values of -1/3, 0, 1/15, 1/6 correspond to using $U_s$, $\overline{U}$, Pade's expansion, and $U_b$, respectively. Witting's approach was shown to give the best comparison to Stokes theory. Figure 1.3 shows a comparison of the constant, $B$, from the group velocity relation based on derivations from the four studies. Subsequently, in their derivation of the Boussinesq equations, Madsen et al. (1991) showed how $B$ could be utilized as a curve fitting parameter in order to obtain the best comparison of the phase velocities to Stokes theory. Based on their choice of $B$, the new equations incorporate notably improved phase velocities for linear waves in water depths up to and beyond the deep water limit (see Figure 1.4). The model was able to simulate the propagation of irregular wave trains traveling from deep water to shallow water. As mentioned previously, Nwogu (1993) developed a set of Boussinesq equations using the horizontal velocity at an abitrary depth as the dependent variable. By letting the velocity variable be close to middepth it was determined that the dispersive properties were significantly improved. An important consequence is that the improvement allows this set of equations to be applicable to a greater depth range.

Subsequently, Wei and Kirby (1995) developed a numerical model based on Nwogu's equations. They use a fourth order predictor-corrector scheme for time stepping. The addition of a discretization of the first-order spatial derivatives to fourth-order accuracy allowed for the elimination of error terms which are of the same form as the dispersive terms. They applied the numerical model to solitary wave propagation over a uniform depth and found that the wave height and shape remained stable over a long distance without undergoing any damping or evolution, indicative of dissipative effects that are negligible or non-existent.

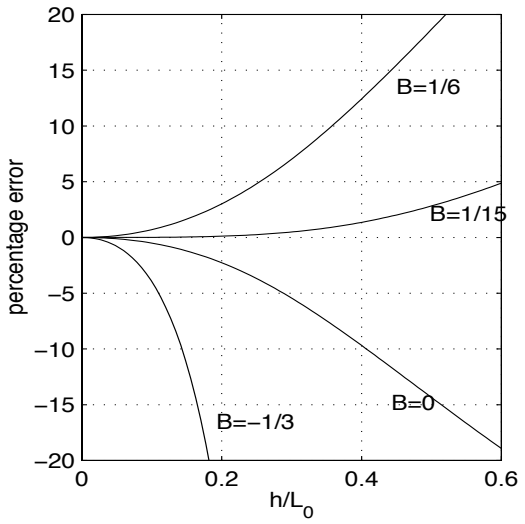


Figure 1.2: Comparison of the constant B from the phase velocity relative to Stokes theory, i.e. $100(c - c_{Stokes})/c_{Stokes}$. B values of -1/3, 0, 1/15, 1/6 correspond to using $U_s$, $\overline{U}$, Pade's expansion, and $U_b$, respectively. Equations used to generate the figure are from Madsen et al. (1991).

Chen et al. (1999) investigated a rip current system using the theory for the fully nonlinear Boussinesq equations developed by Wei et al. (1995). Additional terms were added to the governing equations to account for wave breaking, shoreline run-up, subgrid turbulent mixing, and bottom friction.

More recently, Shi et al. (2000) developed a numerical model in generalized curvilinear coordinates based on the theory derived by Wei et al. (1995). An extra term was included in the governing equations, which had the same form as used in Chen et al. (1999), to account for subgrid turbulent mixing.

## 1.2 Solitary Wave Interactions with a Vertical Wall

Solitary waves propagating past a semi-infinite vertical wall at a normal angle of incidence have been studied both numerically and experimentally for a range of parameters, domain shapes, and domain sizes.

Perroud (1957) conducted experiments in a constant water depth wave tank with water maintained at a depth of 0.061 $m$. The experiments consisted of generating a solitary wave both obliquely and normally incident on a vertical wall extending a

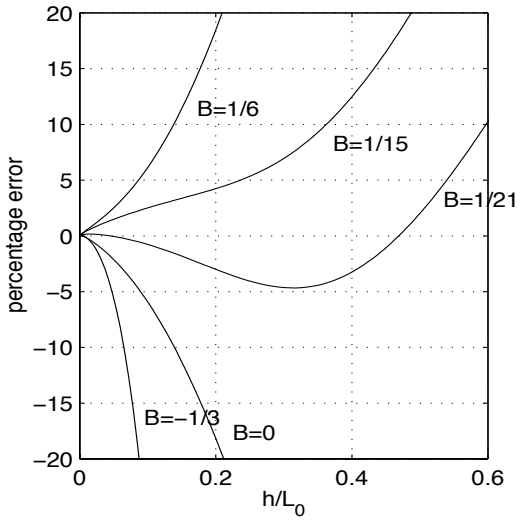


Figure 1.3: Comparison of the constant B from the group velocity relative to Stokes theory, i.e. $100(c_g - c_{g,Stokes})/c_{g,Stokes}$. B values of -1/3, 0, 1/15, 1/6 correspond to using $U_s$, $\overline{U}$, Pade's expansion, and $U_b$, respectively. Equations used to generate the figure are from Madsen et al. (1991).

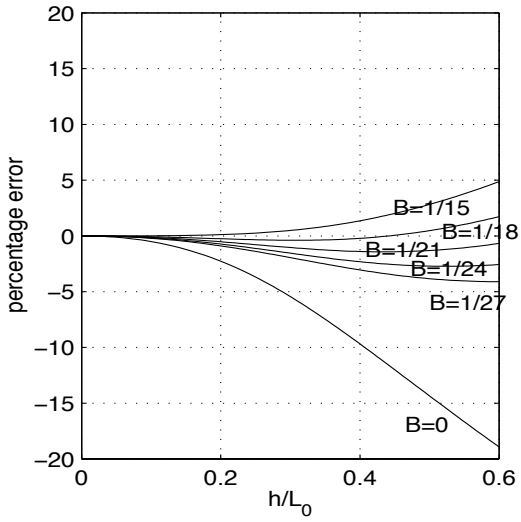


Figure 1.4: Comparison of the constant B from the phase velocity relative to Stokes theory, i.e. $100(c - c_{Stokes})/c_{Stokes}$, for various selected values for B. Equations used to generate the figure are from Madsen et al. (1991).

fraction of the distance across the tank. The wall used in the tank was .008 $m$ thick and had a round tip. Two across-tank gap spacings (the distance between the wall tip and the opposite side of the tank) were studied, .254 $m$ and .508 $m$, and a range of wave height to water depth ratios of 0.2 to 0.58 were used. A clockwise rotating vortex was reported to have formed and the orientation of this vortex is illustrated by a schematic in Figure 1.5. The strength of the vortex was not measured. As explained earlier, the strength refers to the magnitude of the velocities in the vortex. An approximation of 0.0127 $m$ was given as the depression of the surface elevation in the center of the vortex for a wave amplitude of $a = 0.0274$ $m$.

Liu (1984) also conducted experiments of a solitary wave impinging on a wall at both normal and oblique angles of incidence. Liu (1984) studied the diffraction of solitary waves by comparing results from a theoretical model which was developed based on linear diffraction theory to the results of his laboratory experiments. Good agreement was obtained between the model results and the corresponding experimental results for incident and reflective wave heights. Some discrepancies were found in the surface elevations between model and experimental results. It was suggested that these are attributed to wave diffraction effects and frictional losses and that this discrepancy is most significant in the 'shadow zone', the region downstream of the structure. Although a vortex was observed to have formed near the tip of the breakwater in the experiments, this was not considered as a possible source of energy loss from the incident wave. The numerical model is not capable of simulating a vortex because it's development is based upon potential flow theory. The strength of the vortex was not measured in this study.

Wang (1993) numerically modeled the interaction of a solitary wave with a wall at both normal and oblique angles of incidence. The model used was the two equation model Boussineq developed by Wu (1981). An investigation of solitary wave diffraction, reflection, and transmission was carried out in this study, however, vortex formation was not examined because the model generates potential flow and, therefore, no vorticity could be generated. They found that their model produced surface elevations which were comparable to Liu's (1984) experimental data. It will be shown that the numerical model used in the present study generates surface elevations which improve the predictions of $\eta$ relative to Liu's (1984) results.

Roddier and Ertekin (1999) developed a numerical model based on the theory

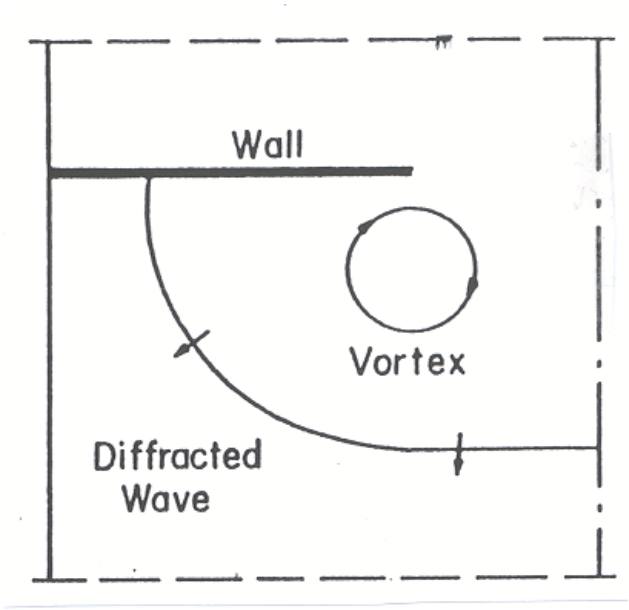


Figure 1.5: Clockwise rotating vortex formed during experiments by Perroud. From Perroud (1957).

developed by Wu and applied the model to solitary wave propagation along the length of a vertical structure. The solitary wave is diffracted when it reaches the tip of the structure and a 'bathtub' vortex is described to form at the tip (Figure 1.6). The vortex in this case was actually a singularity which formed as the potential flow turns the corner sharply. The 'vortex' in this case is not a physical circulation feature.

## 1.3 Objectives of the Present Study

In the present study, experiments were conducted which involved a solitary wave propagating along a uniform depth wave flume past a vertical wall. Two different wave heights were considered in the experiments. As the wave propagates past the wall structure a vortex forms (Figure 1.1) is shed from the structure, and subsequently propagates away from the structure. The strength of the vortex was measured as well as the magnitude and shape of the solitary wave. The numerical model developed by Shi, et al. (2000) was then employed to simulate the experiments. Several model parameters such as wave height and tank geometry were based on the experiments.

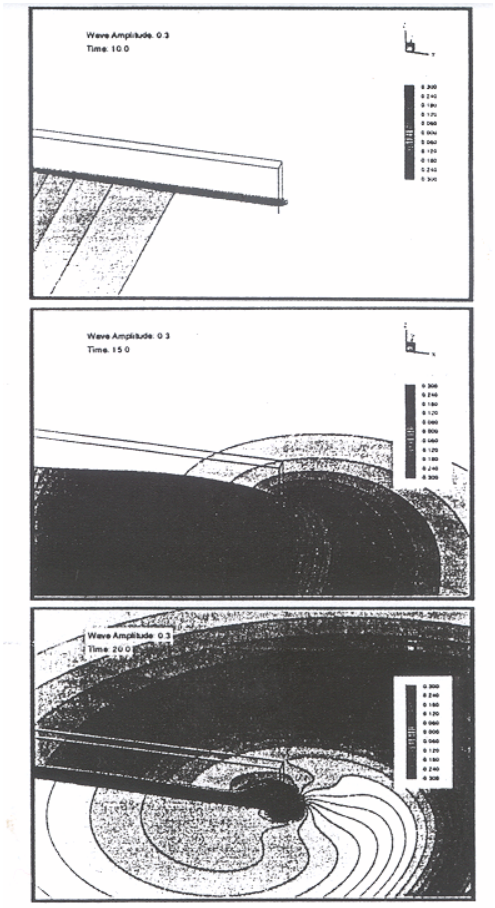


Figure 1.6: "Bathtub vortex" formed due to a singularity occurring at the tip of the wall (from Roddier et al. (1999).

## 1.4 Outline of Thesis

In the following chapter an explanation is given of both the experimental setup and the experiments conducted. A description of the numerical model utilized in the present study is then provided. Several tests were carried out and the descriptions of these and their results are presented. In Chapter 3 the results of both the experiments and model are given and comparisons are made between the two data sets. Chapter 4 contains a discussion of the results and comparisons are made to previous works. The final chapter provides conclusions to the study.

# Chapter 2

# METHODS

The first part of this study consisted of a series of experiments which were carried out at The Center for Applied Coastal Research. The second part of this study consisted of the implementation of a numerical model to attempt to simulate the experimental results. A description of the experimental setup, procedure, and experimental tests will be given followed by a description of the numerical model along with the numerical tests carried out for this study.

## 2.1 Experimental Setup and Procedure

Experiments were conducted in the wave flume which had a length of approximately 25 $m$, a width of .6 $m$, and a height of .77 $m$. Figure 2.1 shows a photograph taken, with a digital Epson camera, of the tank where the experiments took place. A water depth of .30 $m$ was used for all experiments. A vertical wall extending half-way across the tank was constructed and placed at the midway point along the length of the tank, 12.4 $m$ from the wavemaker. Figure 2.2 shows the experimental setup with the vertical wall extending from the right side of the tank to the center of the tank and the instrumentation attached to the carriages beyond the breakwater. The structure was composed of 1.9 $cm$ thick plywood which had a width of .30 $m$ and a height extending above the top of the tank. Figure 2.3 (a) shows a simplistic schematic plan view of the wave flume.

Solitary waves were generated with a piston-type wave paddle using the following equation taken from Goring (1978)

$$\xi(t) = \frac{H}{kh} \int_0^{\theta} f(w)dw \tag{2.1}$$

where $\xi$ is the trajectory along which the wavemaker plate moves, $w$ is the dummy variable of integration, and

$$\theta = k(ct - \xi) \tag{2.2}$$

$$c = (g(h + H))^{1/2} \tag{2.3}$$

$$k = (\frac{3H}{4h^3})^{1/2} \tag{2.4}$$

and for solitary wave generation

$$f(\theta) = 1/\cosh^2\theta \tag{2.5}$$

To solve this equation for $\theta$, for a given time step, the relation for $\theta$ is substituted into equation 2.1 and differentiated with respect to $\theta$. Then using Newton's rule,

$$\theta_{i+1} = \theta_i - \frac{F(\theta_i)}{F_\theta(\theta_i)} \tag{2.6}$$

where $F_\theta = \frac{\partial F}{\partial \theta}$, the solution is given by

$$\theta_{i+1} = \theta_i - \frac{(\theta_i - kct + \frac{H}{h}tanh(\theta_i))}{(1 + \frac{H}{h}(1/\cosh(\theta_i)^2))} \tag{2.7}$$

where $t$ is in seconds.

The wave paddle and data collection were controlled and synchronized using several computers. The duration of each experiment varied but was approximately 10 s. Each experiment was conducted approximately 20-30 min. apart to allow for the fluid surface in the tank to calm down completely. The sampling rate for the wave gages was 20 Hz.

Two sets of experimental data were collected. For the first set of data an average solitary wave height of 5.48 $cm$ was used and for the second set of experiments an average wave height of 10.3 $cm$ was used.

Eight wave gages were set up to measure the temporal changes in the free surface elevation. The gages were calibrated once each day. A total of nineteen data points were used for the calibration of each gage. During the calibration procedure the gages were automatically raised and lowered to known depths by 1 $cm$ increments and the wire of each gage is correspondingly emerged and submerged for calibration. In general the calibration data followed a straight line and the coefficients were obtained from the least squares error fit to the data points. The linear calibration curves, of volts to $cm$, were generated for all gages with the slope and intercept. For each data set 512 data points were collected at a sampling rate of 20 $Hz$.

The data in units of volts was then converted to units of length (specifically $cm$) using the algorithm

$$\eta = p_1 f + p_2 \tag{2.8}$$

where $f$ is the data, in volts, to be converted and $p_1$ and $p_2$ are the linear regression coefficients. Gage 3 was located in front of the structure and was used as the location for matching up the model data with the experimental data. When the wave crest passed gage 3 this was marked in the time series as $t = 0$ and the corresponding location in the model data was marked as $t = 0$ in that time series. In this way the two times series could be aligned with one another. Because gage 3 was stationary throughout all of the wave experiments, the data from multiple data runs could be aligned with one another as well. The remaining gages were located behind the structure.

In the experiments, the gages held by the moving carriage, highlighted by the red rectangle in Figure 2.3 (b) for $H = 5.48$ $cm$ are gages 1, 2, and 4, while gages 3, 5, and 6 are fixed in their location in the tank throughout the experiments. For the small wave height case there were three gages attached to the nearest carriage to the structure. The red rectangle indicates the carriage which was moved during each of the experiments and the arrow indicates the direction of motion of the carriage. This carriage was moved in between each experiment (by 2 $cm$ up to a distance of 37 $cm$ from the structure and then by 5 $cm$ increments to a distance of 62 $cm$ from the structure) to create a 'mapping' of the surface elevation and velocity data sets.

For the large wave height case there were five gages attached to the mobile carriage nearest to the structure and the remainder of the gages were fixed in location for all of the experiments. The gages on the moving carriage for the case of $H = 10.3\ cm$ are gages 1, 7, 2, 8, and 4, while gages 3, 5, and 6 are fixed in position and these positions are indicated by $x's$ in Figure 2.4 (b). The red rectangle indicates the mobile carriage and the arrow indicates the direction of motion of the carriage, the same as for the small wave height case. The carriage was moved by increments of 2 $cm$ up to a distance of 39 $cm$ from the structure and then by increments of 5 $cm$ up to a distance of 69 $cm$ from the structure.

Three Sontek acoustic doppler velocimeters (ADV) were used to measure the velocity field. These were fastened onto the front of the moving carriage for both the small and large wave height cases and these locations are indicated in Figures 2.3 (b) and 2.4 (b), respectively by circles. A transducer sends two pulses of sound separated by a time lag. The receivers face towards the transmitter so that the receive beam patterns are directed 30° towards the transmitter beam, having a focus at 5 $cm$ in front of the transmitter. The sampling volume is defined as this focus region where the receive beam patterns cross. As the transmitted acoustic pulse passes through the sampling volume the energy is scattered in all directions by the particles present in the water. The receivers then measure the phase of the return signal from the portion of reflected energy of each pulse. The velocity of the particles in the water is directly proportional to the change in phase divided by the time between pulses. The sampling rate for the ADV's was 20 Hz, the same as for the wave gages.

## 2.2 Repeatability

By moving the gages down the tank between experiments, an array of data locations is generated to allow for a mapping of the area where vortex formation and advection occurs, that is, near the structure location. Figures 2.3 (c) and 2.4 (c) show the resulting data arrays generated for the small and large wave height cases.

In order to use this entire array of data locations as one unit it is necessary to show that the experiments are repeatable to within some reasonably small level of error. One wave gage and one ADV gage were placed in a fixed location in the tank and a solitary wave with an average height of 10.3 $cm$ was generated 10 times. The surface elevation and the $u$ and $v$ velocity components were measured. From this data

means and standard deviations were computed for each point in the time series. The means (with the standard deviations shown in red) of these computations are shown in Figure 2.5 for gage 3 located upstream of the structure, gage 1 located downstream of the structure and the velocity components taken at the location of gage 1. Because the error levels for all three data components are fairly small, the experiments then are considered to be repeatable within this level of error.

## 2.3 Numerical Model

In the second part of this study a numerical model was applied to several cases of solitary wave generation. In each experiment conducted, the actual wave height generated varied by up to several tenths of a $cm$, so an average wave height from ten waves generated in the tank was used as the incident wave height in the numerical model. The average of the wave heights was determined to be $H = 5.48\ cm$ for the small wave height case and $H = 10.3\ cm$ for the large wave height case. The numerical model employed was developed by Shi et al. (2000).

### 2.3.1 Model Description

The numerical model employed in this study was developed by Shi et al. (2000) and is based on the fully nonlinear Boussinesq equations derived by Wei et al. (1995). The model equations are derived in curvilinear coordinates and include a term to account for subgrid turbulent mixing following the work of Chen et al. (1999). After tranformation to a curvilinear coordinate system the model equations become very complex expressions and the contravariant component method is used for mathematical simplification of the system of equations. Details on the contravariant component method as it is used in this model as well as details of the numerical method beyond what is provided below are given in Shi et al. (2000).

The fully nonlinear Boussinesq equations written in cartesian coordinates, as expressed by Chen et al. (1999) (excluding terms for shoreline run-up and wave breaking) in terms of a reference elevation, $z_\alpha$, and reference velocity, $\vec{u} = (u, v)$, are given by the following forms for mass conservation

$$\eta_t + \nabla \cdot \vec{M} = 0 \tag{2.9}$$

where $\eta$ is the surface elevation and $\vec{M}$ is the mass flux given by

$$\begin{aligned} \vec{M} &= (h+\eta)\vec{u} + (h+\eta)[\frac{z_\alpha^2}{2} - \frac{1}{6}(h^2 - h\eta + \eta^2)]\nabla(\nabla \cdot \vec{u}) \\ &+ (h+\eta)[z_\alpha + \frac{1}{2}(h-\eta)]\nabla[\nabla \cdot (h\vec{u})] \end{aligned} \tag{2.10}$$

and momentum

$$\vec{u}_t + (\vec{u} \cdot \nabla)\vec{u} + g\nabla\eta + \vec{V_1} + \vec{V_2} + \vec{R_s} = 0 \tag{2.11}$$

where $g$ is gravitational acceleration and $\vec{V_1}$ and $\vec{V_2}$ are the dispersive Boussinesq terms

$$\vec{V_1} = \frac{z_\alpha^2}{2}\nabla(\nabla \cdot \vec{u}_t) + z_\alpha\nabla[\nabla \cdot (h\vec{u}_t)] - \nabla[\frac{1}{2}\eta^2\nabla \cdot \vec{u}_t + \eta\nabla \cdot (h\vec{u}_t)] \tag{2.12}$$

$$\vec{V_2} = \nabla[(z_\alpha - \eta)(\vec{u}\cdot\nabla)[\nabla\cdot(h\vec{u})] + \frac{1}{2}(z_\alpha^2 - \eta^2)(\vec{u}\cdot\nabla)(\nabla\cdot\vec{u})] + \frac{1}{2}\nabla[\nabla \cdot (h\vec{u}) + \eta\nabla \cdot \vec{u}]^2 \tag{2.13}$$

The last term, $\vec{R_s}$, is an expression representing the subgrid mixing to account for the eddy viscosity of the underlying flow. This expression is implemented similarly to that of Chen et al. (1999) and the $x$ and $y$ components are given by

$$R_s^x = \frac{1}{h+\eta}[(\nu_s[(h+\eta)u_\alpha]_x)_x + \frac{1}{2}(\nu_s[(h+\eta)u_\alpha]_y + \nu_s[(h+\eta)v_\alpha]_x)_y] \tag{2.14}$$

$$R_s^y = \frac{1}{h+\eta}[\frac{1}{2}(\nu_s[(h+\eta)v_\alpha]_x + \nu_s[(h+\eta)u_\alpha]_y)_x + (\nu_s[(h+\eta)v_\alpha]_y)_y] \tag{2.15}$$

here $\nu_s$ is the eddy viscosity due to the subgrid turbulence and is given by

$$\nu_s = c_m \triangle x \triangle y[(U_x)^2 + (V_y)^2 + \frac{1}{2}(U_y + V_x)^2]^{\frac{1}{2}} \tag{2.16}$$

where $\triangle x$ and $\triangle y$ are the grid spacing in the $x$ and $y$ directions, respectively and $c_m$ is a constant mixing coefficient.

A series of numerical tests were conducted using a one dimensional version of the numerical model. A uniform grid was used and the grid domain had a solid boundary at the end opposite to the side where wave generation occured. The maximum runup height was measured as the wave reflected off of the solid boundary. Tests were run for three incident wave heights ($H = 3$, 6, and 10 $cm$) and three mixing coefficients ($c_m = 0$, 3, and 10). A plot of the runup height vs. incident wave height for the three values of mixing coefficients is shown in Figure 2.6. Plotted along with the model results are data values obtained from experiments which were conducted by Chan and Street (1970) and these data values are indicated in the figure. For the range of mixing coefficients tested, the model results correlate well with the experimental data plotted. It is clear that for the range of mixing coefficients tested that there is no discernable effect on the numerical solution for small incident wave heights. For larger incident wave heights the deviation in the numerical solution is negligible. A mixing coefficient of 10 was ultimately used for all of the numerical simulations because this choice resulted in the best physical behavior.

The contravariant component method was used to transform the system of equations because the kinematical lateral boundary conditions are more easily obtained. The system of equations for mass conservation written in tensor-invariant forms which are derived using a contravariant basis method have the form

$$\eta_t + \frac{1}{\sqrt{g_0}}\frac{\partial}{\partial x^k}(\sqrt{g_0 M^k}) = 0 \tag{2.17}$$

with $M$ expressed as

$$\begin{aligned} M^k &= (h+\eta)u^k + (h+\eta)[\frac{z_\alpha^2}{2} - \frac{1}{6}(h^2 - h\eta + \eta^2)][\frac{1}{\sqrt{g_0}}\frac{\partial}{\partial x^l}(\sqrt{g_0}u^l)]\!!^k & (2.18)\\ &+ (h+\eta)[z_\alpha + \frac{1}{2}(h-\eta)][\frac{1}{\sqrt{g_0}}\frac{\partial}{\partial x^l}(\sqrt{g_0}hu^l)]\!!^k & (2.19)\end{aligned}$$

and the momentum equation becomes

$$\frac{\partial u^k}{\partial t} + g\eta!\!!^k + u^l u^k_{,l} + V_1^k + V_2^k + R_s^k = 0 \tag{2.20}$$

with tensors

$$V_1^k = \frac{z_\alpha^2}{2}[\frac{1}{\sqrt{g_0}}\frac{\partial}{\partial x^l}(\sqrt{g_0}hu_t^l)]!^k \tag{2.21}$$

$$+ \; z_\alpha[\frac{1}{\sqrt{g_0}}\frac{\partial}{\partial x^l}(\sqrt{g_0}hu_t^l)]!^k \tag{2.22}$$

$$- \; [\frac{\eta^2}{2\sqrt{g_0}}\frac{\partial}{\partial x^l}(\sqrt{g_0}u_t^l) + \frac{\eta}{\sqrt{g_0}}\frac{\partial}{\partial x^l}(\sqrt{g_0}hu_t^l)]!^k \tag{2.23}$$

$$V_2^k = (z_\alpha - \eta)u^l\frac{\partial}{\partial x^l}[\frac{1}{\sqrt{g_0}}\frac{\partial}{\partial x^m}(\sqrt{g_0}hu^m)]!^k \tag{2.24}$$

$$+ \; \frac{1}{2}(z_\alpha^2 - \eta^2)u^l\frac{\partial}{\partial x^l}[\frac{1}{\sqrt{g_0}}\frac{\partial}{\partial x^m}(\sqrt{g_0}u^m)]!^k \tag{2.25}$$

$$+ \; \frac{1}{2}([\frac{1}{\sqrt{g_0}}\frac{\partial}{\partial x^l}(\sqrt{g_0}hu^l) + \frac{\eta}{\sqrt{g_0}}\frac{\partial}{\partial x^l}(\sqrt{g_0}u^l)]^2)!^k \tag{2.26}$$

where here the indices for $k, l$ and $m$ are 1 and 2, $(u^1, u^2) = (U, V), (x^1, x^2) = (\xi_1, \xi_2)$, $\frac{\partial}{\partial x_k}$ is the partial derivative, $()_k$ indicates the covariant spatial derivative, and $!^k$ represents the contravariant spatial derivative and is defined by

and

$$R_s^k = \frac{1}{h+\eta}T_{,l}^{kl} \tag{2.27}$$

where

$$\vec{T} = \frac{1}{2}(h+\eta)\nu[\nabla\vec{u} + (\nabla\vec{u})^T] \tag{2.28}$$

Here $\nu$ is the diffusion coefficient and $\vec{T}$ represents the stress tensor.

$$f!^k = \frac{\partial f}{\partial x^i}g^{ik} \tag{2.29}$$

where $g^{ik}$ is the contravariant basis.

A staggered grid system is used in the transformed image domain and the time integration was performed using a fourth-order Adams-Bashforth-Moulton predictor-

corrector scheme. There is a fourth-order discretization of the first-order spatial derivatives by the use of the standard five-point finite-differencing, and a second-order discretization of the dispersive terms. This accuracy ensures that the truncation error does not include terms which are mathematically similar to the actual dispersive terms (Shi et al.,2000).

F. Shi (personal communication) demonstrated that this numerical model shows improved prediction of the surface elevation over the model by Liu (1984) when compared with experimental data collected by Liu (1984). Figure 2.7 shows the data for two stations, station A which is located in a wave tank upstream of a breakwater and station B which is located in the 'shadow zone', downstream of the breakwater. The figure shows data from Liu's experiments, results from Liu's linear theory, and results using the model developed by Shi et al. (2000). It is clear that model results using the numerical model developed by Shi et al. (2000) provide an improved prediction of the surface elevation as compared to the linear theory (Hommel et al., 2000).

### 2.3.2 Model Grid

The numerical model was developed for a generalized curvilinear grid which is staggered in the transformed image domain. The Figure 2.10 shows an example of this which is the stretched grid utilized by the model in the present study. The purpose of using a stretched grid is to allow for higher resolution around the region where the structure is located while, at the same time, maintaining computational efficiency. The range of grid resolutions used was from 1.9 $cm$ to 7.6 $cm$. The grid varies linearly in $x$ only and this stretching is described by

$$x_i = x_{i-1} + .076 - s_i \tag{2.30}$$

where $x_i$ is in meters and $s_i$ is the stretch factor defined by

$$s_i = (i - l1)(.00114) \tag{2.31}$$

for $x < 12.42\ m$ and

$$s_i = (l2 - i)(.00114) \tag{2.32}$$

for $x > 12.42\ m$. The variable $l1$ ($l2$) is the grid point in the $x$ direction where the stretching begins (ends) and $i$ is the iteration number from grid point to grid point. In the present study $l1 = 131$ and $l2 = 283$. A plot of $x_i$ is given in Figure 2.8. Grid points less than 131 and greater than 181 have a $dx$ of 7.6 $cm$ and grid points in the range of 131-181 have a $dx$ of 1.9 $cm$ so there is a uniform, fine grid resolution in the vicinity of the structure. There are discontinuities in the grid spacing in the $x$ dimension of the grid. A plot of the change in the grid resolution is shown in Figure 2.8. The model was tested to ensure that the numerical solution was consistent when either the uniform or variable grids were used. The model was run using the uniform grid and the stretched grid and the numerical solutions were plotted together and are displayed in Figure 2.9. The geometry of the uniform grid is illustrated in Figure 2.11. It is clear from the figure that the solutions are consistent using either grid type.

### 2.3.3 Model Parameters

Several model parameters were largely determined by the experiments. The fluid depth in the numerical model was .3 $m$ and the structure representing the vertical wall in the tank had a width of .3 $m$ and a thickness of one grid point (1.9 $cm$). This is equivalent to the physical thickness of the wall. The Courant number was held constant (=0.180) throughout all of the experiments and was calculated based on the finest grid resolution used in the model grid which was 1.9 $cm$. The breakwater structure is located at $x = 12.42\ m$. The model grid dimensions are $406 \times 32$.

### 2.3.4 Test For Convergence

A series of model runs were carried out for the purpose of testing convergence of the numerical model, to examine the effect of different grid resolutions on the numerical solution. Tests were run for grid spacings of 0.076 $cm$, 0.038 $cm$, and 0.019 $cm$. Results from these tests are shown in Figure 2.12 for $t = 0\ s$ and $t = 5.28\ s$. From these results it is clear that there is no significant variation in the numerical solution for all three cases. The larger grid spacing was included in the test for the purpose of determining the extent to which the model grid could be stretched.

### 2.3.5 Vortex Formation

The vorticity in the fluid is obtained by taking the curl of the momentum equation

$$\nabla \times [\vec{u}_t + (\vec{u} \cdot \nabla)\vec{u} + g\nabla\eta + \vec{V_1} + \vec{V_2} + \vec{R_s}] = 0 \tag{2.33}$$

This gives

$$\frac{\partial \Omega}{\partial t} + (\vec{u} \cdot \nabla)\Omega = -(\Omega \cdot \nabla)\vec{u} + \nabla \times \vec{R_s} + \nabla \times \vec{V_1} + \nabla \times \vec{V_2} \tag{2.34}$$

where

$$\vec{\Omega} = \nabla \times \vec{u} \tag{2.35}$$

is the vorticity vector and is oriented vertically and $\nabla \times \vec{R_s}$ contains the eddy viscosity term while $(\vec{u} \cdot \nabla)\vec{\Omega}$ represents the advection of vorticity and comes from taking the curl of the advective acceleration term in the momentum equation. The term $-(\Omega \cdot \nabla)\vec{u}$ represents vortex stretching. The complete form of the advective acceleration may be expressed as

$$(\vec{u} \cdot \nabla)\vec{u} = \frac{1}{2}\nabla(\vec{u} \cdot \vec{u}) - \vec{u} \times \vec{\Omega} \tag{2.36}$$

If the form of the advective acceleration is $\frac{1}{2}\nabla(\vec{u} \cdot \vec{u})$, as in some models, then the curl of this term looks like

$$\nabla \times (\frac{1}{2}\nabla(\vec{u} \cdot \vec{u})) = 0 \tag{2.37}$$

and no advection and stretching of vorticity results. A more thorough investigation of this subject is given by Gobbi et al. (2000). The form of the advective acceleration which allows for the advection of vorticity is $(\vec{u} \cdot \nabla)\vec{u}$ and not $\frac{1}{2}\nabla(\vec{u} \cdot \vec{u})$. The eddy viscosity allows for separation of the fluid and it is this process of fluid separation which (in the present study occurs at the tip of the breakwater) is the source for vorticity. Therefore, in order to numerically simulate the phenomena of vortex formation and advection it is necessary to have both the source of the vorticity (fluid separation) and the advective acceleration in the correct form.

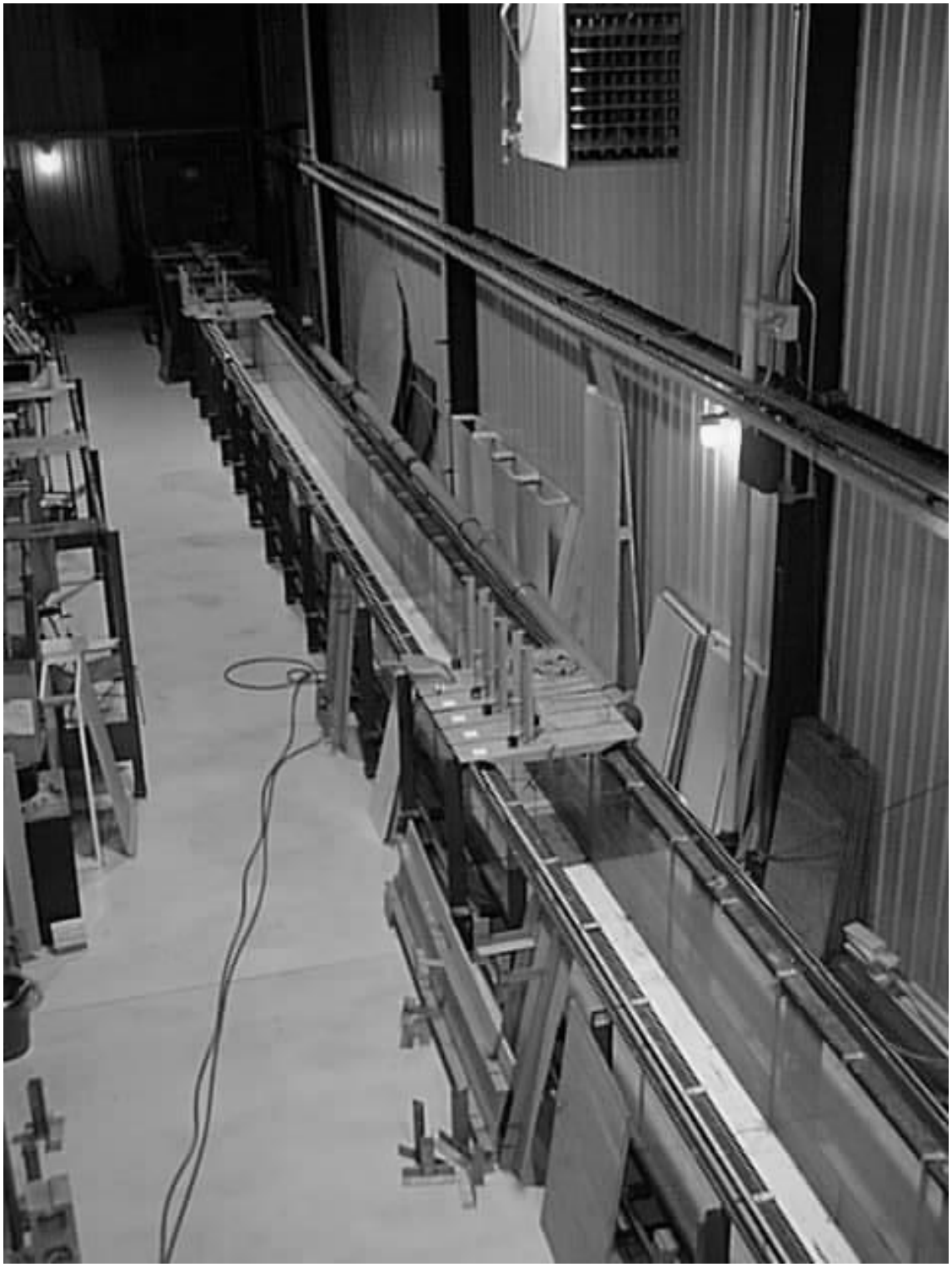

Figure 2.1: Digital photograph showing the wave flume at CACR used for the experiments.

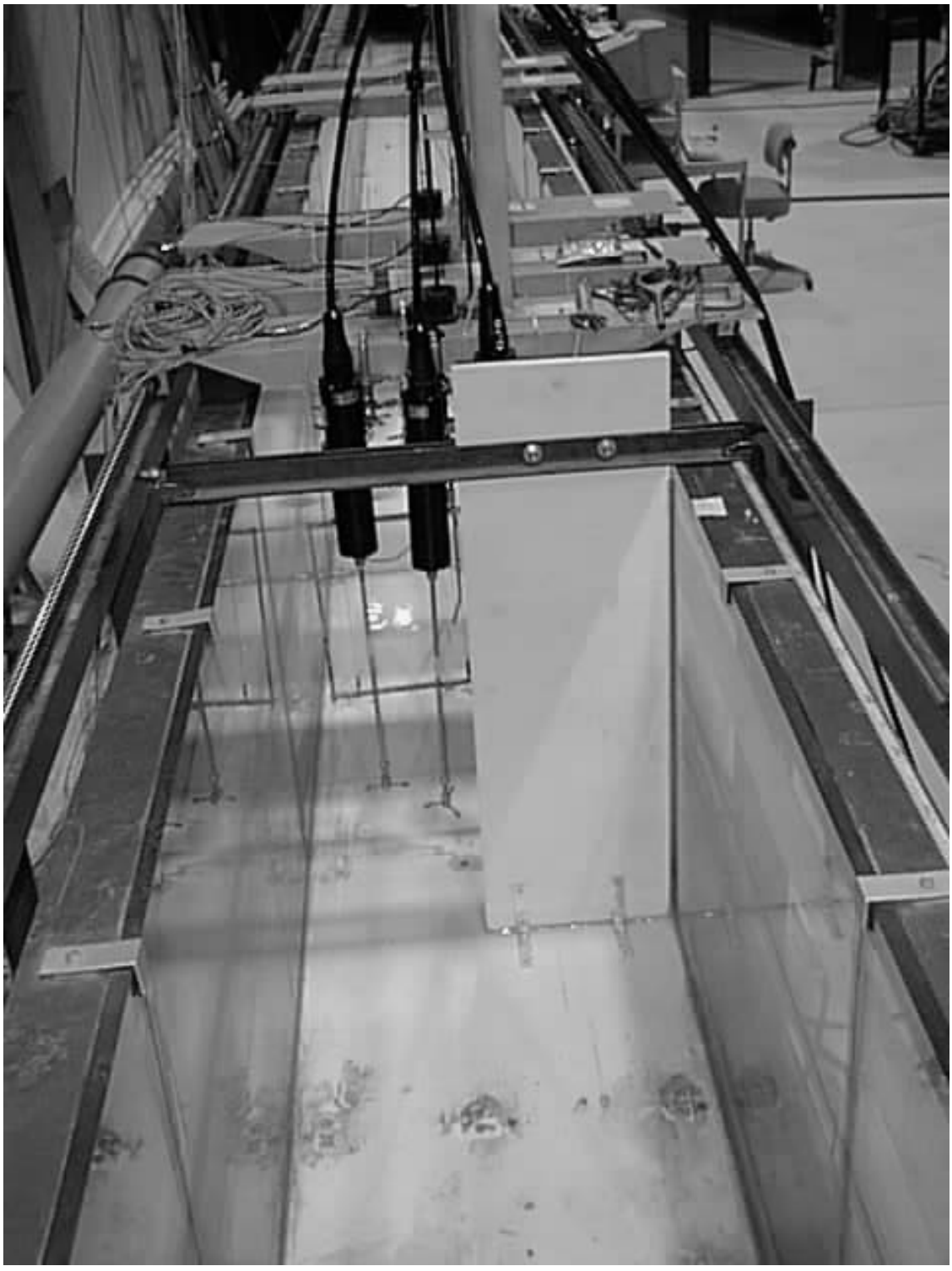

Figure 2.2: Digital photograph showing the breakwater and instrument setup.

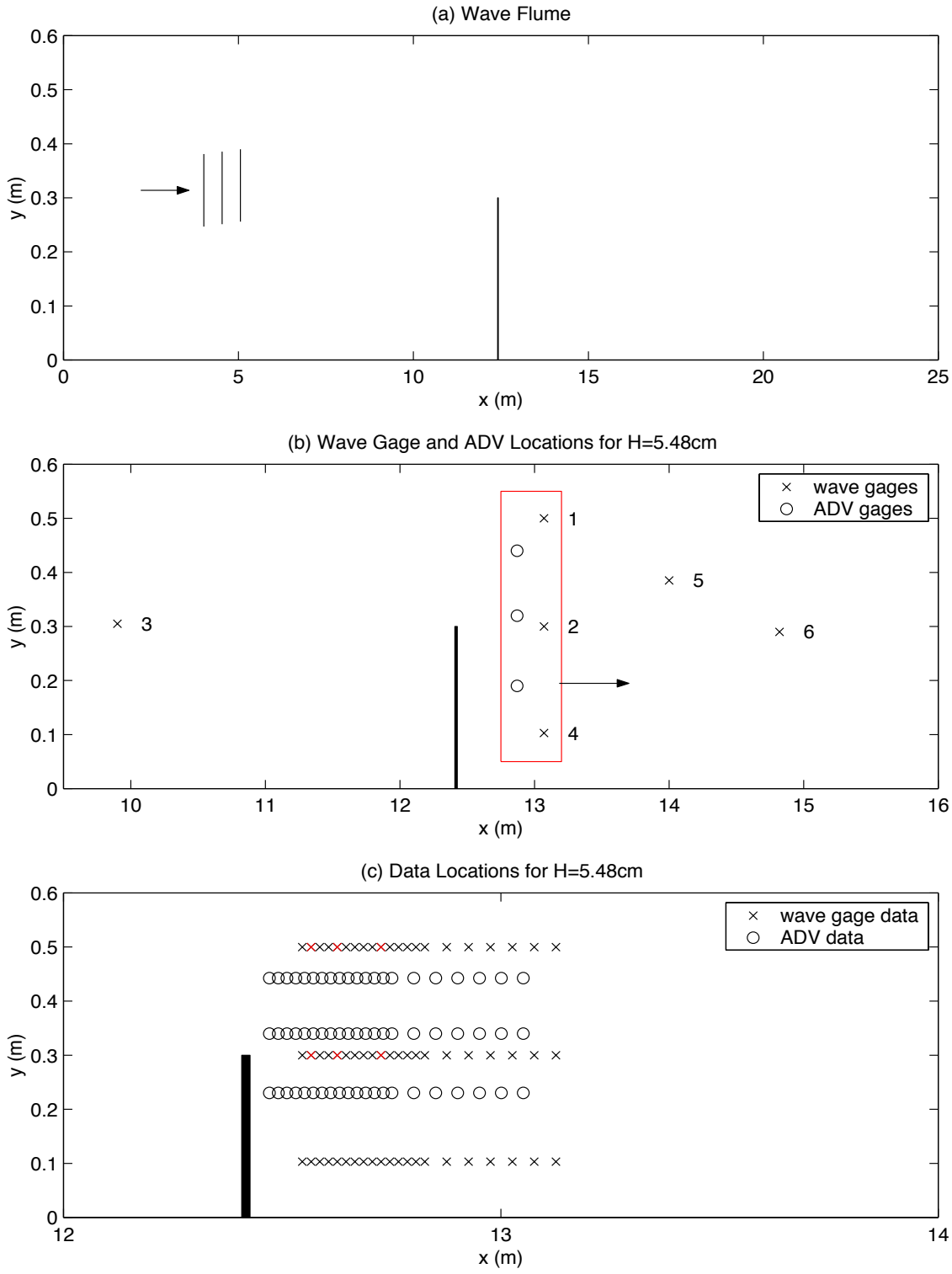


Figure 2.3: (a) Wave flume, (b) gage locations, and (c) data locations for $H = 5.48\,cm$.

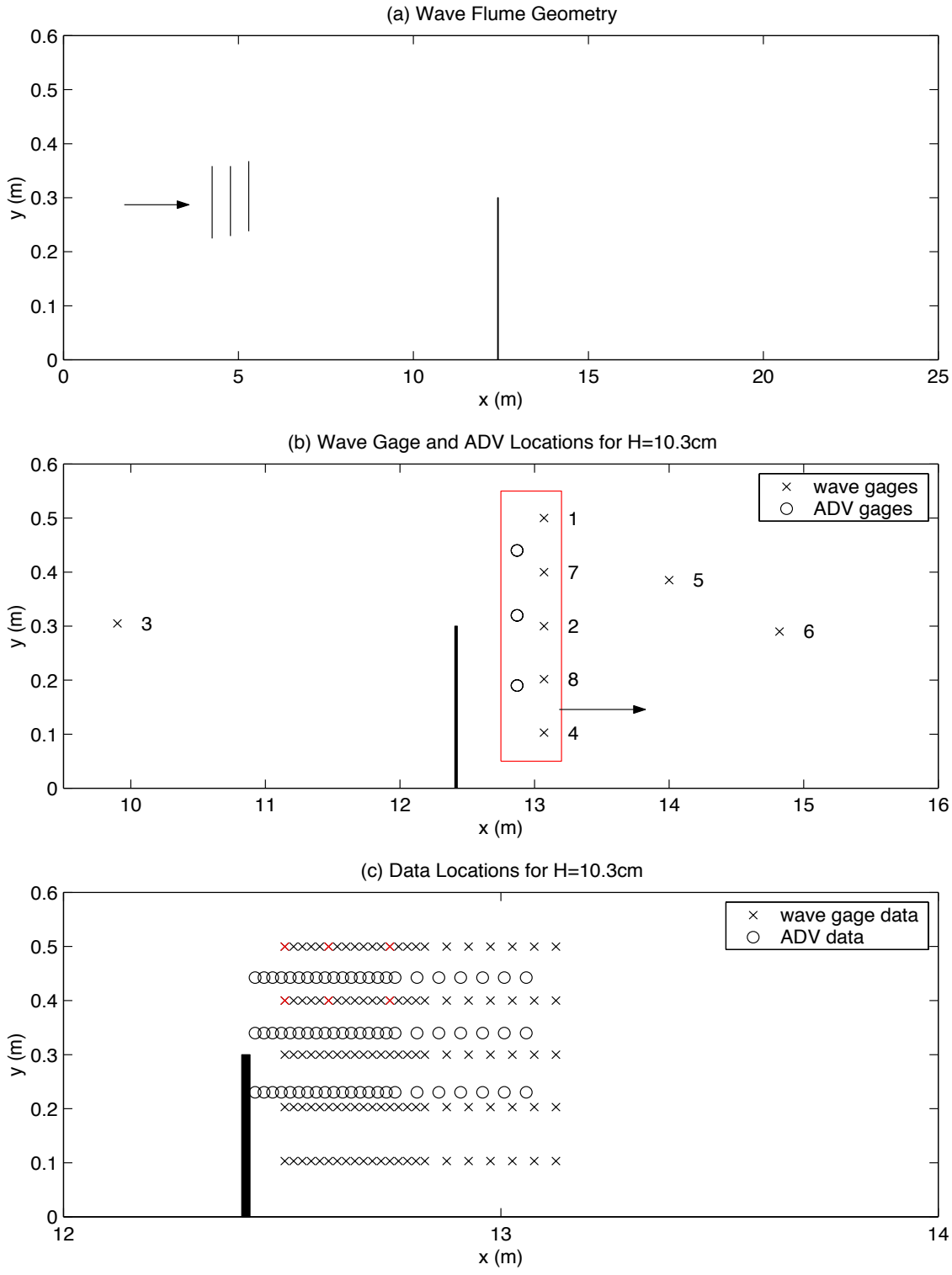


Figure 2.4: (a) Wave flume, (b) gage locations, and (c) data locations for $H = 10.3\,cm$.

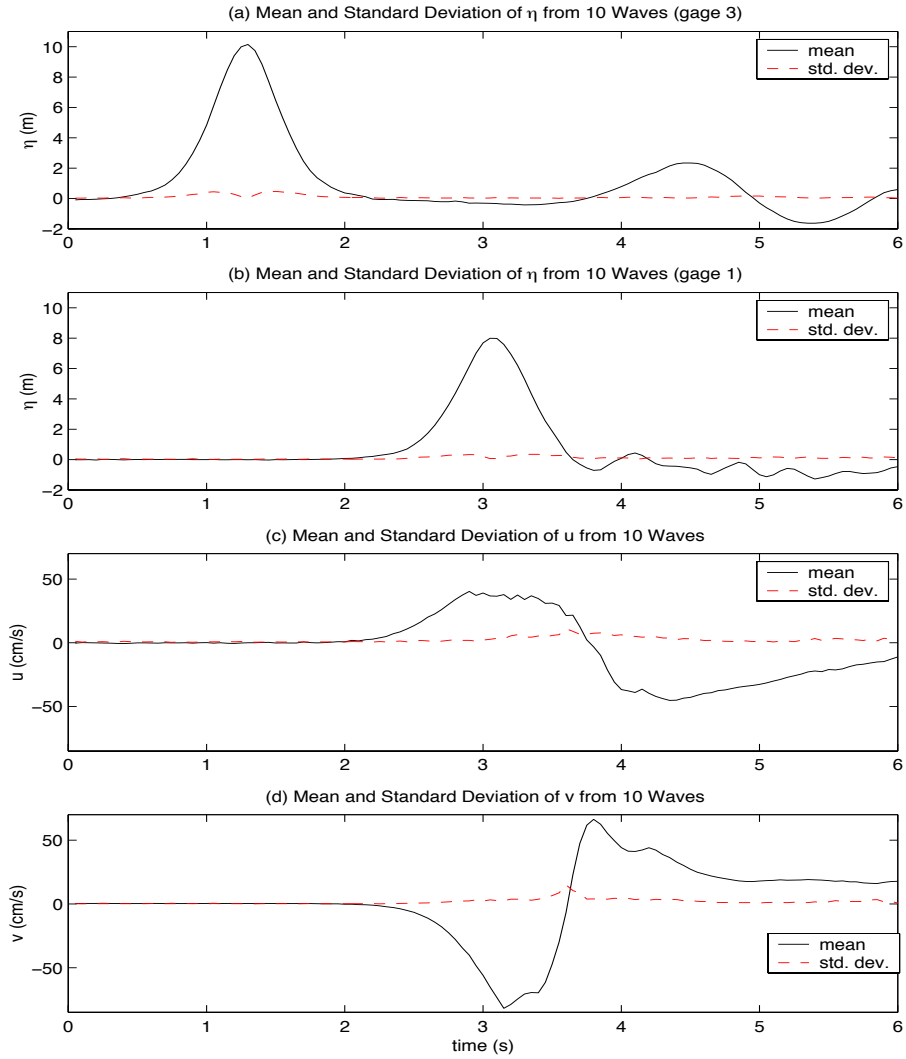


Figure 2.5: Repeatability tests for solitary waves with an average $H = 10.3\ cm$.

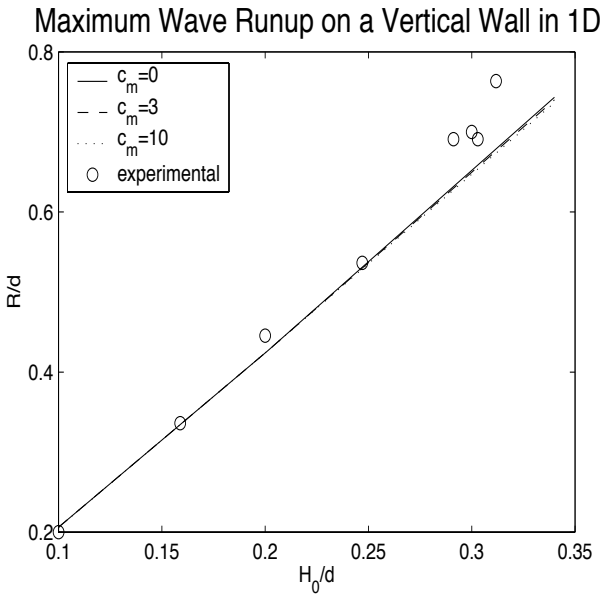


Figure 2.6: Wave runup vs. incident wave height. Nine numerical tests were carried out, three different wave heights ($H$ = 3, 6, and 10 $cm$) for each of three mixing coefficients ($c_m$ = 0, 3, and 10). Circles represent experimental data from Chan and Street (1970).

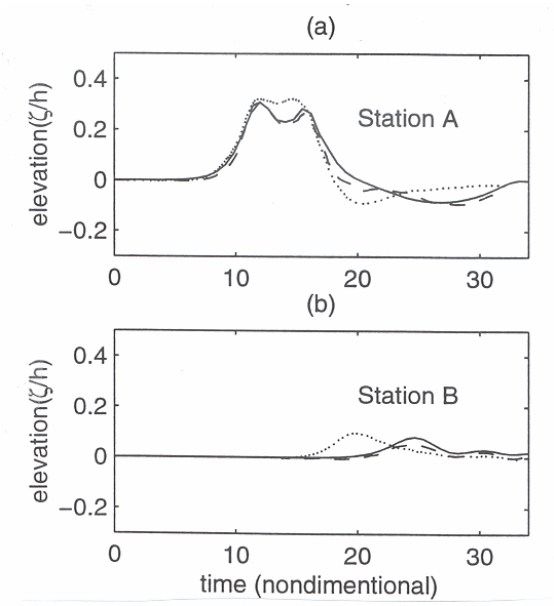


Figure 2.7: $\eta$ comparisons between stations A (a) and B (b). The solid line is data results obtained by F. Shi using the model by Shi et al. (2000), the dashed line is the experimental data (Liu, 1984), and the dotted line is linear theory (Liu, 1984).

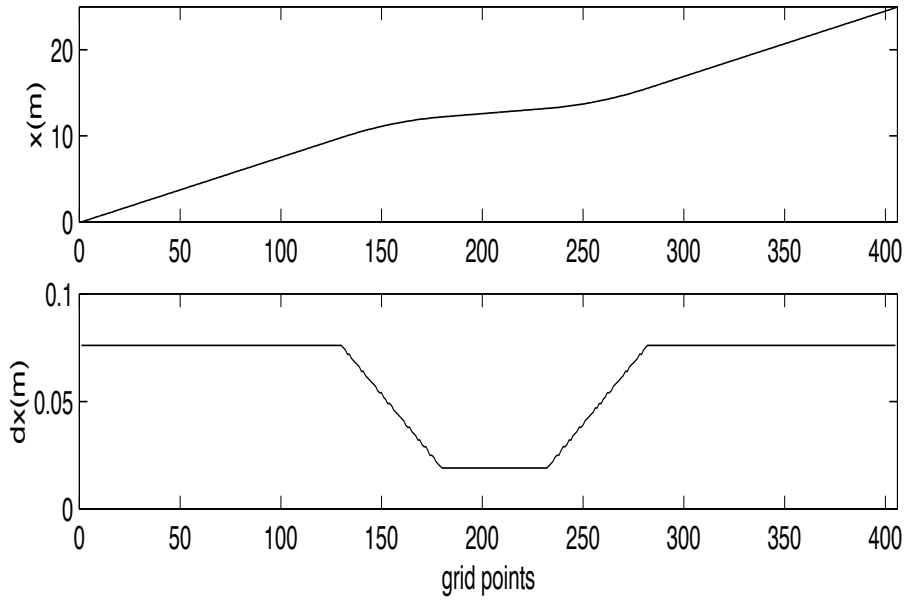


Figure 2.8: Plot of grid points and corresponding $x$ and $dx$ values for the tank.

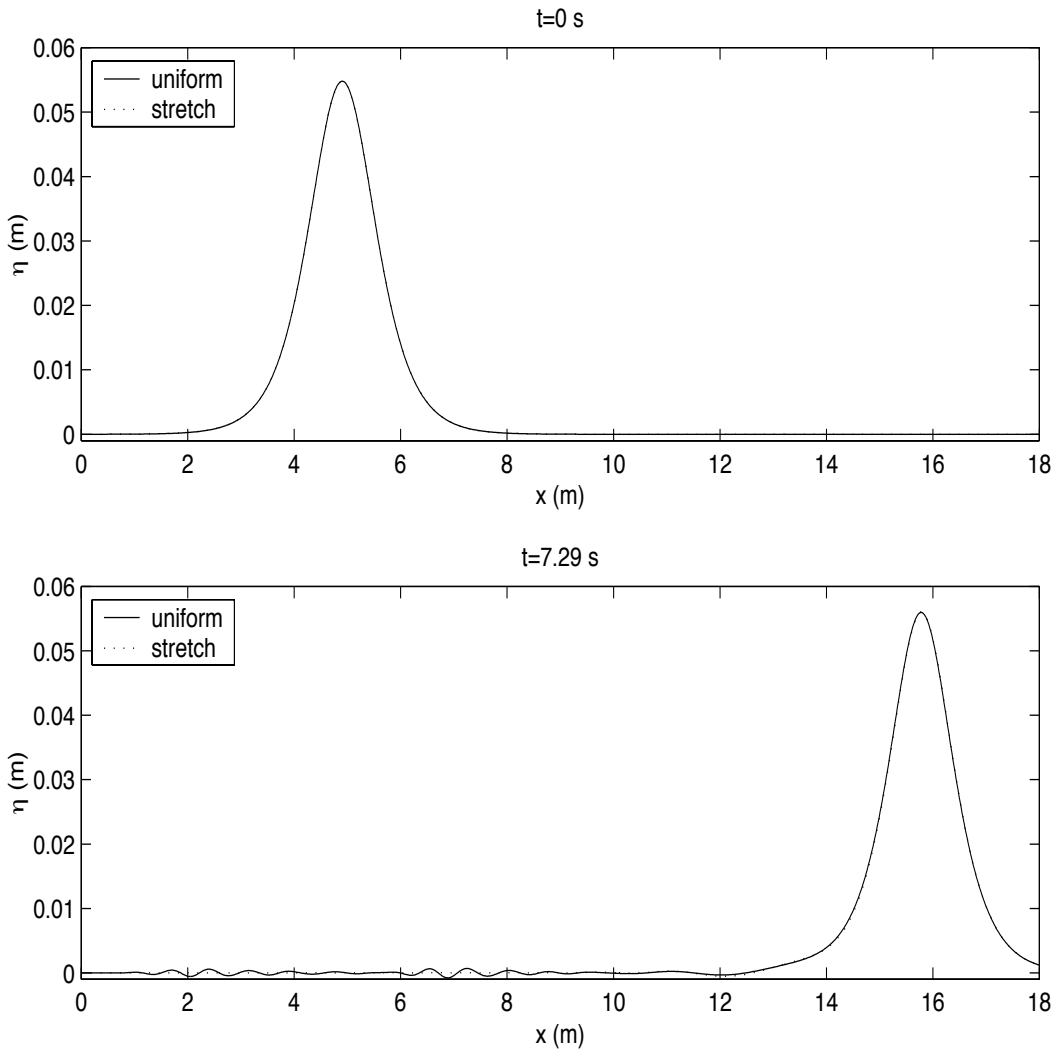


Figure 2.9: Numerical solution for both the uniform and variable grids. In (a) $t = 0$ and $t = 7.29\ s$ in (b).

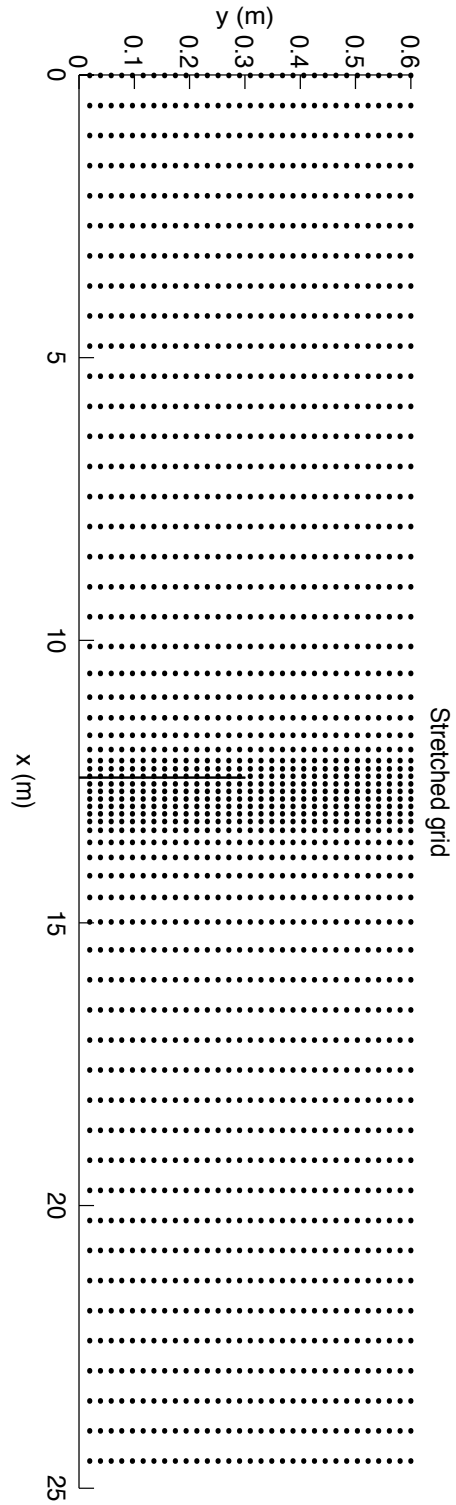


Figure 2.10: Stretched grid utilized by the model.

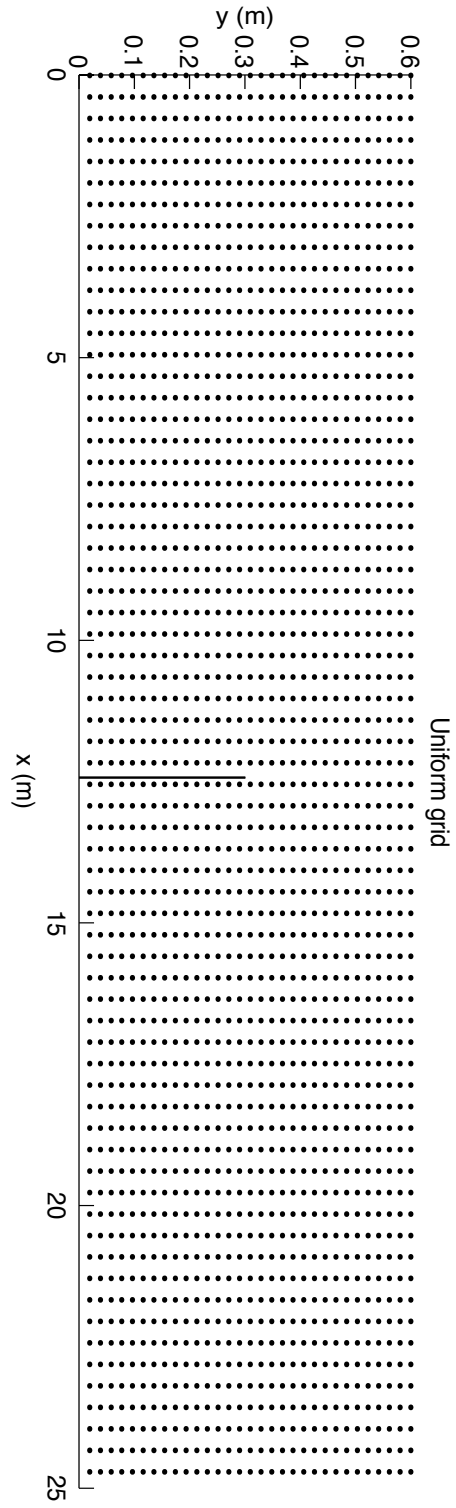


Figure 2.11: Uniform grid utilized by the model.

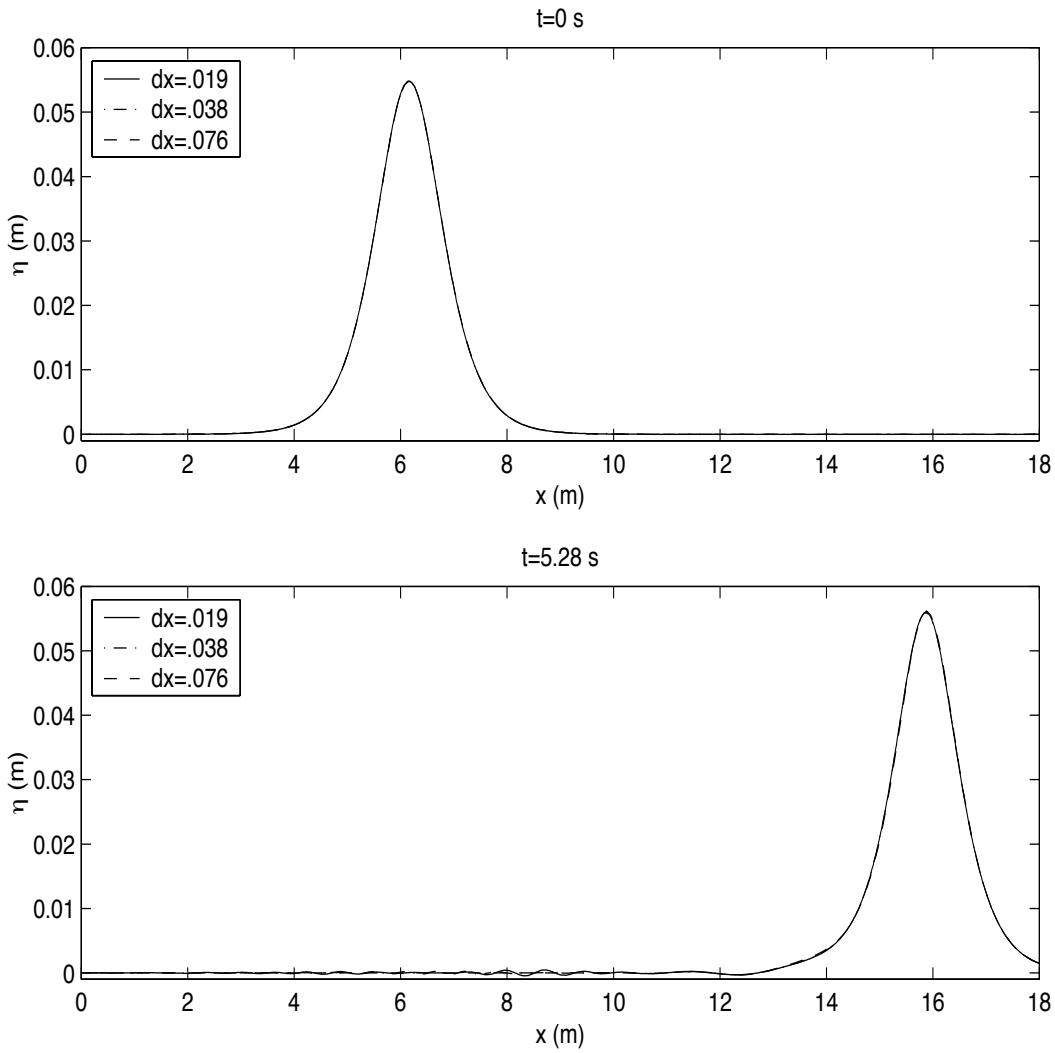


Figure 2.12: Convergence tests showing the surface elevation at $t = 0$ in (a) and $t = 5.28\ s$ in (b).

# Chapter 3

# RESULTS and COMPARISONS

The results from the modeling part of this study are presented first followed by results from the experiments that were conducted. Comparisons between data and model results are made in this chapter and will be discussed in the following chapter.

## 3.1 Surface Elevation Data

The time series of surface elevations from the numerical model were overlayed on top of the time series of experimental data for corresponding locations in the domain of the wave flume to show how the temporal changes in the surface elevation occur throughout a single model run as a solitary wave propagates past the breakwater structure.

### 3.1.1 Small Wave Height

The data is plotted in several ways to facilitate understanding of the fluid processes in this study. The data for $H = 5.48\ cm$ in Figure 3.1 shows a spatial arrangement representative of the $x$ and $y$ wave gage locations in the tank relative to one another for the small wave height case. The correlation between the model and the experiments is very good in general, but with some differences. For example, the surface elevation in the experimental and model data decreases by more than 1 $cm$ when the transmitted solitary wave reaches the gage at $x = 12.55\ m$, $y = 0.30\ m$ but by the time the transmitted solitary wave reaches gage 5 at $x = 13.83\ m$, $y = 0.40\ m$ the surface elevation returns to that predicted by the model data.

Figure 3.2 shows $\eta$ time series comparisons between model and experimental data at the six $x$ locations, from the moving carriage, highlighted in red in Figure 2.3 (c). There is a slight overprediction of the surface elevation at $x = 12.55\ m$, $y = .50\ m$ and at $x = 12.55\ m$, $y = .30\ m$. Moving away from the structure (in the positive $x$ direction) the model prediction improves. This can be seen more clearly in the data plotted in Appendix A for all three gages on the moving carriage, 1, 2, and 4. The entire array of $x$ locations for the data shown in Appendix A are plotted in Figure 2.3 (c). The time series data in Appendix A show that there is a significant decrease in the experimental data at gage 2 for $x = 12.64 - 12.80\ m$, $y = 0.30\ m$. This may be a physical phenomenon or it may be due to instrument error. More data needs to be collected before this may be determined. The model slightly underpredicts the wave height for $x = 12.57 - 12.63\ m$ and the predictions at gage 1 are very good and improve with increasing $x$ to capture details in the wave structure extremely well.

Figure 3.3 shows $\eta$ contours of four instances in time from the experimental data. The plot was formulated by taking the surface elevation data collected from all of the $x$ locations shown in Figure 2.3 (c) and forming contours of the surface elevation at four instances in time. The gap in the data, to the right of the structure, is due to an inability to move the instruments any nearer to the structure. The vortex location is indicated by a depression in the surface elevation and the contours at $t = 5.2\ s$ with values of $\eta = -1.5\ cm$ and $\eta = -1.0\ cm$ show the first sign of the vortex. At $t = 5.2\ s$ the vortex had begun to move downstream of the structure and is also moving in the increasing $y$ direction. The depression at the core of the vortex increases to greater than $-2.0\ cm$ indicated by the contour line of $\eta = -2.0\ cm$ at $t = 5.4\ s$. As the vortex begins to spread out the surface depression dissipates and this is illustrated by the contour plots at $t = 5.5\ s$ and $t = 7.25\ s$. Dissipation of the surface depression at the core of the vortex occurs over several seconds, however, the vortex itself was observed to persist for several minutes.

Contours of $\eta$ from the model data for the small wave height case are shown in Figures 3.4 and 3.5 for eight time steps. In these figures it is clear that there is a surface depression in $\eta$, representing the vortex core, and that this signature of the vortex is advected away from the structure. The magnitude of the surface depression increases to nearly $-1.0\ cm$ at $t = 3.4\ s$ and then by $t = 3.9\ s$ the vortex has begun to spread out and the surface signature dissipates. The model underpredicts the magnitude of the surface depression observed in the experimental data.

Velocity vectors were plotted over contours of surface elevation in Figures 3.6 and 3.7 for the same eight time steps to verify the temporal and spatial coincidence of the depression in the surface elevation, which is being called here the surface signature, with the vortex itself. The vortex location is represented in these figures by a closed loop of velocity vectors. These plots show that as the vortex forms the surface becomes depressed at the center of the vortex and this surface depression is advected away from the structure along with the vortex. Once the surface signature dissipates, the vortex persists beyond that time.

### 3.1.2 Large Wave Height

Similar results are observed for the large wave height case as for the small wave height case. Figure 3.8 shows the time series of surface elevation data comparing model and experimental data. The individual plots are arranged according to the way the instruments were set up in the tank. For the large wave height case there is increased resolution in the cross-tank ($y$) direction because there are two additional gages on the moving carriage (compare Figures 2.3 (c) and 2.4 (c)). Comparisons between the model and experimental data in general are not as good near the structure for gages 1, 7, 2, 8, and 4. However, comparisons improve dramatically further from the structure. This can be seen more clearly in Figure 3.9 representing several time series of $\eta$ for the $x$ locations marked in red in Figure 2.4 (c). There is a surface depression, indicative of the location of the vortex core (or proximity to the vortex core) at $x = 12.49\ m$, $y = 0.40\ m$. The signature of the vortex, manifested as a depression in $\eta$, is actually evident in several of the gage locations. Appendix B shows the time series data for the five gages on the moving carriage for all of the $x$ locations shown in Figure 2.4 (c). The prediction of $\eta$ improves by the time the transmitted solitary wave reaches a distance of only 14 $cm$ downstream of the breakwater. Here the model captures detail in the wave structure extremely well. The model simulation of the transmitted solitary wave is particularly good for gages 1, 7, and 2 for $x > 12.57\ m$. Gage 8 predicts $\eta$ well and gage 4 slightly overpredicts the experimental data for all $x$ locations.

Figures 3.10 and 3.11 shows $\eta$ contours for eight instances in time from the experimental data. These figures were generated in the same manner as was described for the small wave height case. The contours in Figure 3.10 at $t = 3.3\ s$ show the first stages of the vortex generation indicated by the contour line $\eta = -0.03\ m$. At

$t = 3.4 - 3.5$ $s$ the surface deformation increases in magnitude to a value greater than $\eta = -.05$ $m$. The vortex moves in the increasing $y$ direction. In Figure 3.10 at $t = 4$ $s$ and in Figure 3.11 at $t = 4.1 - 4.3$ $s$ the vortex moves downstream and then in the direction of increasing $y$. At $t = 4.4 - 5.2$ $s$ the depression of the water surface begins to dissipate though the vortex itself was observed to persist for several minutes.

Contours of the surface elevations from the model are shown in Figures 3.12 and 3.13 for eight time steps. The depression in $\eta$ forms over the time interval $t = 1.5 - 1.8$ $s$ and during this time the depression in $\eta$ seems to move slightly upstream. Subsequently, the surface signature is advected downstream and this is illustrated by the contours at $t = 2.2 - 2.3$ $s$. It is not clear why the surface depression initally moves upstream in the model but it is thought to be erroneous and this is something that needs to be investigated further.

Figures 3.14 and 3.15 show contours of $\eta$ overlayed with velocity vectors. For the large wave height case the vortex is first formed at approximately $t = 1.8$ $s$ as evidenced by the closed loop of velocity vectors. The advection of the surface depression downstream of the structure at $t = 2.2 - 2.3$ $s$ is coincident with the movement of the vortex. The magnitude of the surface depression is nearly $\eta = -0.01$ $m$. This, again, underpredicts the magnitude of the experimental data which shows that a maximum is reached of $\eta > -.05$ $m$.

## 3.2 Vorticity Data

The vorticity, generated by taking the curl of the momentum equations as described earlier, can be a convenient way to view the velocity field and evolution of the flow field over time. In both the experimental and numerical parts of the study, a vortex was generated and the strength of this vortex may be visualized through consideration of the vorticity field. In order to view the vorticity of the experimental data it would be necessary to obtain a high resolution data set. In the present study this was not possible. However, it is possible to view the vorticity of the numerical data and this is presented below for both the small wave height and large wave height cases.

### 3.2.1 Small Wave Height

In Figures 3.16 and 3.17 the vorticity field generated from the instantaneous velocity fields is plotted with the instantaneous velocity vectors superimposed. Eight different time steps illustrate how the vortex forms and is shed from the structure and is subsequently advected downstream. The vortex core initially forms at $y < 0.3\ m$ and $x < 12.5\ m$ and, subsequently, as the vortex is shed from the structure it moves towards both larger $x$ and $y$ values. This pattern of movement of the vortex corresponds to what occurs in the experiments as well. The strength of the vortex is greatest during the initial formation and decreases as the vortex separates from the structure and propagates downstream. This makes sense since the only forces acting after the solitary wave propagates past the breakwater are viscous forces. For the time steps shown the maximum horizontal velocity is $u = 0.70\ m/s$.

### 3.2.2 Large Wave Height

The vorticity field for the large wave height case is similar to the small wave height case. Figures 3.18 and 3.19 show the vorticity field overlayed with the velocity vectors for eight times steps as shown. For the time steps shown the maximum horizontal velocity is $u = 1.08\ m/s$ and the maximum vorticity occurs during vortex generation. The vortex follows a similar pattern of movement as the experimental data. Vortex generation initially occurs at $y < 0.2\ m$ and $x < 12.65\ m$ and, subsequently, as the vortex is shed from the structure it moves towards both larger $x$ and $y$ values.

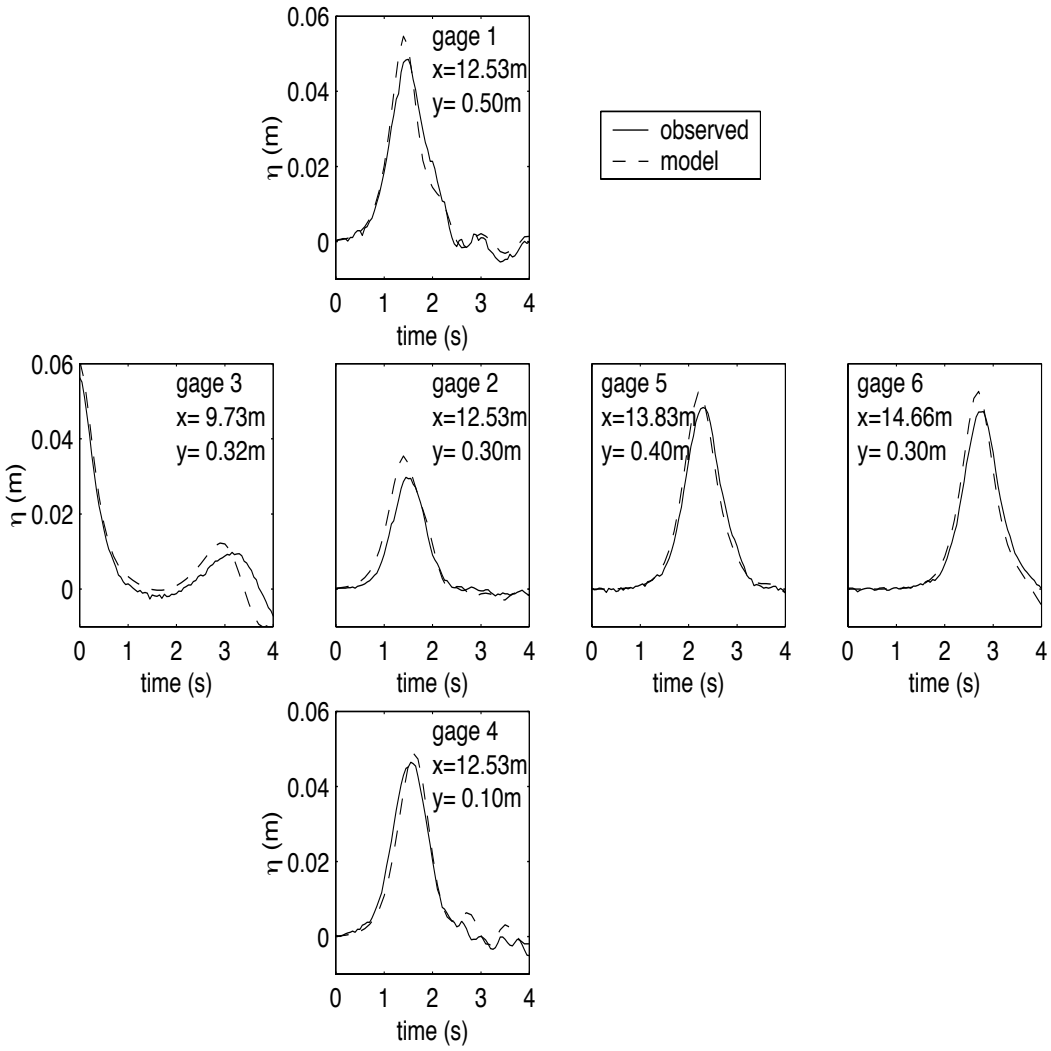


Figure 3.1: Comparison of surface elevations for $H = 5.48\ cm$ in an arrangement which represents the arrangement of the gages in the tank.

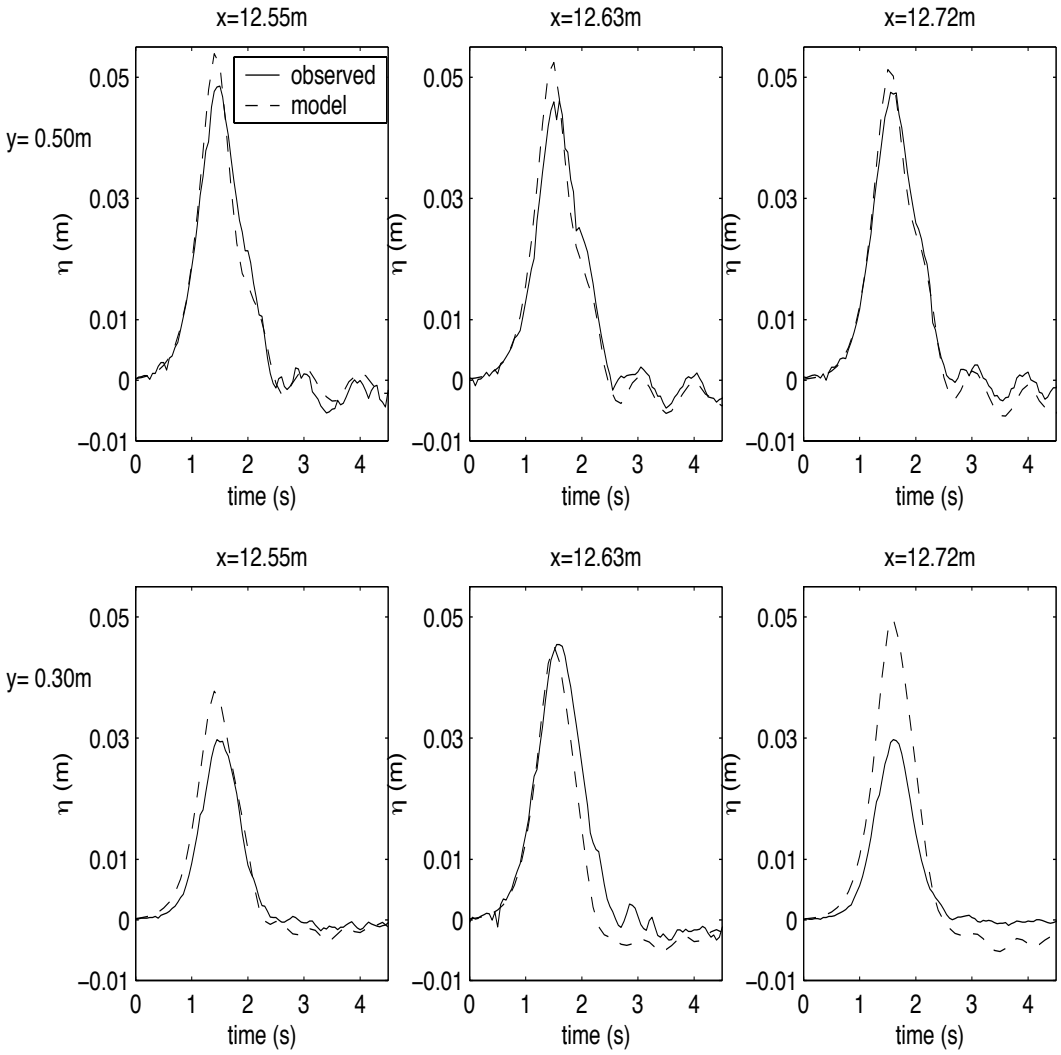


Figure 3.2: Time series of surface elevations for $H = 5.48\ cm$ at 6 $x$ and $y$ locations.

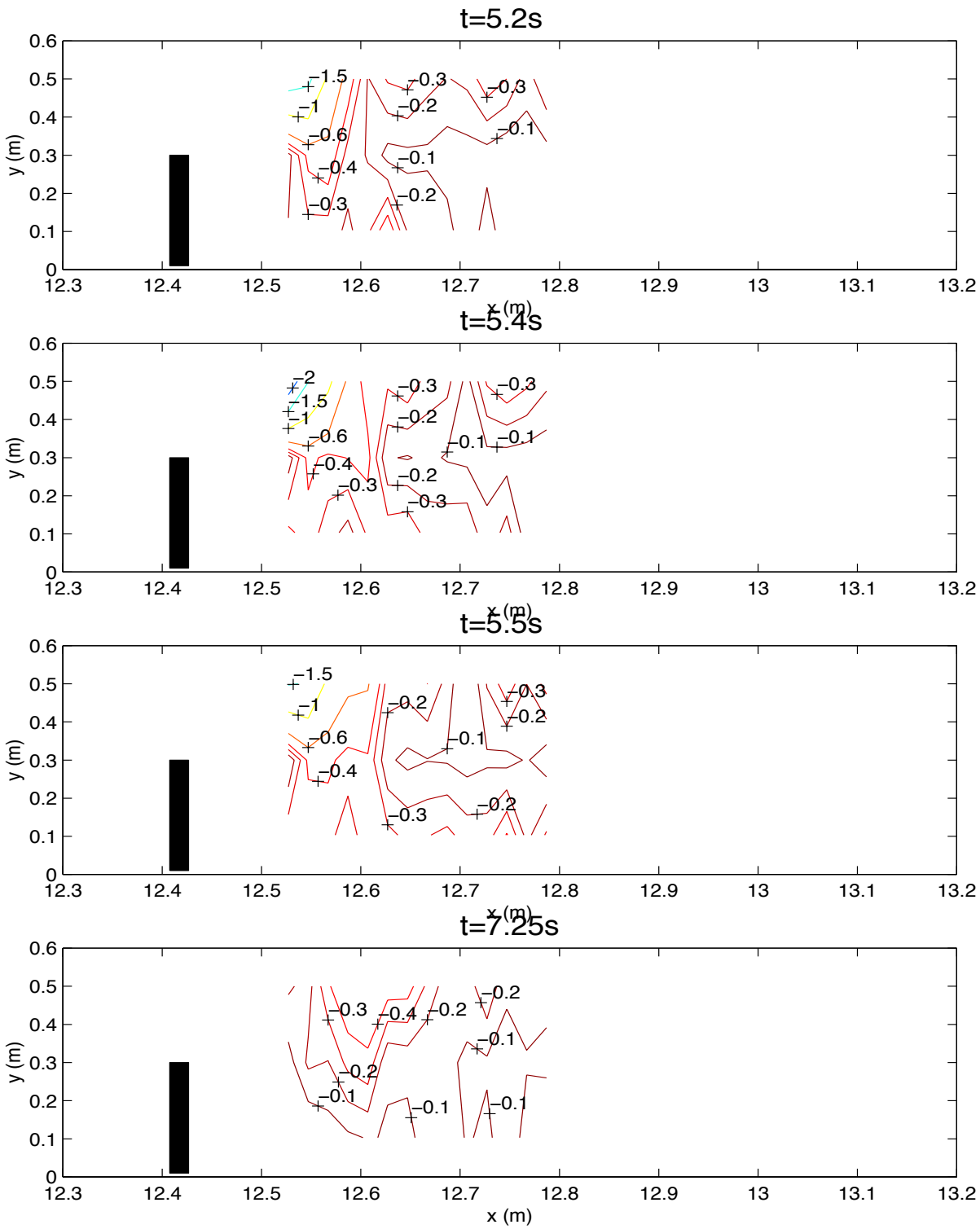


Figure 3.3: Contours of surface elevations (cm) from the experimental data for $H = 5.48\ cm$ at four instances in time.

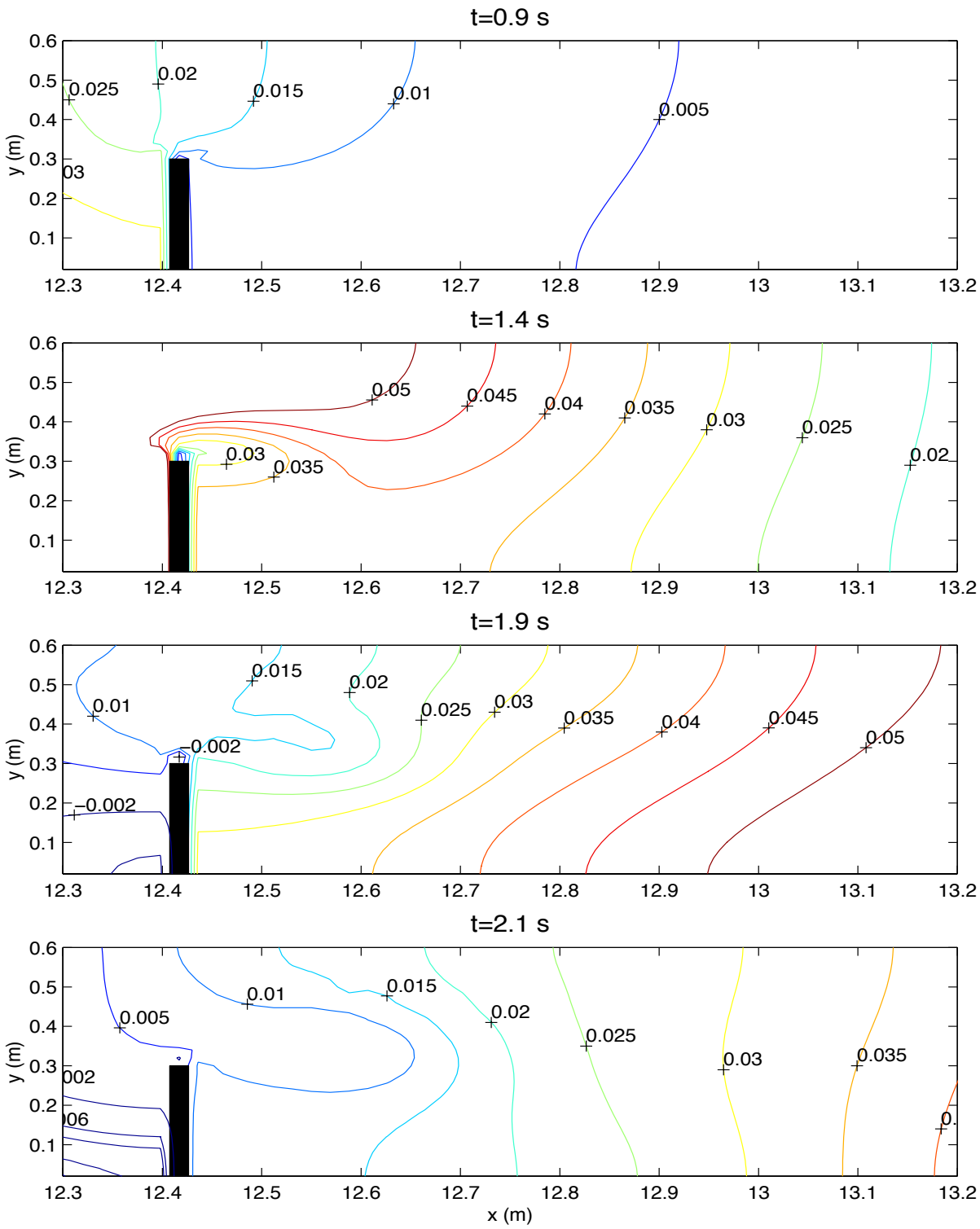


Figure 3.4: Contours of surface elevation (m) from the model data for $H = 5.48\ cm$ at four instances in time.

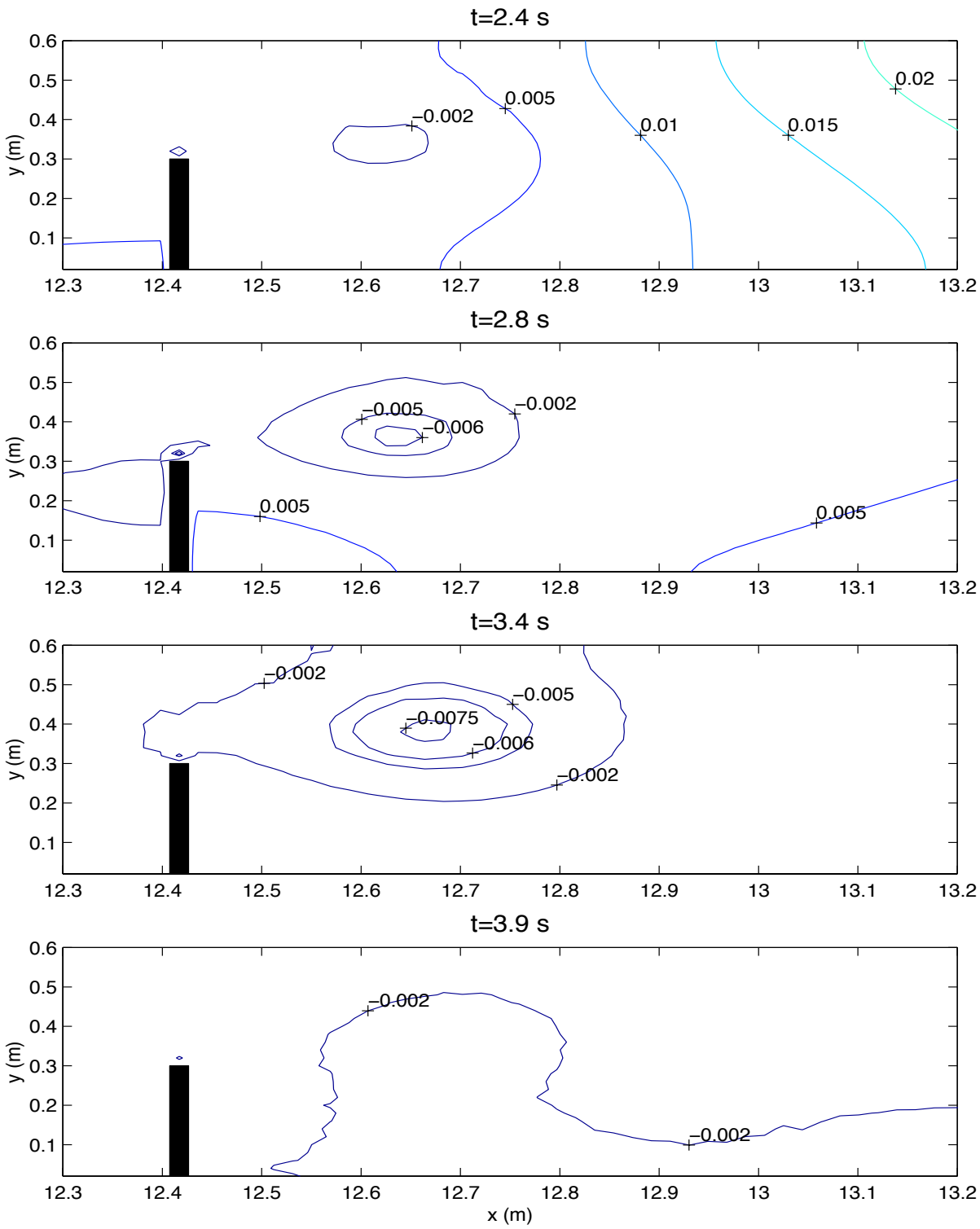


Figure 3.5: Contours of surface elevation (m) from the model data for $H = 5.48\ cm$ at four instances in time.

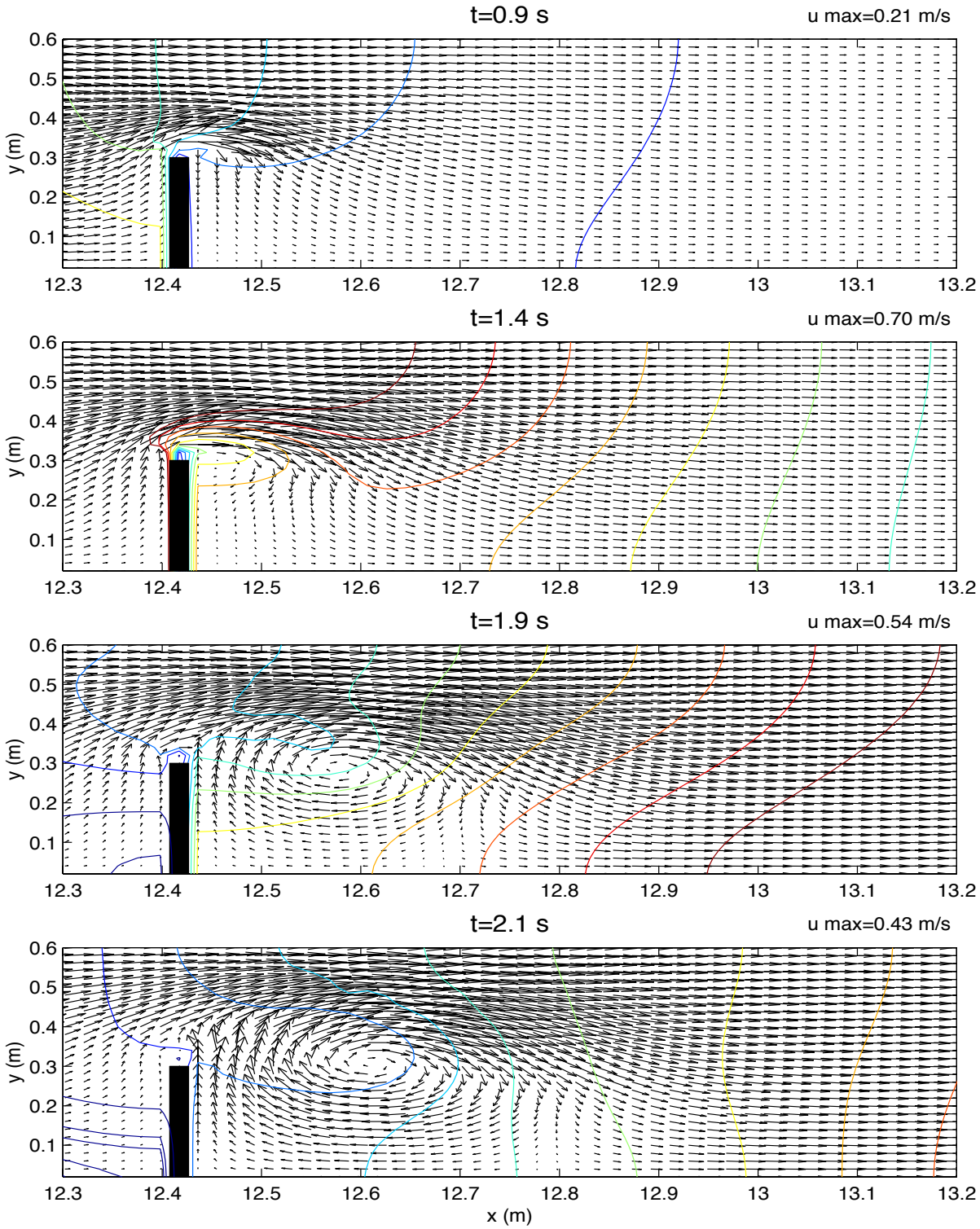


Figure 3.6: Velocity vectors overlayed on contours of surface elevations for $t = 3.5 - 5.0\ s$.

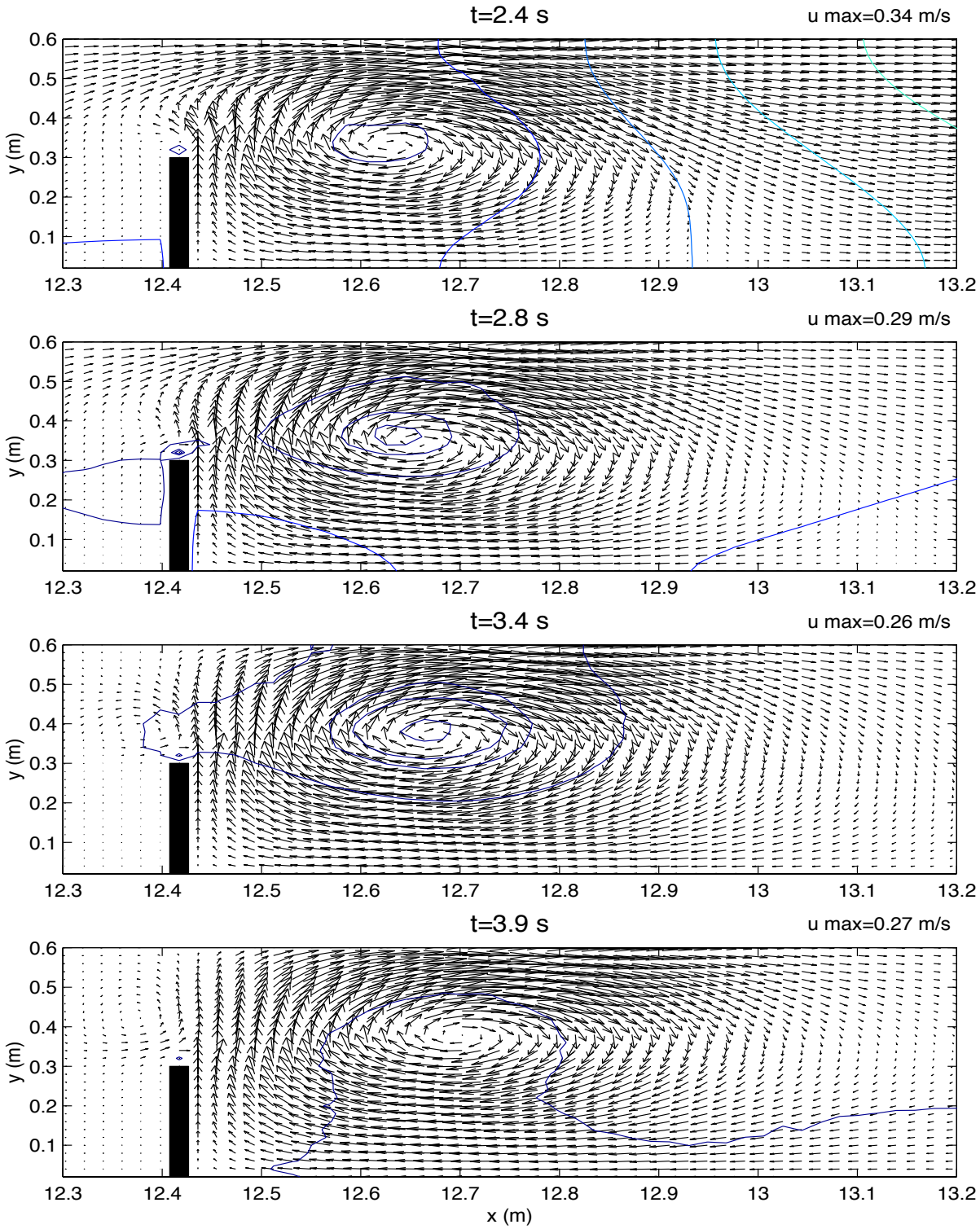


Figure 3.7: Velocity vectors overlayed on contours of surface elevations for $t = 5.4 - 6.5\ s$.

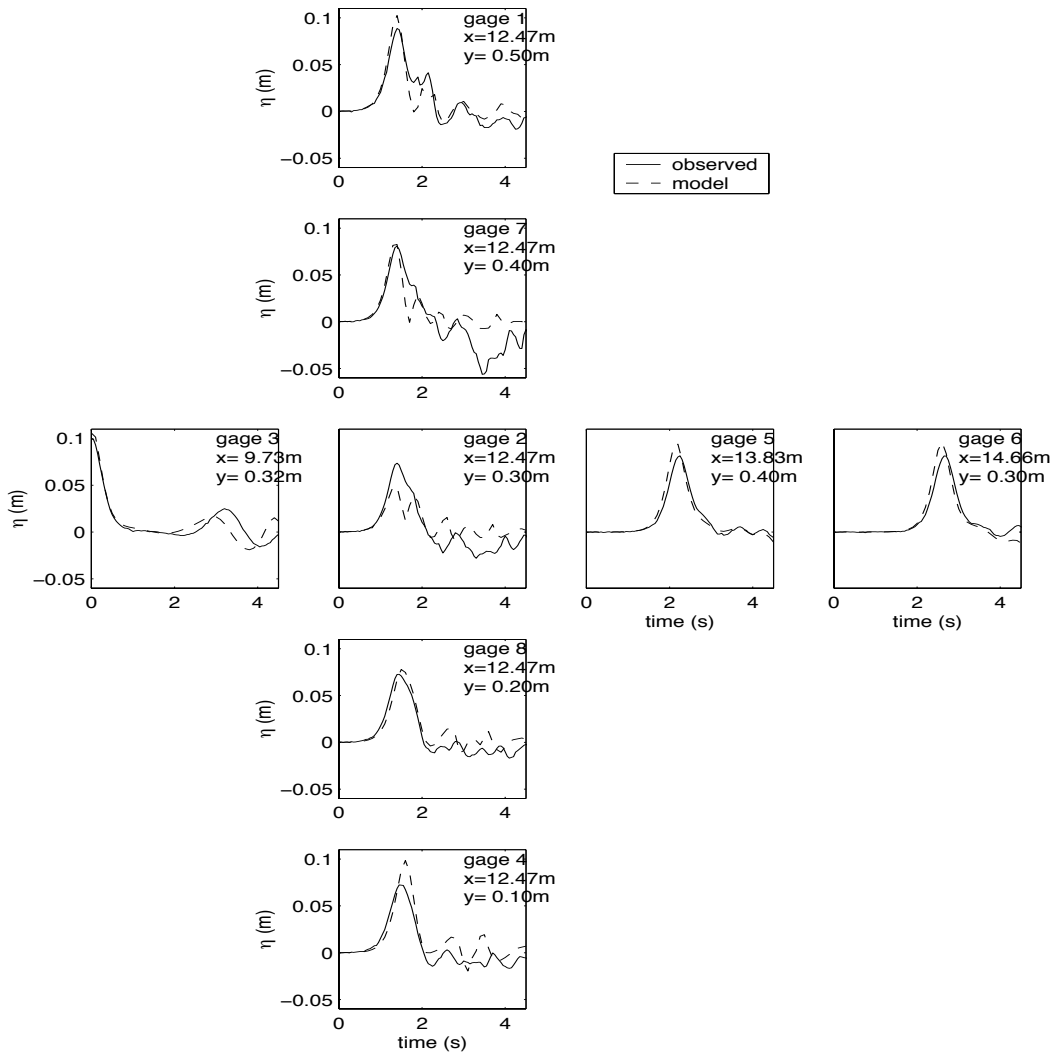


Figure 3.8: Comparison of surface elevations for $H = 10.3\ cm$ in an arrangement which represents the arrangement of the gages in the tank.

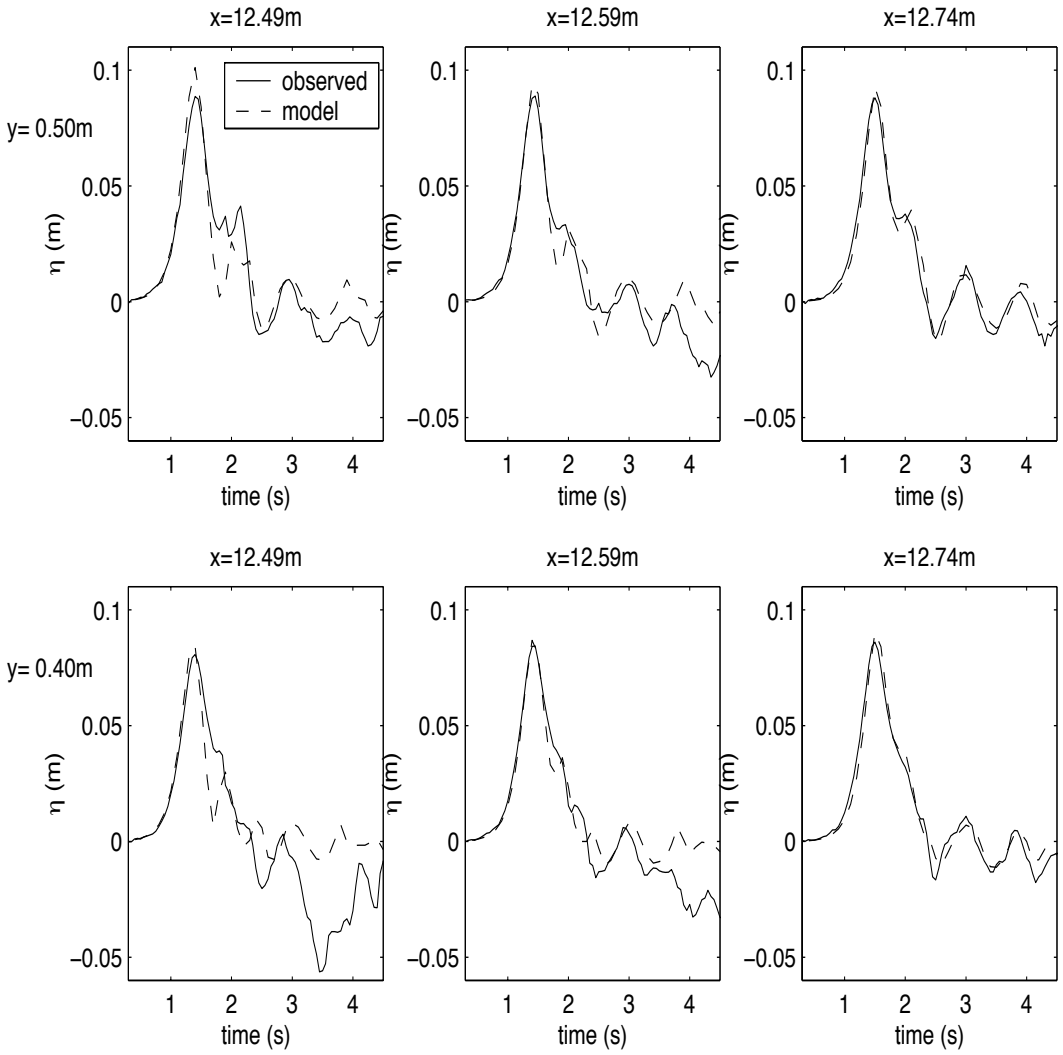


Figure 3.9: Time series of surface elevations for $H = 10.3\ cm$ at 6 $x$ and $y$ locations.

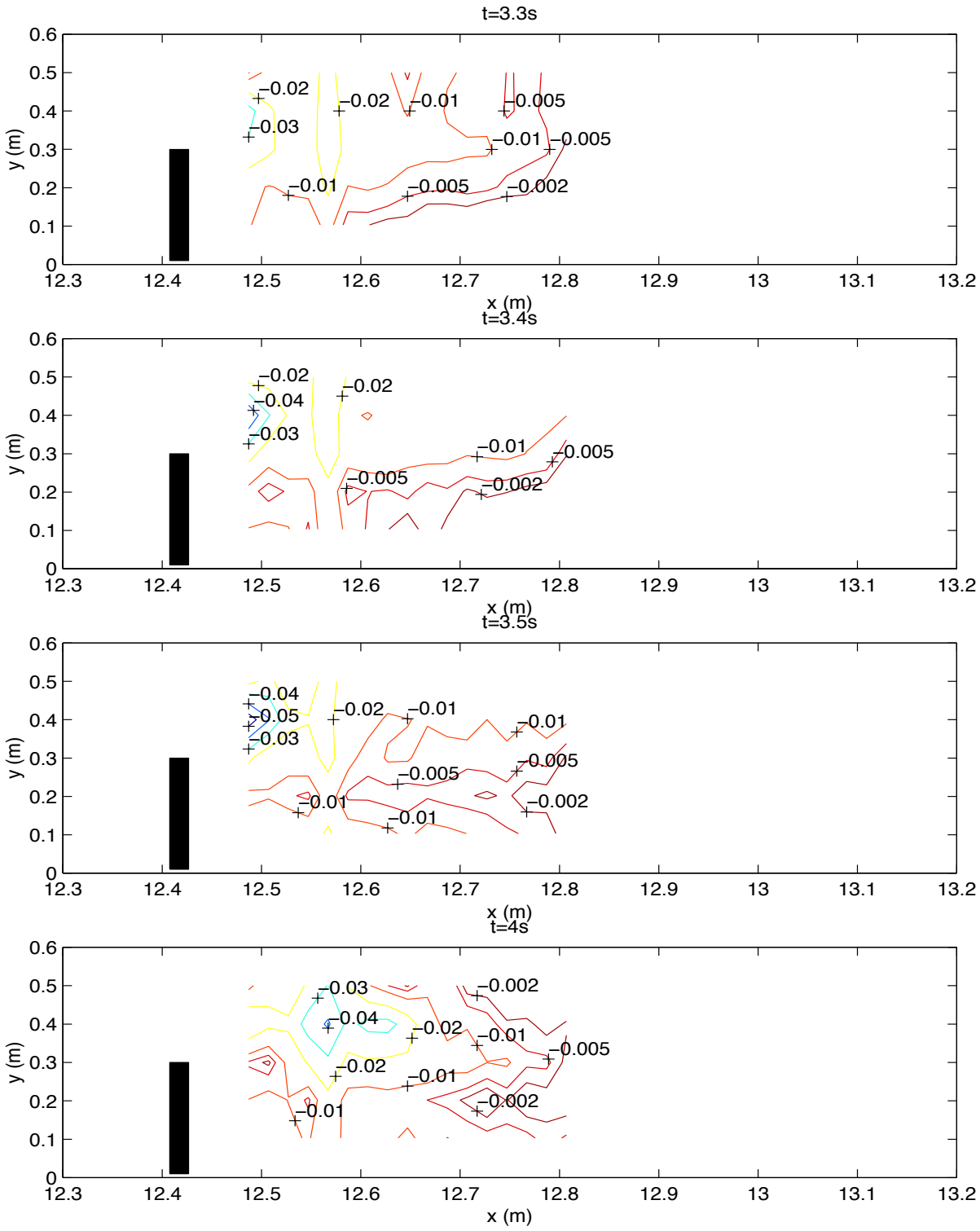


Figure 3.10: Contours of surface elevation (m) from the experimental data for $H = 10.3\ cm$ at $t = 1.5 - 1.8\ s$.

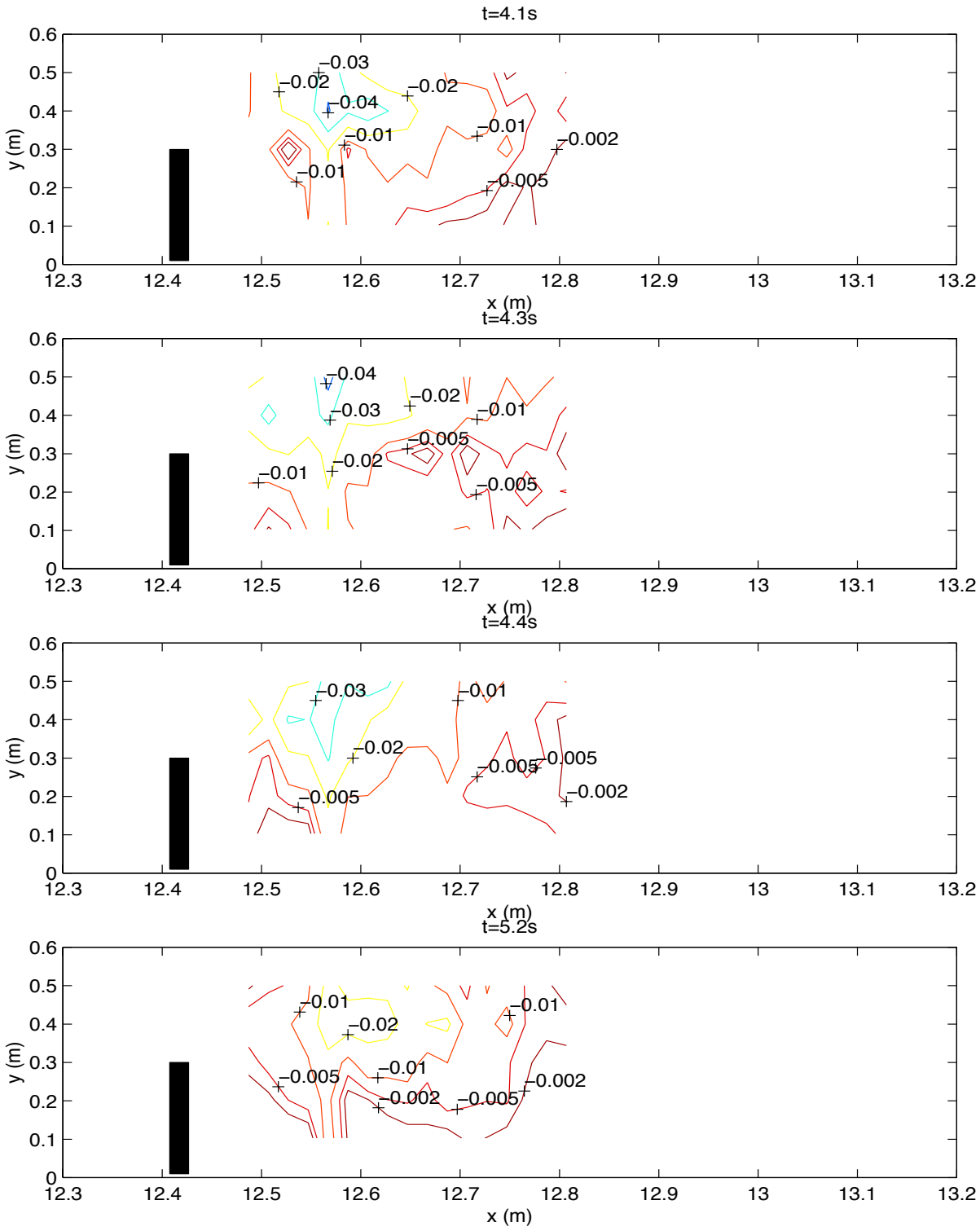


Figure 3.11: Contours of surface elevation (m) from the experimental data for $H = 10.3\ cm$ at $t = 2.0 - 3.1\ s$.

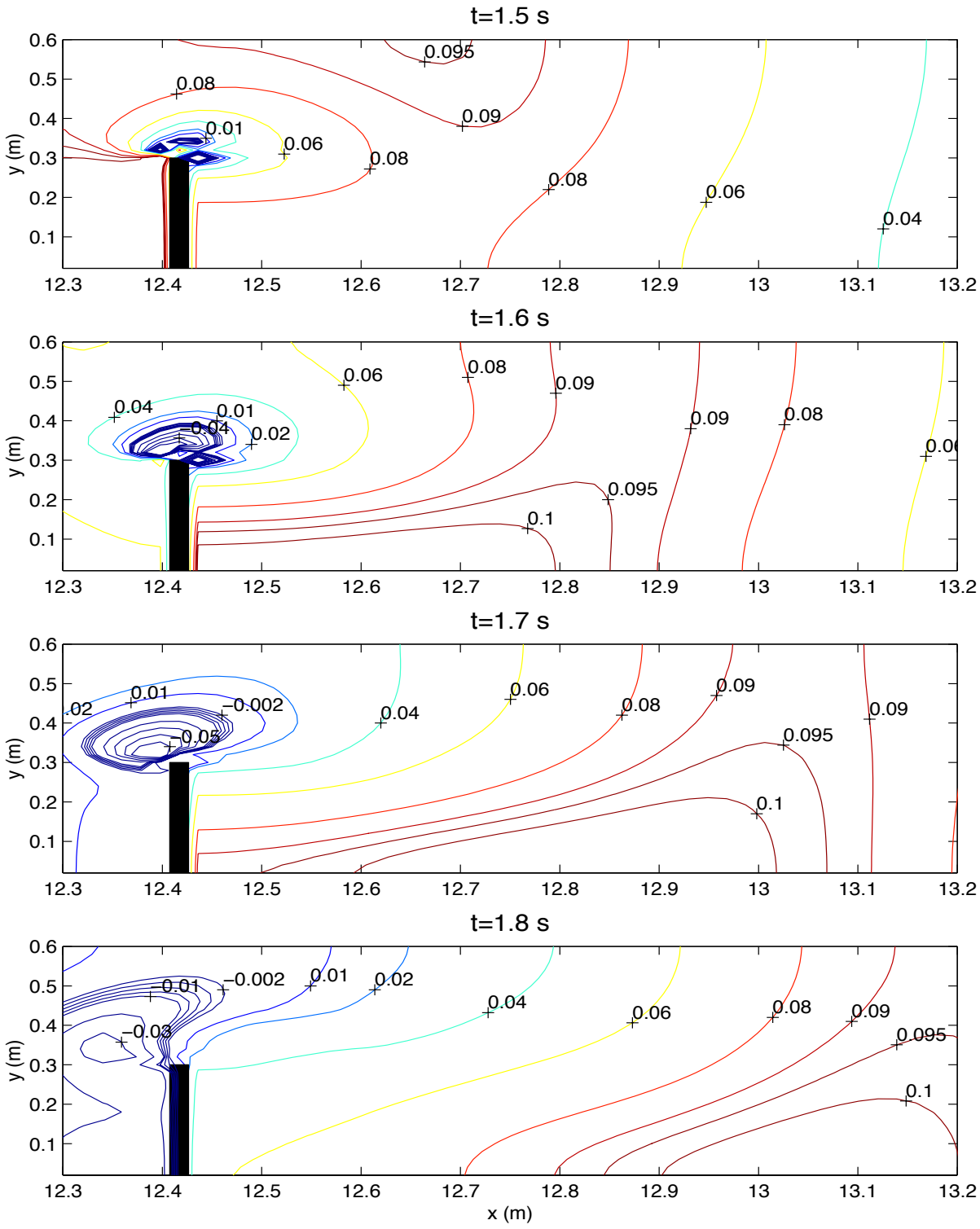


Figure 3.12: Contours of surface elevation (m) from the model for $H = 10.3\ cm$ at $t = 1.5 - 1.8\ s$.

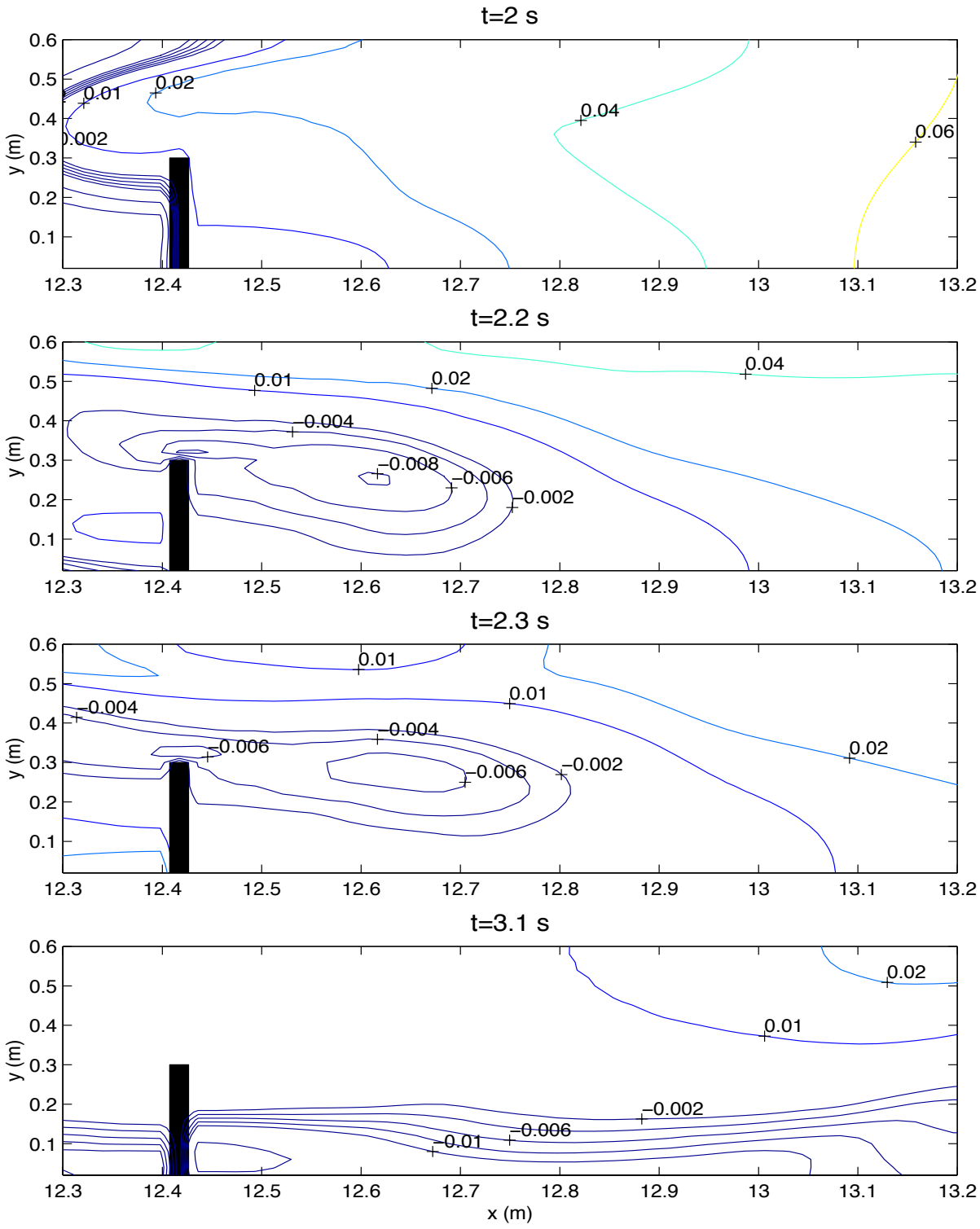


Figure 3.13: Contours of surface elevation (m) from the model for $H = 10.3\ cm$ at $t = 2.0 - 3.1\ s$.

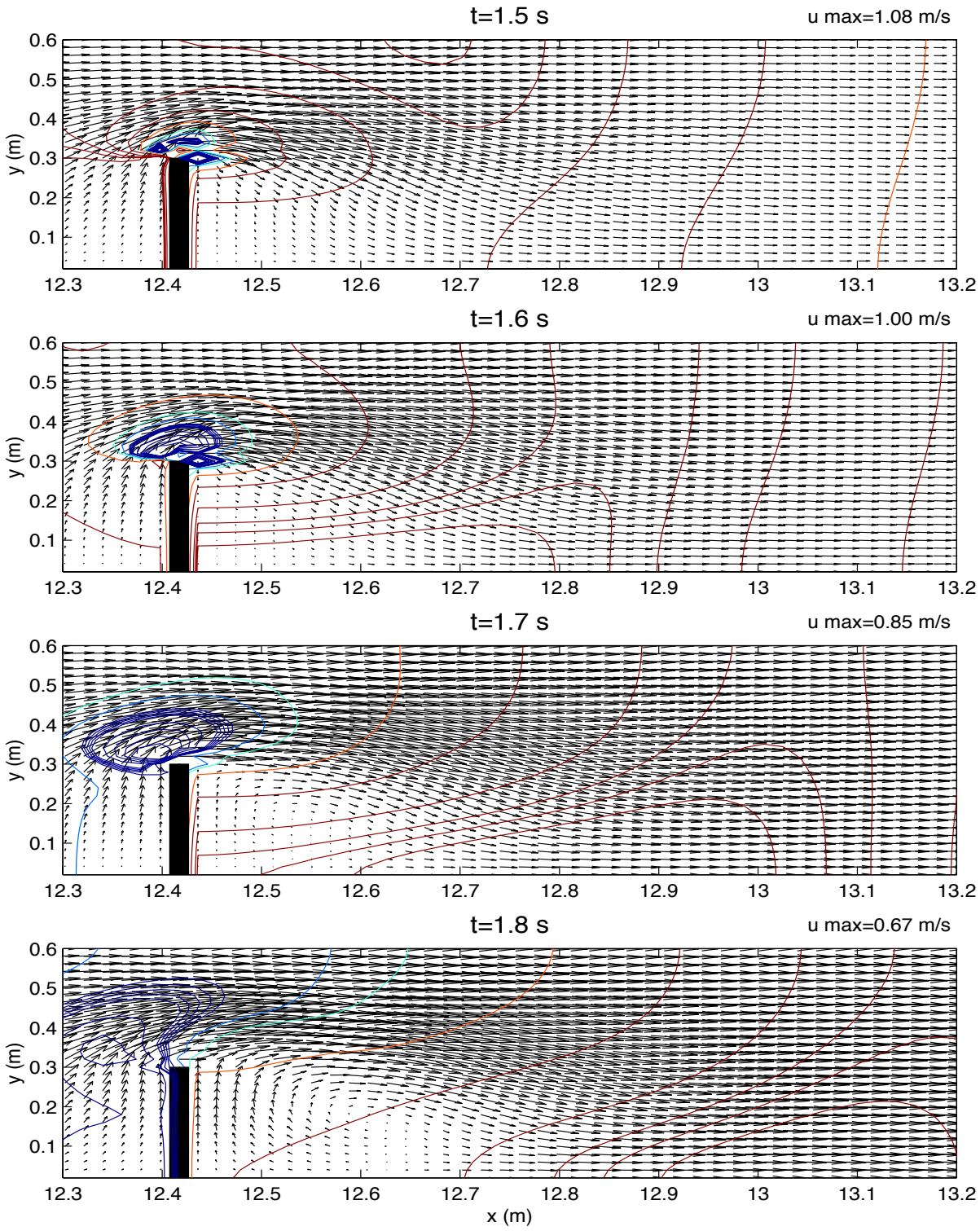


Figure 3.14: Contours of surface elevation (m) with velocity vectors from the model for $H = 10.3\ cm$ at $t = 1.5 - 1.8\ s$.

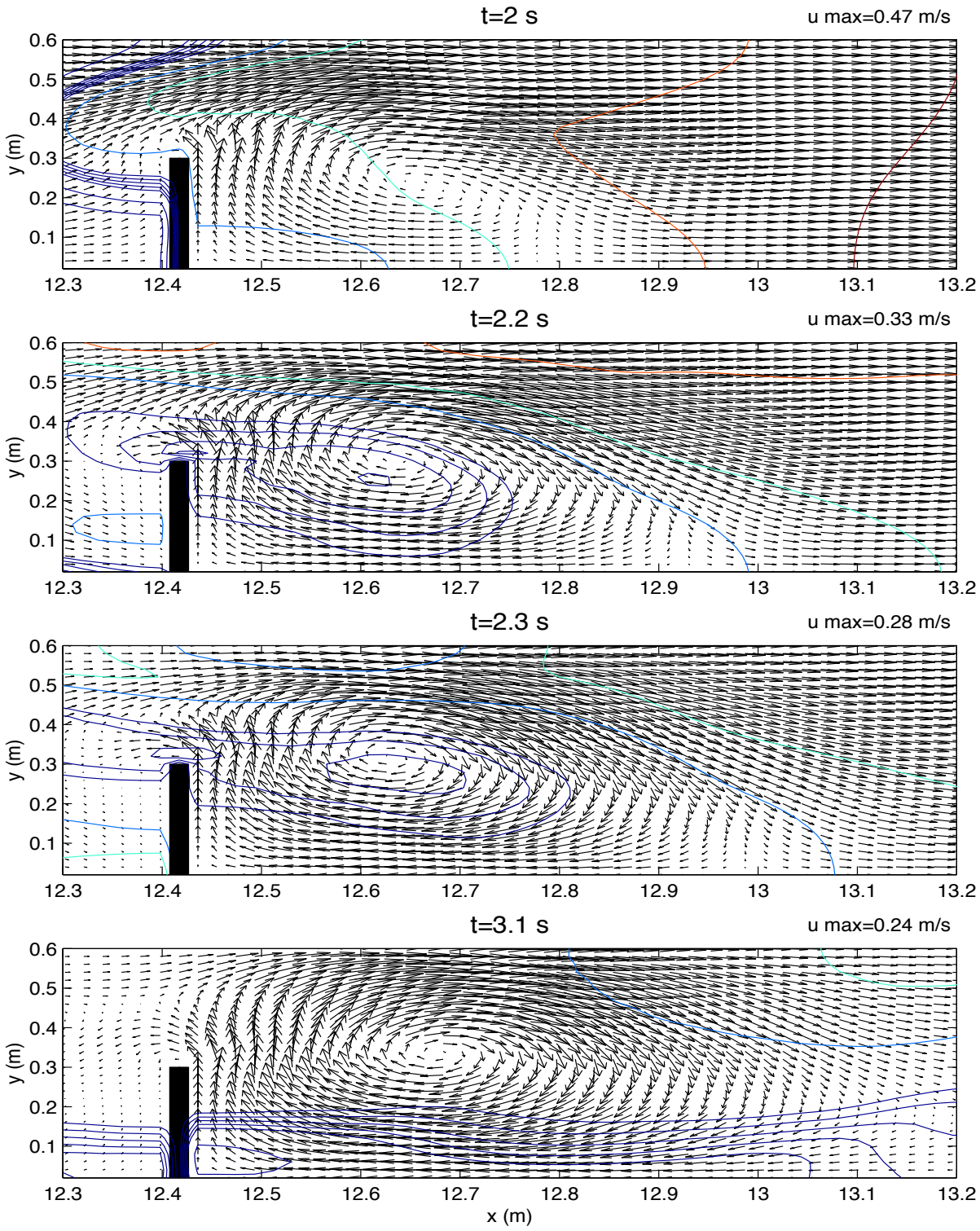


Figure 3.15: Contours of surface elevation (m) with velocity vectors from the model for $H = 10.3\ cm$ at $t = 2.0 - 3.1\ s$.

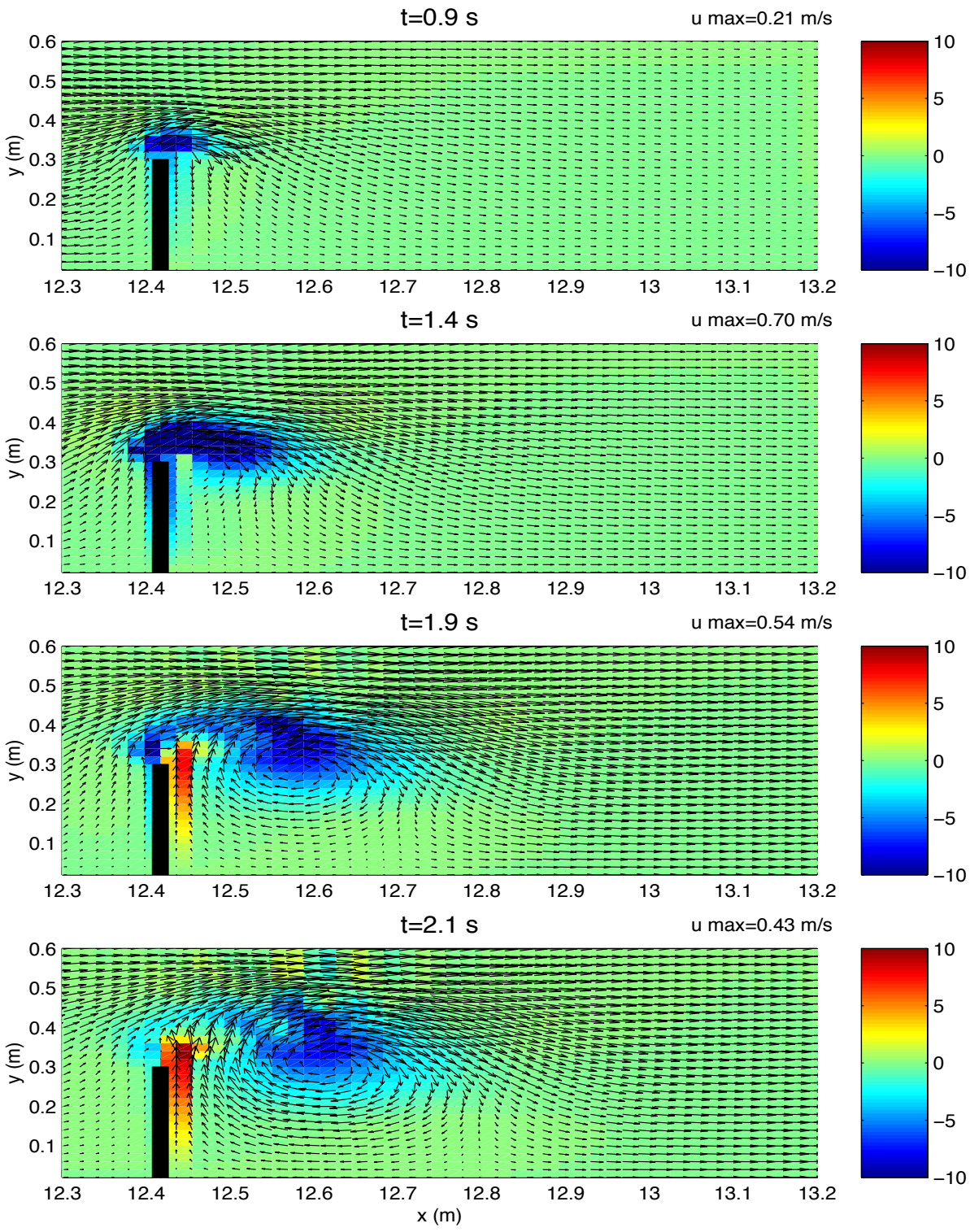


Figure 3.16: Velocity vectors overlayed on the vorticity field for $H = 5.48\ cm$. Colorbars give the vorticity in units of $s^{-1}$.

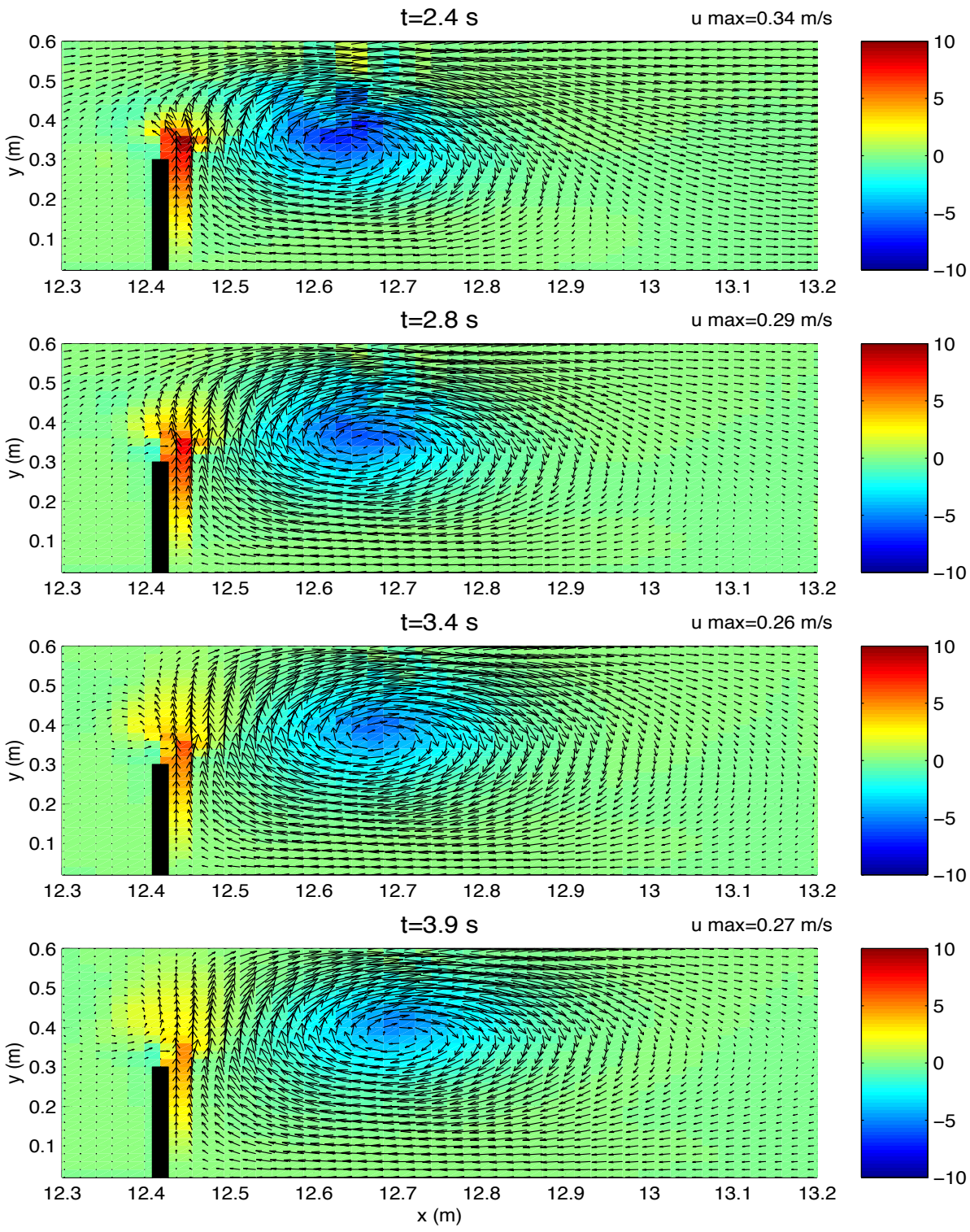


Figure 3.17: Velocity vectors overlayed on the vorticity field for $H = 5.48\ cm$. Colorbars give the vorticity in units of $s^{-1}$.

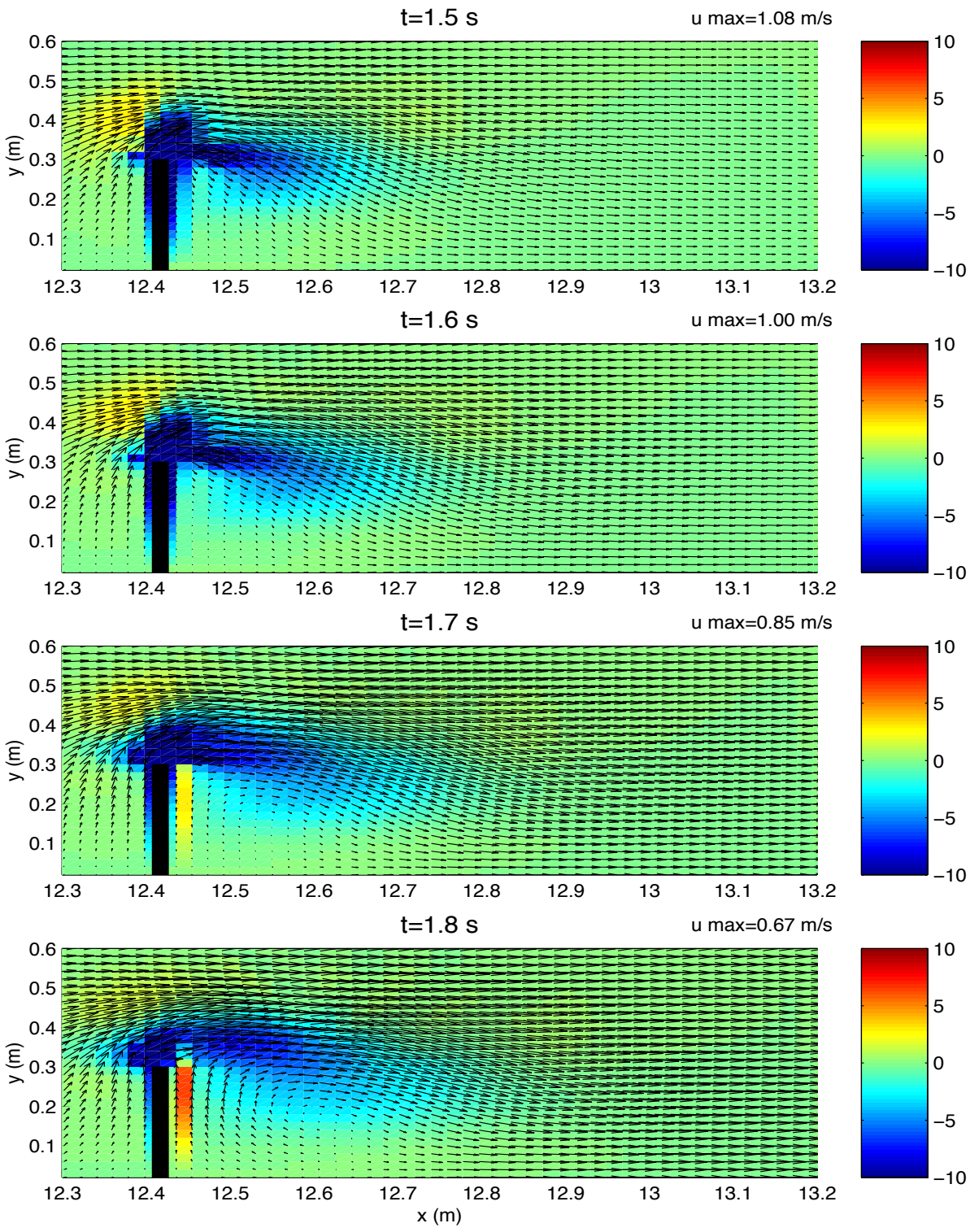


Figure 3.18: Velocity vectors overlayed on the vorticity field for $H = 10.3\ cm$. Colorbars give the vorticity in units of $s^{-1}$.

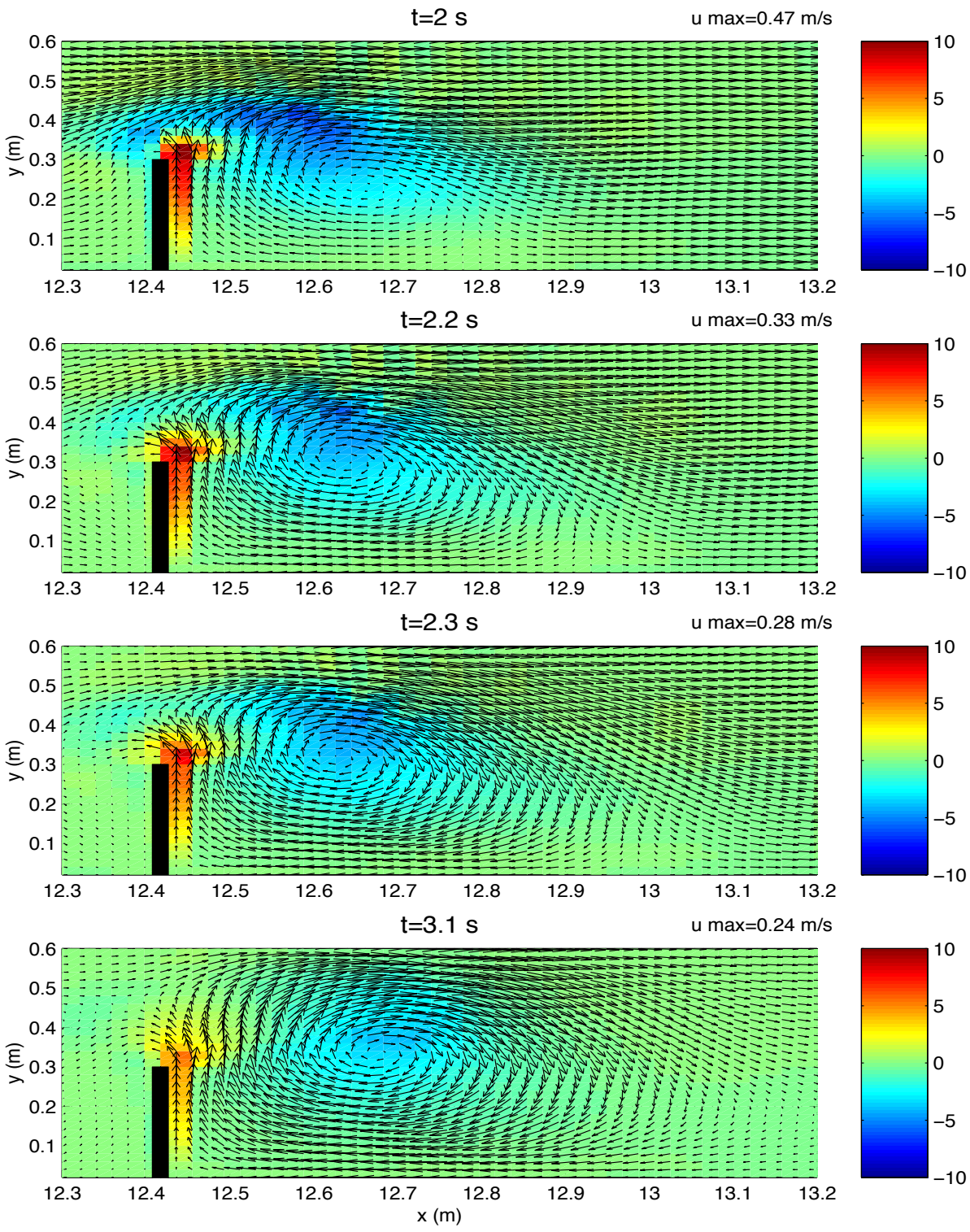


Figure 3.19: Velocity vectors overlayed on the vorticity field for $H = 10.3\ cm$. Colorbars give the vorticity in units of $s^{-1}$.

# Chapter 4

# DISCUSSION

The surface elevations from both the model and experimental data are discussed and comparisons are made to previous studies. The total circulation of the fluid is calculated and it's relevance to this study is discussed as well. Additionally, there is a section on vortex formation and a discussion of vortex characteristics.

## 4.1 Surface Elevation Data

The predictions of surface elevations by the model vary somewhat for both cases. Generally, comparison's of $\eta$ between the model and experimental data are fairly good near the breakwater and model predictions are very good further downstream of the breakwater structure. Details in the wave structure are captured extremely well by the model at some of these locations (see Appendix B).

Wang (1993) compared surface elevations from his numerical model to data collected from Liu's (1984) experiments. His results agreed fairly well with the experiments except it is noted that the wave heights from the experimental data are smaller due to dissipation effects not accounted for in the model. It was also observed that the amplitude of the transmitted solitary wave varies along the crest of these waves. An across tank oscillation has also been reported to occur in the experiments by Perroud (1957). In the present study there is substantial variation along the crest of the transmitted wave and this is illustrated in Figure 4.1 comparing $\eta$ between the model and the experiments at $x = 12.53\ m$ for $H = 5.48\ cm$. The figure shows both the model results (solid line) representing the surface elevation in the across tank ($y$) direction

with the experimental data (circles). The magnitude of the cross tank oscillation is illustrated as the solitary wave propagates past the structure. As the solitary wave begins to propagate past the structure the water surface rises more rapidly for $y > 0.3\ m$ (Figure 4.1, $t = 0.5 - 1.4\ s$). Diffraction of the wave then causes the $\eta$ surface to rise higher for $y < 0.3\ m$ (Figure 4.1, $t = 1.5 - 1.7\ s$) indicating a piling up of water downstream of the structure in the 'shadow zone'. Finally, after the solitary wave has propagated downstream and the vortex has also moved downstream of the structure, the surface elevation returns to a level surface. The surface deformation occurs more rapidly in the experimental data but the surface returns to a level surface over the same approximate time interval in both the model and the experimental data. In the experimental data there is some change in the surface elevation from $y > 0.3\ m$ to $y < 0.3\ m$ but it is not as large in magnitude as is evident in the model data. The depression near $y = 0.30$ visible at $t = 1.3 - 1.7$ is thought to be due to vortex generation. The surface deformation has the greatest magnitude where the vortex is generated, near the breakwater, and this is illustrated in the following section.

## 4.2 Characteristics of Vortex Formation

Figure 4.2 shows a schematic of a theoretical stationary vortex to illustrate simplistically how the velocity magnitude varies across the vortex in the present study. The velocity increases from the outer edge to a maximum velocity (moving across the vortex towards the center) and then reduces in magnitude again to a viscous core at the center of the vortex. Theoretically, there is a stagnation point at the core of the vortex and this is observed in both the experimental and numerical results as well.

Initially, when the vortex is first generated, the vortex has a small diameter and over time it was observed that the vortex spreads out resulting in a larger area of fluid rotation. This can be observed best in the model data. In Figures 3.6 and 3.7 for the small wave height case at time steps $t = 4\ s$, the velocities are the largest and only a small area of fluid is rotational. At $t = 4.5 - 6.5\ s$ the area of fluid rotation has increased but the magnitude of velocities has decreased. Figures 3.14 and 3.15 showing the model data for the large wave height case show a similar pattern.

As stated in the introduction, the results of the study by Sumer and Fredsøe (1996) showed that vortices forming at the head of the breakwater are the primary cause of erosion. In the present study it has been shown that a vortex forms as a

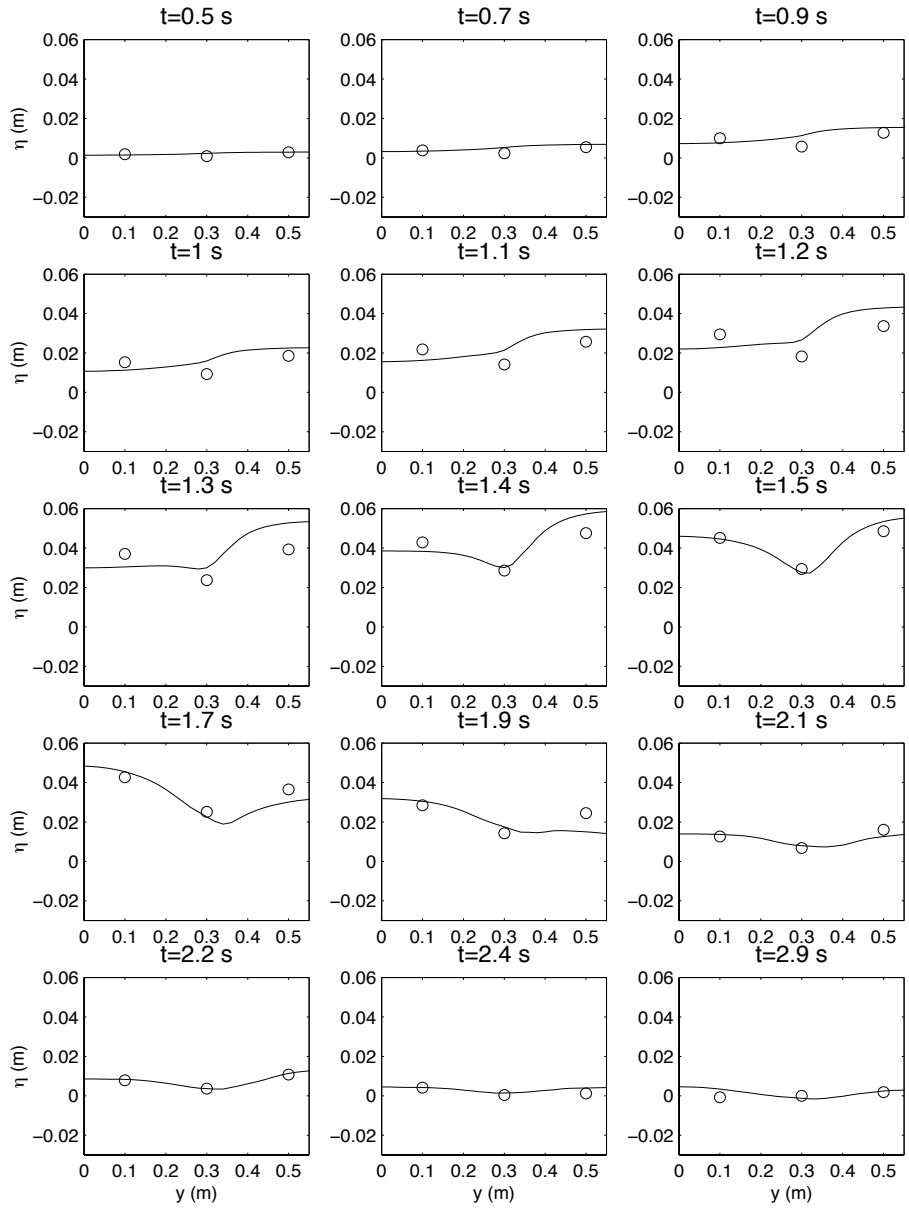


Figure 4.1: Profile of $\eta$ across the width of the tank. The circles represent experimental data points and the solid lines are from the model output.

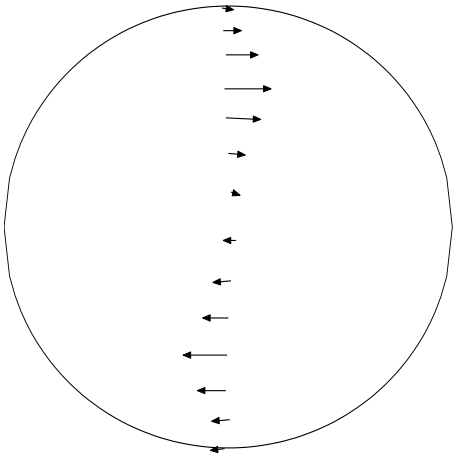

Figure 4.2: Schematic showing velocity magnitudes across a Rankine vortex.

result of unsteady flow past a breakwater at normal incidence. Plots of the model velocity vectors also show an increase in the velocities associated with the vortex corresponding to an increase in the wave height. It would be expected that a vortex with larger magnitude velocities would have a more significant erosional effect than a smaller vortex with reduced velocities. If a vortex persists in the generation region, significant erosional effects could result, depending upon the strength of the vortex, which could threaten the integrity of the structure.

In the work conducted by Perroud (1957) a vortex was generated by a solitary wave, nonuniform flow, past a vertical structure, however, he observed that the vortex persisted near the structure and was not immediately advected downstream. In the present study, as has been mentioned previously, the vortex generated from nonuniform flow past a structure was advected away. Further investigation is needed in order to understand the circumstances which determine whether or not the vortex will be advected downstream. One familiar example of flow past a structure producing a single shed vortex comes from the field of aerodynamics.

In aerodynamics it is well known that a steady flow past an airfoil, for a specific angle of incidence to the ambient flow direction, results in the generation of a vortex which is then shed from the airfoil. Figure 4.3 shows a sequence of images as the flow starts up past an airfoil. In Figure 4.3 (a) just after start-up the flow is irrotational and inviscid. A stagnation point occurs on the upper surface of the rear of the airfoil. This occurs theoretically and is not physically realizable. The flow cannot make the

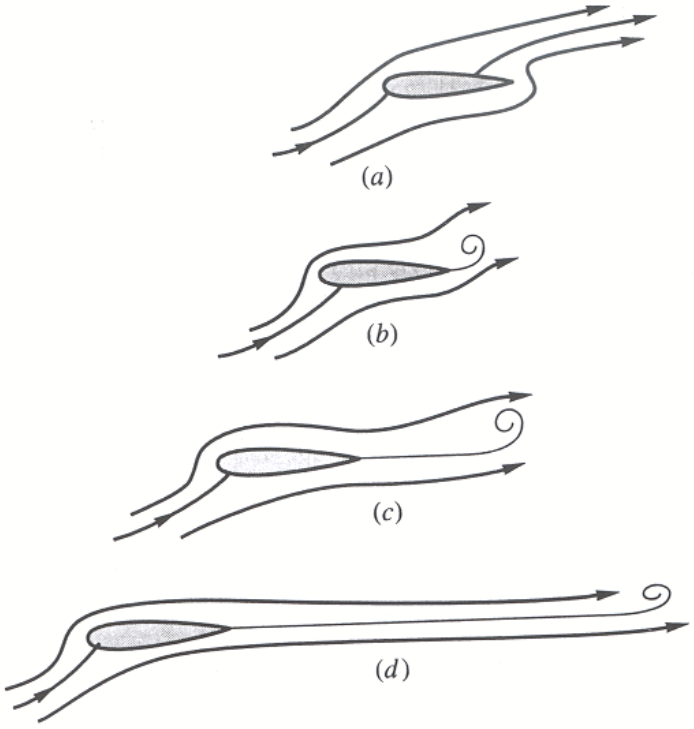


Figure 4.3: Steady flow past an airfoil (White, 1999).

sharp turn and separation occurs which causes a starting vortex to form (Figure 4.3 (b)). This starting vortex is shed and is advected downstream as shown in Figures 4.3 (c) and (d).

In order to adequately compare results from previous studies with the present study it is necessary to consider the differences in the model parameters used. The parameters from three studies are given in Table 4.1 and comparisons of nondimensionalized parameters from the same three studies are presented in Table 4.2. Further investigation is necessary to determine how these variables effect vortex propagation downstream.

In the experiments the depression (d) in $\eta$ occurring at the center of the vortex (scaled by the wave height), for the small wave height case, is approximately $d/H = 0.46$ for an $H/h = 0.18$. For the large wave height case the depression is approximately $d/H = 0.58$ of the incident wave height for an $H/h = 0.34$. Perroud (1957) estimated that the surface depression was approximately $d/H = 0.47$ of the incident wave height for an $H/h = 0.45$. Liu (1984) observed that a vortex formed during his experiments,

Table 4.1: Comparison of parameters used in three studies. $H$=incident wave height, $L$=wall length, $W$=tank width, $h$=fluid depth, $d$=surface depression at the center of the vortex.

| Study | $L$ (m) | $W$ (m) | $H$ (cm) | $h$ (m) | $d$ (m) |
|---|---|---|---|---|---|
| Perroud (1957) | .88-.62 | 1.12 | 2.7 | .061 | -.013 |
| Liu (1984) | 3.02 | 4.00 | .65-2.2 | .050-.052 | N/A |
| Present study (case 1) | .30 | .60 | 5.5 | .30 | -.025 |
| Present study (case 2) | .30 | .60 | 10.3 | .30 | -.060 |

Table 4.2: Comparison of nondimensionalized parameters for three studies. $H$=incident wave height, $L$=wall length, $W$=tank width, $h$=fluid depth, $d$=surface depression at the center of the vortex.

| Study | $H/h$ | $L/W$ | $d/H$ |
|---|---|---|---|
| Perroud (1957) | .58 | .78-.56 | -.47 |
| Liu (1984) | .13-.42 | .76 | N/A |
| Present study (case 1) | .18 | .50 | -.46 |
| Present study (case 2) | .34 | .50 | -.58 |

however, no measurement was given for the surface depression at the center of the vortex in that study. Based on this evidence, it is difficult to determine the relationship between the surface depression and the parameter $H/h$.

The reference to a surface depression is being used in the present study as a signature of the vortex location and as a reference for comparison with the model results. It is of interest to find that the numerical model predicts this depression in $\eta$ (despite the underprediction in magnitude) and that the surface depression is advected with the vortex as shown in Figures 3.6 and 3.7. The surface depression in the model data begins to dissipate over approximately 2 $s$ similar to what is observed in the experimental data. The prediction of this signature by the model is further verification of the model's ability to simulate the fluid motion that was observed in the experimental data.

From the model data it was illustrated, by contours of $\eta$ (Figure 3.4), that the vortex is identified by a surface depression, however, the magnitude of the deformation is underpredicted by the model. Figure 4.4 shows plots of $\eta$, from the model data,

for six time intervals to illustrate the evolution as well as the variability of the surface deformation that occurs as the vortex is being generated and advected downstream. The incident wave is just passing the vertical wall at $t = 4\ s$ and the vortex is being generated. The surface deformation is greatest as the vortex is being generated. After the wave has moved past the breakwater, the vortex is shed from the structure and begins to propagate downstream ($t = 4.4 - 5.6\ s$). The signature of the surface depression dissipates more rapidly (approximately 0.5 $s$) in the model than in the experimental data (2.0 $s$) for the small wave height case. The vortex itself persists for several minutes in the model results and this is similar to what was observed in the experimental data.

Figure 4.5 shows the trajectories for the vorticies formed in both the experiments and the model for the small wave height case. Each trajectory was generated by estimating the center position of the vortex from contour plots of surface elevation at selected time steps. Although vortex formation and advection are predicted by the model, this figure shows the temporal and spatial differences between the model and experimental data, for the process of vortex formation and advection. The vortex formed in the model travels farther and more rapidly downstream than in the experiments and does not travel far in the increasing $y$ direction. The vortex generated in the experiments traveled in the increasing $y$ direction and impacted on the side wall and began to travel downstream.

## 4.3 Circulation

As described previously in the methods chapter, in order to have vortex formation as well as advection from the structure it is necessary to be able to simulate flow separation. In addition, the form of the advective acceleration must be of the form

$$(\vec{u} \cdot \nabla)\vec{u} \tag{4.1}$$

rather than

$$\frac{1}{2}\nabla(\vec{u} \cdot \vec{u}) \tag{4.2}$$

If the latter form is used then there will be no advection and if, additionally,

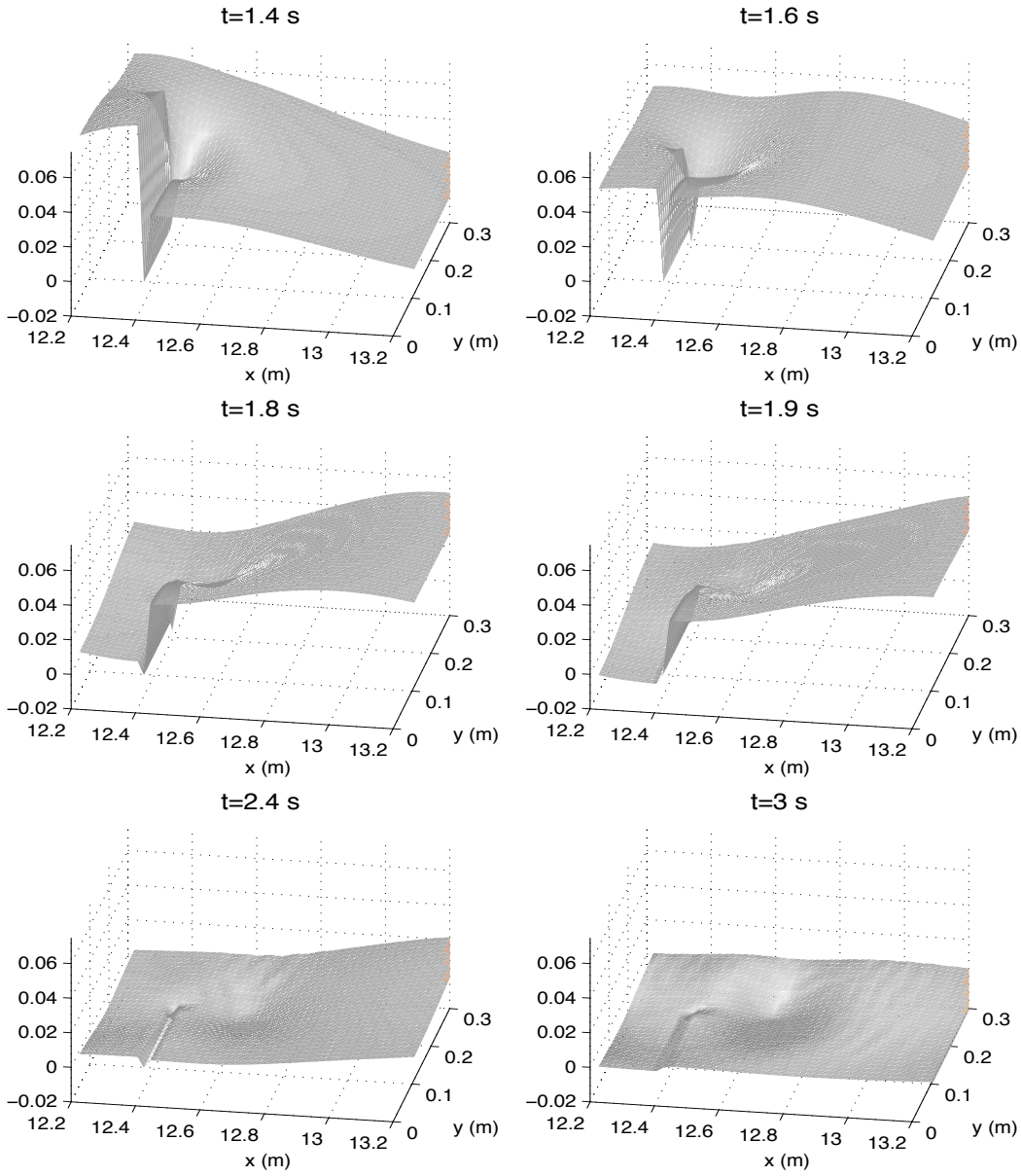


Figure 4.4: $\eta$ surface from the model data for 6 time steps showing the evolution of the surface depression as a vortex develops.

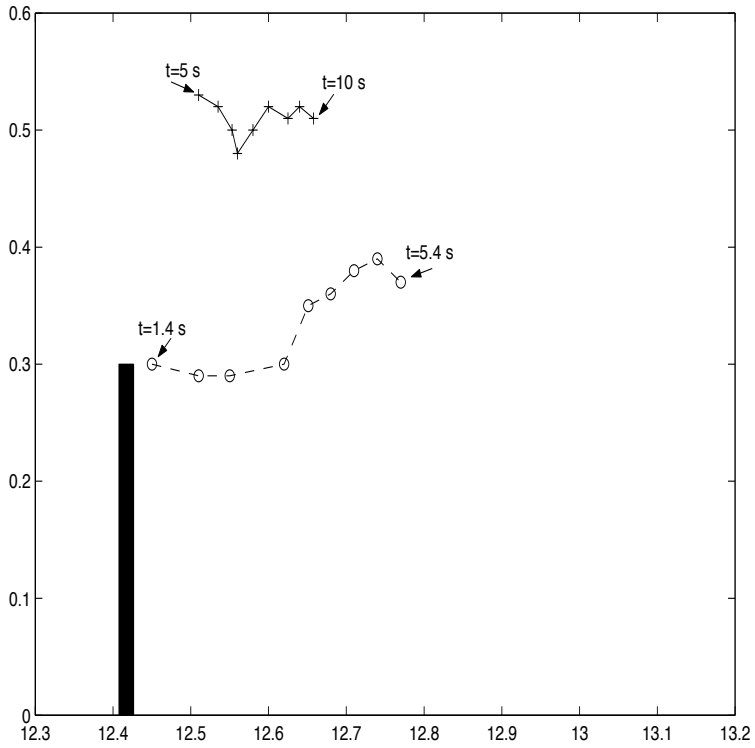


Figure 4.5: Comparison of the trajectories of vorticies generated in the experiments (solid line) and in the model (dashed line) for $H = 5.48\ cm$.

there is no eddy viscosity flow separation will not occur to provide a source for the vorticity. To verify this theory using the numerical model, the total circulation was calculated for both forms of the advective acceleration. The total circulation is defined as the line integral of the tangential velocity along any closed contour curve s,

$$\Gamma = \oint \vec{u} \cdot \vec{ds} \tag{4.3}$$

Most of the model domain was used as the control volume for the computation as shown by the arrows in Figure 4.6 (a). The positive direction used for the computation was chosen, following convention, to be counter-clockwise. For the first case Figure 4.6 (b) the form of the advective acceleration used was

$$\frac{1}{2}\nabla(\vec{u} \cdot \vec{u}) \tag{4.4}$$

and no source term for the vorticity. The flow in this case is irrotational. For the

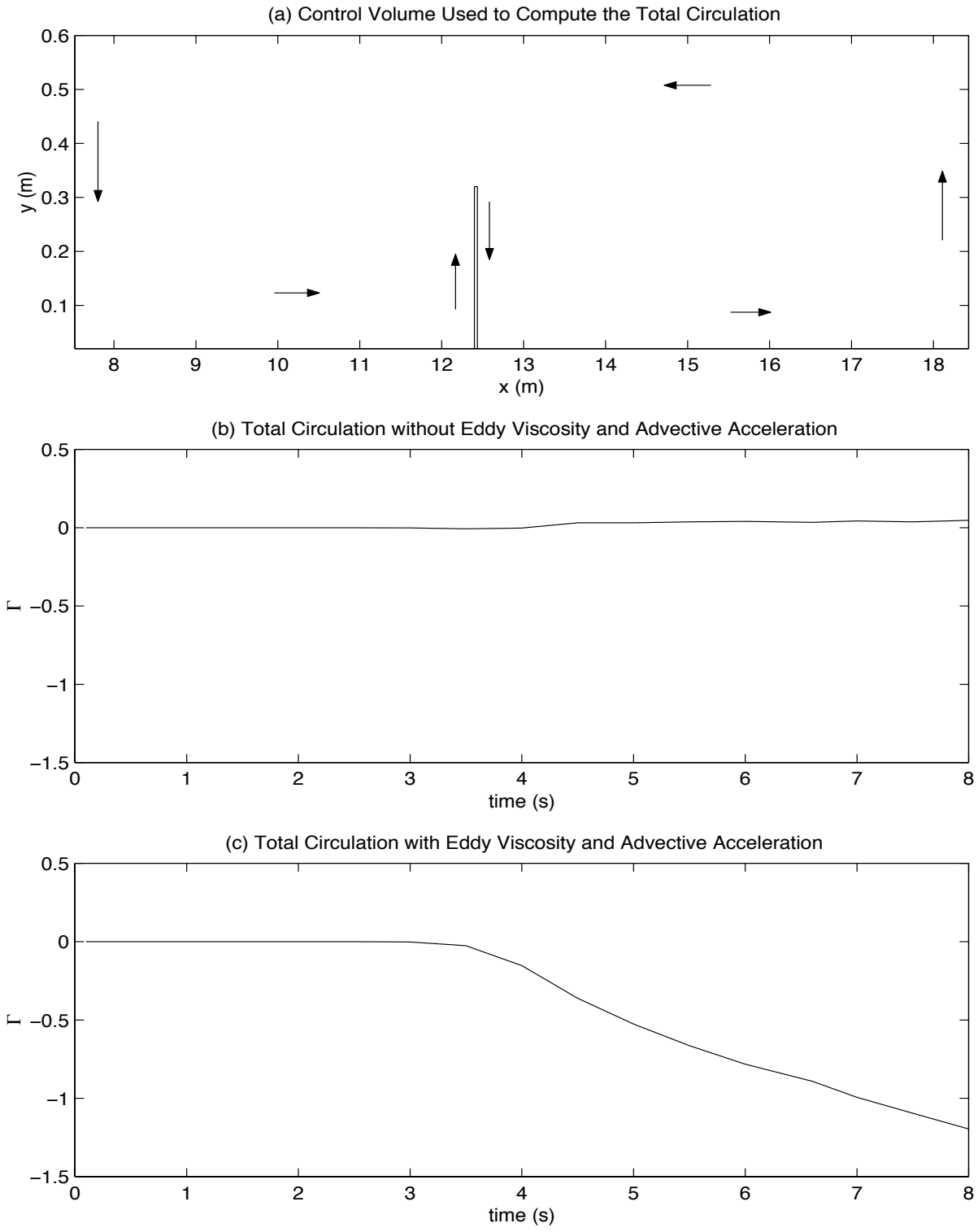


Figure 4.6: (a) Control volume used for computation of Γ, (b) Γ for the potential flow case, (c) Γ for the nonpotential flow case

second case Figure 4.6 (c) the form of the advective acceleration used was

$$(\vec{u} \cdot \nabla)\vec{u} \tag{4.5}$$

and eddy viscosity was included so in this case the fluid has vorticity. For the irrotational case the total circulation theoretically should be zero for all time. And in the figure it is nearly zero with a small increase occurring around $t = 4\ s$ due to numerical error. For the second case, the fluid is not irrotational, there is a net negative circulation. This makes sense because the positive direction for the computation of the total circulation was chosen to be counter-clockwise and the vortex which forms has a clockwise rotation so the total circulation should become negative over time for this case and this is in fact the result. If the vortex was shed and did not propagate downstream and was small in diameter so that it's presence did not effect a large portion of the fluid domain then the total circulation would be expected to become negative and reach some maximum value and then begin to decrease over time as the intensity of the vortex dissipates over time. However, in this case the vortex is shed and is then advected downstream. So over time more of the fluid in the model domain becomes effected and so the total circulation continues to decrease with time. The intensity of the vortex itself is decreasing with time, however, over the entire control volume more of the fluid becomes rotational. If the model simulation were continued eventually the vortex would spin down to the extent that the surrounding fluid motion would also decrease and the a maximum of the total circulation would have been reached.

Illustrations of how the flow fields in these two cases differ is shown in Figures 4.7 and 4.8. The velocity vector field for four time steps is shown in Figure 4.7. No vortex forms over time in this case. In Figure 4.8 velocity vectors for the same four time steps shows that in this case the vortex is formed and is advected.

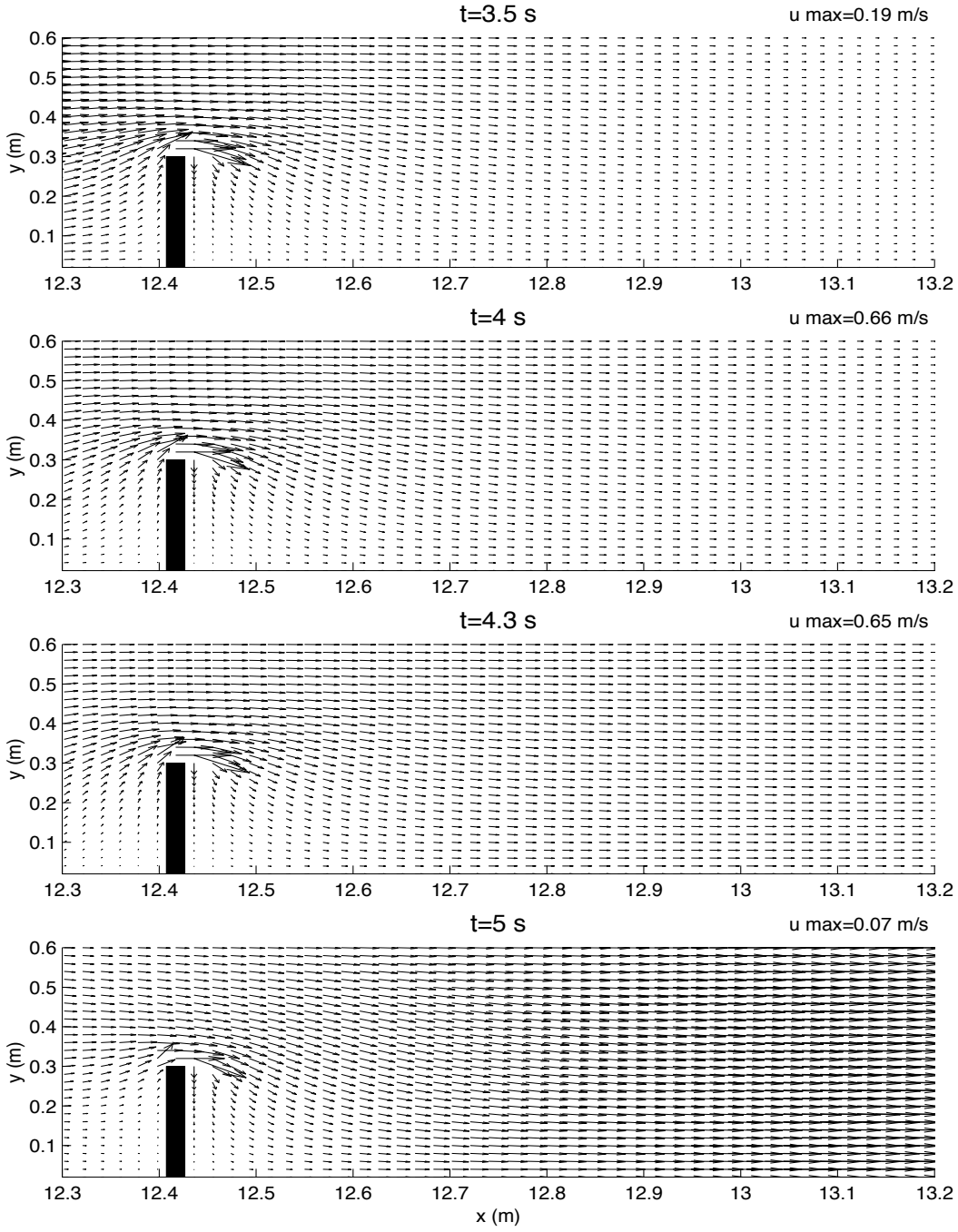


Figure 4.7: Flow fields for the potential flow case showing that no vortex forms.

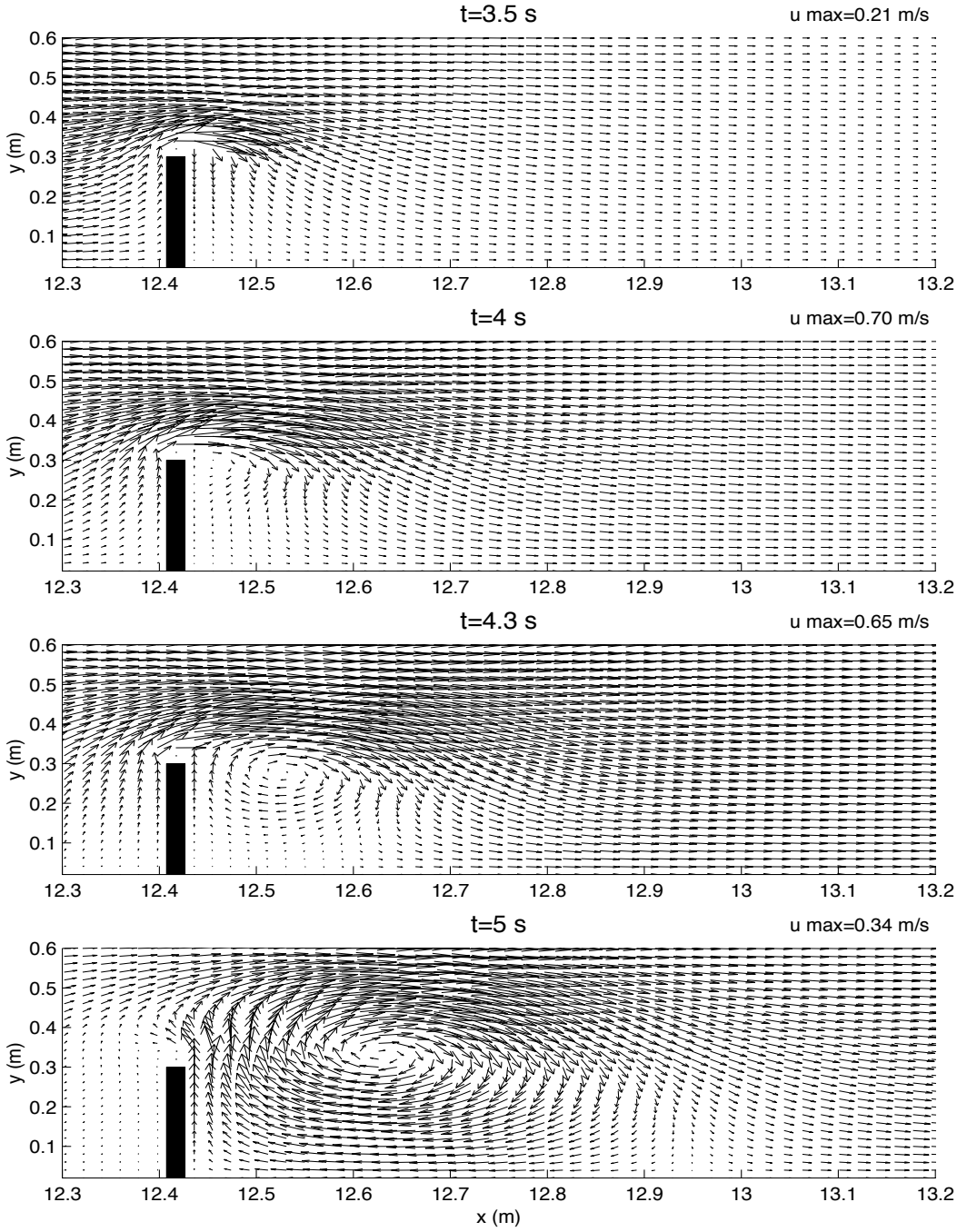


Figure 4.8: Flow fields for the non-potential flow case showing that a vortex forms and is advected downstream.

# Chapter 5

# CONCLUSIONS

The interaction of a single solitary wave with a vertical wall is studied. It is shown using both numerical model results and experimental results that a single vortex forms which persists for some time. The vortex, once formed, is shed and subsequently advected from the structure and propagates downstream. Two cases are considered, a small wave height case, $H = 5.48\ cm$ and a large wave height case, $H = 10.3\ cm$.

Surface elevations for both wave heights are predicted by the model to be fairly close to the experimental data and the prediction improves significantly a small distance from the structure.

It was found that in order for vortex formation and advection from the structure to occur, it is necessary to have a source of the vorticity, and in this study eddy viscosity was included which allowed the fluid to separate as it flowed past a sharp corner. The source of vorticity comes from the occurrence of fluid separation. Additionally, it is necessary to have the advective acceleration in the form

$$(\vec{u} \cdot \nabla)\vec{u} \tag{5.1}$$

rather than in the form

$$\frac{1}{2}\nabla(\vec{u} \cdot \vec{u}) \tag{5.2}$$

To derive the vorticity of the fluid the curl of the momentum equations is calculated. If the acceleration term has the form given by equation 5.1 then the curl of this term gives rise to advection of vorticity. If the acceleration term is of the form in

equation 5.2, the curl of this term is zero, therefore, no advection of vorticity arises.

From contours of surface elevations and from plots of the vortex trajectories for the small wave height case it was shown that vortex formation and advection occurs in the model, however, this process is temporally and spatially offset compared with the experimental data. It was observed that a surface depression forms, located at the center of the vortex, and persists for approximately the same length of time in both the model and experimental data, however, the model underpredicts the magnitude of the surface depression observed in the experimental data.

Verification of the model, showing that the potential flow case was in fact irrotational, was determined by computing the total circulation of the fluid in the model domain. For the potential flow case the total circulation should theoretically be zero for all time and in the model results it was shown that the total circulation has a near zero value over time (the deviation from zero due possibly to numerical error). For the rotational flow case the total circulation has a net negative value over time. A maximum negative value would be expected for a wave flume with an infinite length but in this study the wave flume had a finite length, so the solitary wave reflected off of the end of the tank and propagated back through the model domain before a maximum value could be reached in the data.

In the present study it was observed that the vortex, once formed, is advected downstream of the structure. Previous studies do not consistently report that a vortex which is shed from the structure is also advected. In order to predict whether advection of the vortex would in fact occur this process needs to be compared with previous studies to try to determine the factors necessary.

It was suggested that the persistence of the vortex in the same location as well as the strength of the vortex would have an effect on the erosional processes near the structure so this is an important aspect of this study and would be worthy of further consideration. It was observed, principally from the model data, that the strength of the vortex was greatest during initial formation and decreases as the vortex is shed from the structure and propagates downstream. Energy losses from the solitary wave due to vortex formation need to be determined in order to more accurately estimate erosional effects. In order to carry out an energy analysis, measurements of the velocities within the vortex are necessary.

# REFERENCES


Abbott, M.B., A.D. McCowan, and I.R. Warren (1984). "Accuracy of short-wave numerical model." *J. Hydr.. Eng.*, 110, 1287-1301.

Chan, R.K.-C., and Robert L. Street (1970). "A Computer study of finite-amplitude water waves." *J. Comp. Phys.*, 6, 68-94.

Chen, Q., R.A. Dalrymple, J.T. Kirby, A.B. Kennedy, and M.C. Haller (1999). "Boussinesq modeling of a rip current system." *J. Geophys. Res.*, 104(C9), 20,617-20,637.

Gobbi, M.F., J.T. Kirby, and A.B. Kennedy (2000). "On the consistency of Boussinesq models and their ability to predict vertical vorticity fields." In *Proc. 27th Int. Conf. of Coast. Eng.* , Sydney, Australia.

Goring, D.G. (1978). "Tsunamis: the propagation of long waves onto a shelf". Phd. Dissertation, California Institute of Technology.

Hommel, D., F. Shi, J.T. Kirby, R.A. Dalrymple, and Q. Chen (2000). "On the consistency of Boussinesq models and their ability to predict vertical vorticity fields." In *Proc. 27th Int. Conf. of Coast. Eng.* , Sydney, Australia.

Liu, P.,L.-F. (1984) "Diffraction of solitary waves." *J. Wtrwy. , Port , Coast. and Oc. Engrg.*, 110(2), 201-214.

Madsen, P.A., R. Murray, and O.R. Sorensen (1991) "A new form of the Boussinesq equations with improved linear dispersion characteristics." *Coastal Engrg.* , 15, 371-388.

Madsen, P.A. and H.A. Schäffer (1999). "A review of Boussinesq-type equations for surface gravity waves." in *Advances in Coastal and Ocean Engineering.*, World Scientific, Vol. 5, 1-94.

Mei, C.C. (1983). "The Applied Dynamics of Ocean Surface Waves.", John Wiley, New York, pp 740.

Mei, C.C. and B. Méhauté (1966). "Notes on the equations of long waves over an uneven bottom." *J. Geophys. Res.*, 71(2), 393-400.

Nwogu, O. (1993). "An alternative form of the Boussinesq equations for nearshore wave propagation." *J. Wtrwy. Port Coast. and Oc. Engrg.*, 119(6), 618-638.

Peregrine, D.H. (1967). "Long waves on a beach." *J. Fluid Mech.*, 27(4), 815-827.

Perroud P.H. (1957). "The solitary wave reflection along a straight vertical wall at oblique incidence." *Technical Report Series 99, Issue 3, Institute of Engineering Reserach, University of California, Berkeley*, 93.

Roddier D. and R.C. Ertekin (1999). "Diffraction and remodelization of solitons around a false wall." *Chaos Sol. Frac.* , 10(7), 1221-1240.

Shi, F., R.A. Dalrymple, J.T.Kirby, Qin Chen, and Andrew Kennedy (2000). "A fully nonlinear boussinesq model in generalized curvilinear coordinates." Submitted manuscript.

Sumer B.M. and J. Fredsøe (1996). "Scour at the head of a vertical-wall breakwater." *Coastal Eng.*, 29, 201-230.

Wang, K.-H. (1993) "Diffraction of solitary waves by breakwaters." *J. Wtrwy. Port Coast. and Oc. Engrg.*, 119(1), 49-59.

Wei, G. and J.T. Kirby (1995). "Time-dependent numerical code for extended boussinesq equations." *J. Wtrwy. Port Coast. and Oc. Engrg.*, 125(5), 251-261.

Wei, G., J.T. Kirby, S.T. Grilli, and R. Subramanya (1995). "Time-dependent numerical code for extended boussinesq equations." *J. Wtrwy. Port Coast. and Oc. Engrg.*, 125(5), 251-261.

White, F. (1999). "Fluid Mechanics". WCB McGraw-Hill, pp 826.

Witting, J.M. (1984). "A unified model for the evolution of nonlinear water waves." *J. Comp. , Phys.* , 56(2), 203-236.

Wu, T.Y. (1981). "Long waves in ocean and coastal waters." *J. Eng. , Mech.* , ASCE, 107, No.EM3, 501-522.

# Appendix A

# Time series of $\eta$ from wave gages on the moving carriage for the small wave height case

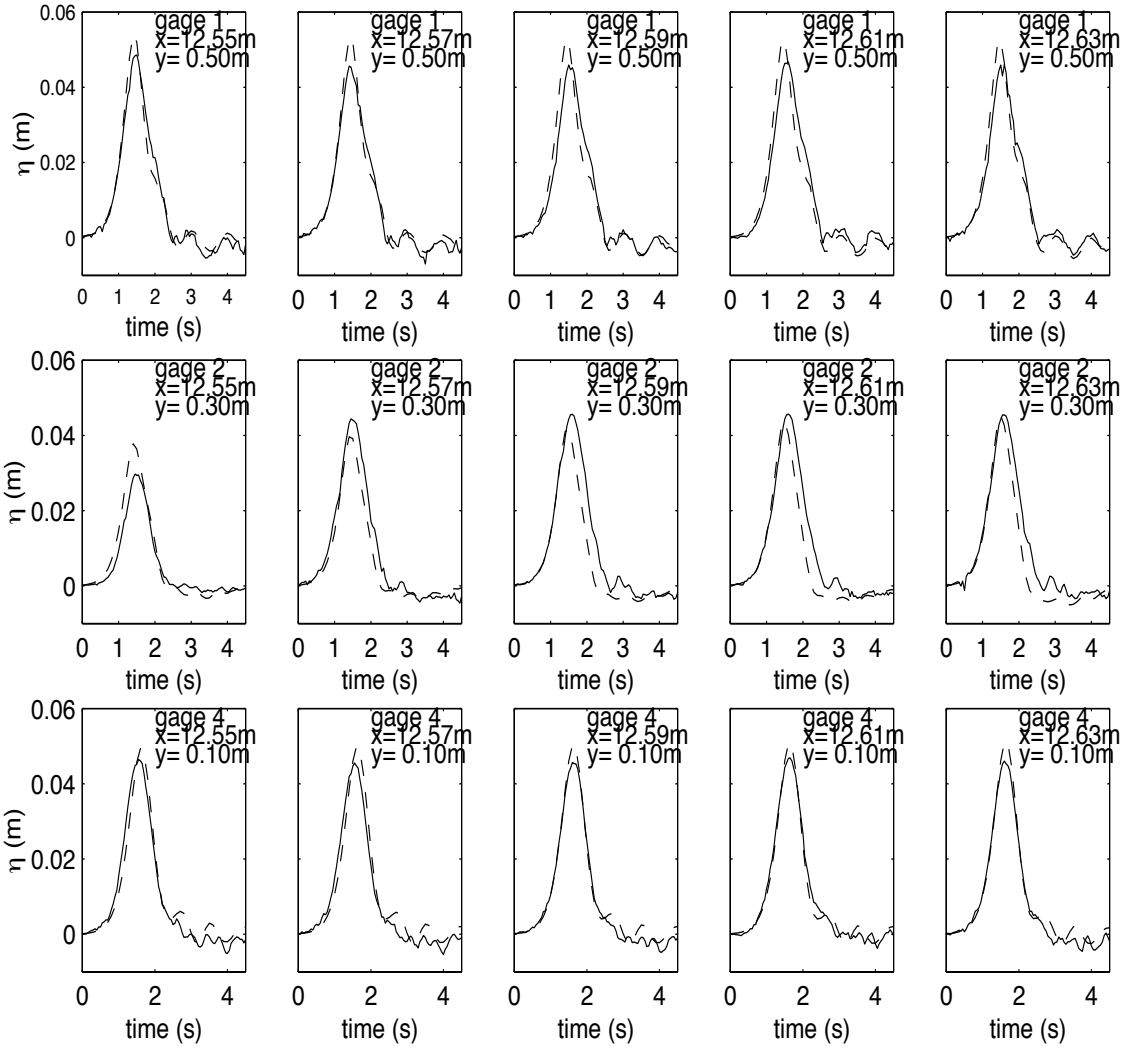


Figure A.1: Time series of surface elevations for $x = 12.53 - 12.63\ m$ and $H = 5.48\ cm$. The solid line is the experimental data and the dashed line is model results.

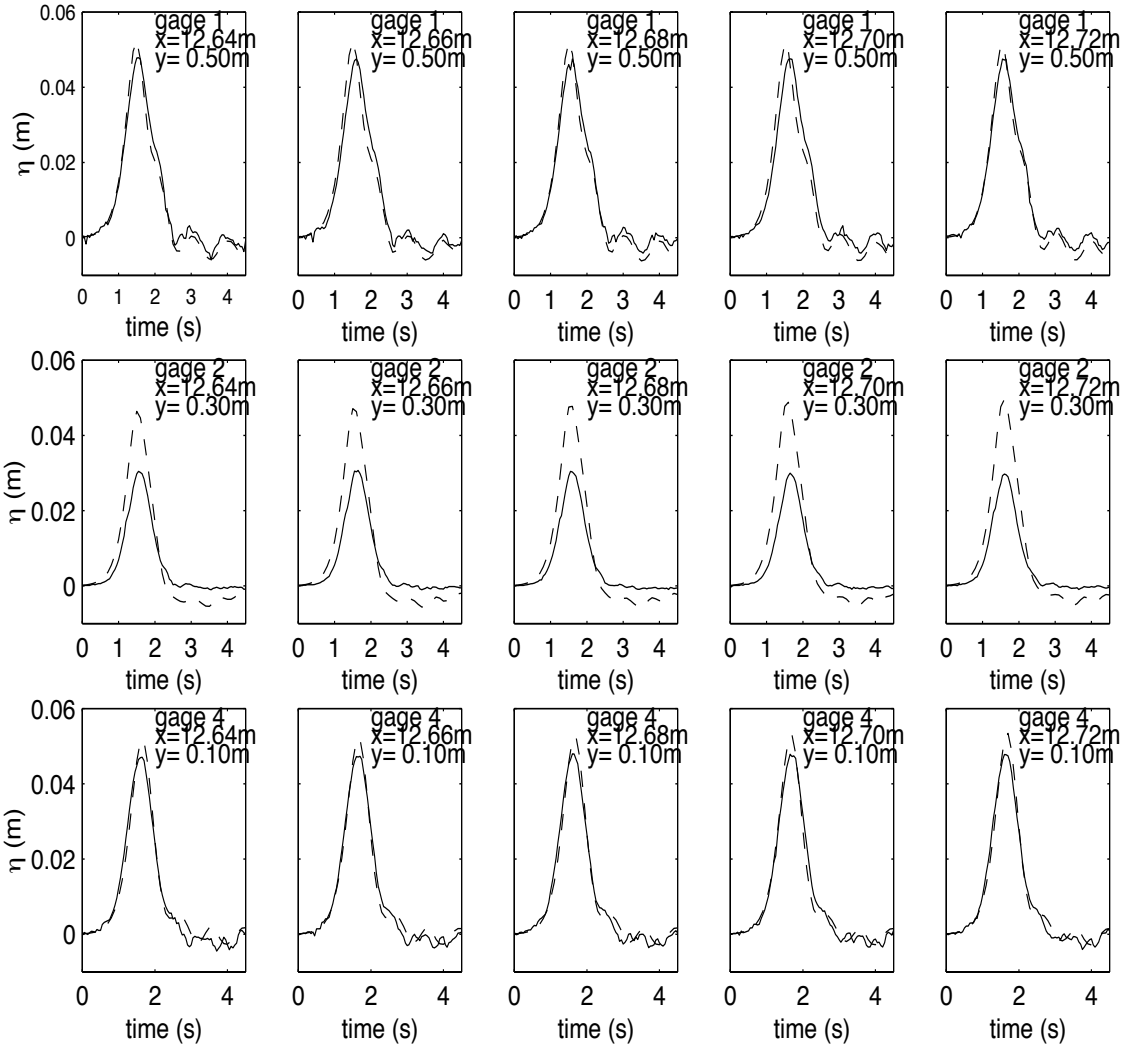


Figure A.2: Time series of surface elevations for $x = 12.64 - 12.72\ m$ and $H = 5.48\ cm$. The solid line is the experimental data and the dashed line is model results.

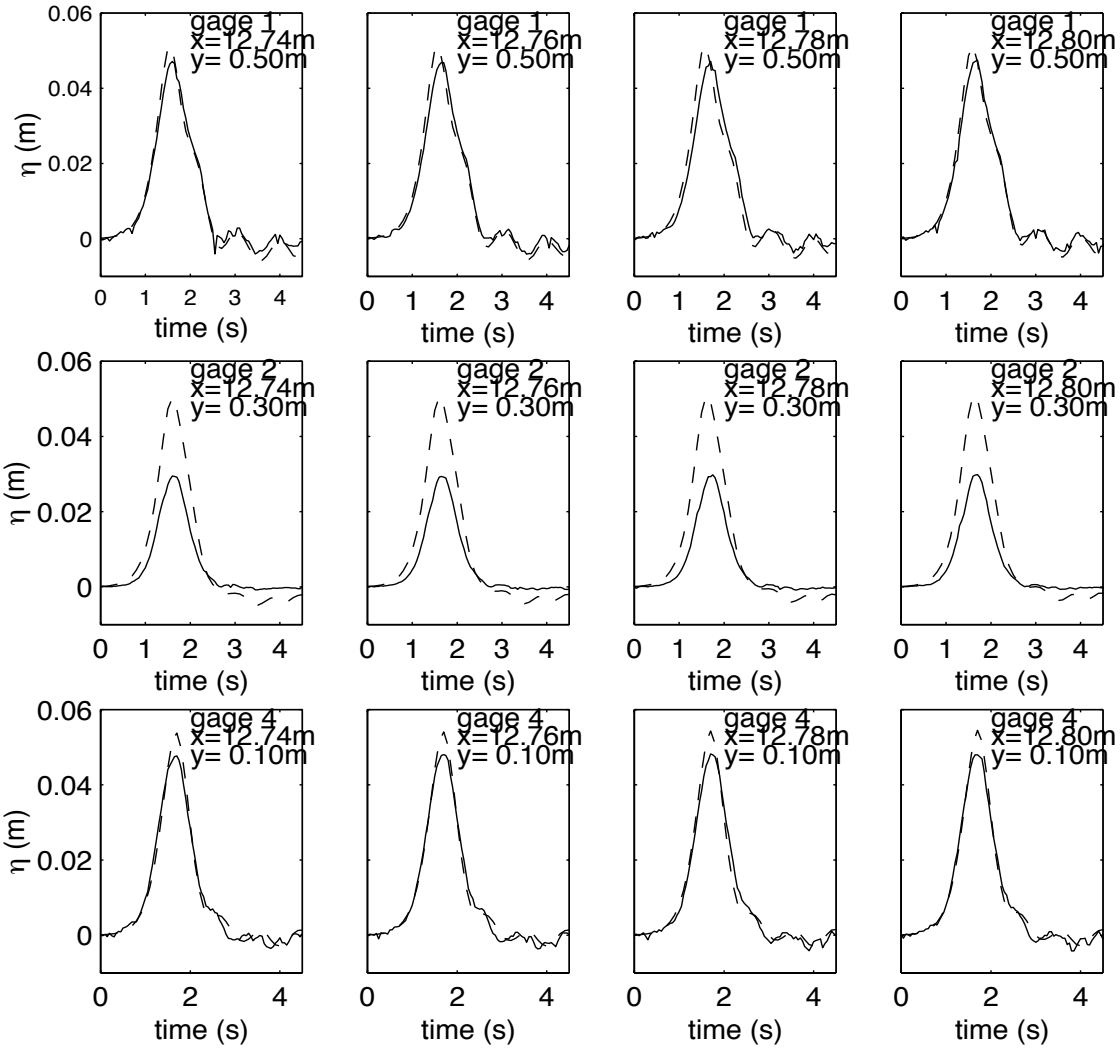


Figure A.3: Time series of surface elevations for $x = 12.74 - 12.80\ m$ and $H = 5.48\ cm$. The solid line is the experimental data and the dashed line is model results.

# Appendix B

# Time series of $\eta$ from gages on the moving carriage for the large wave height case

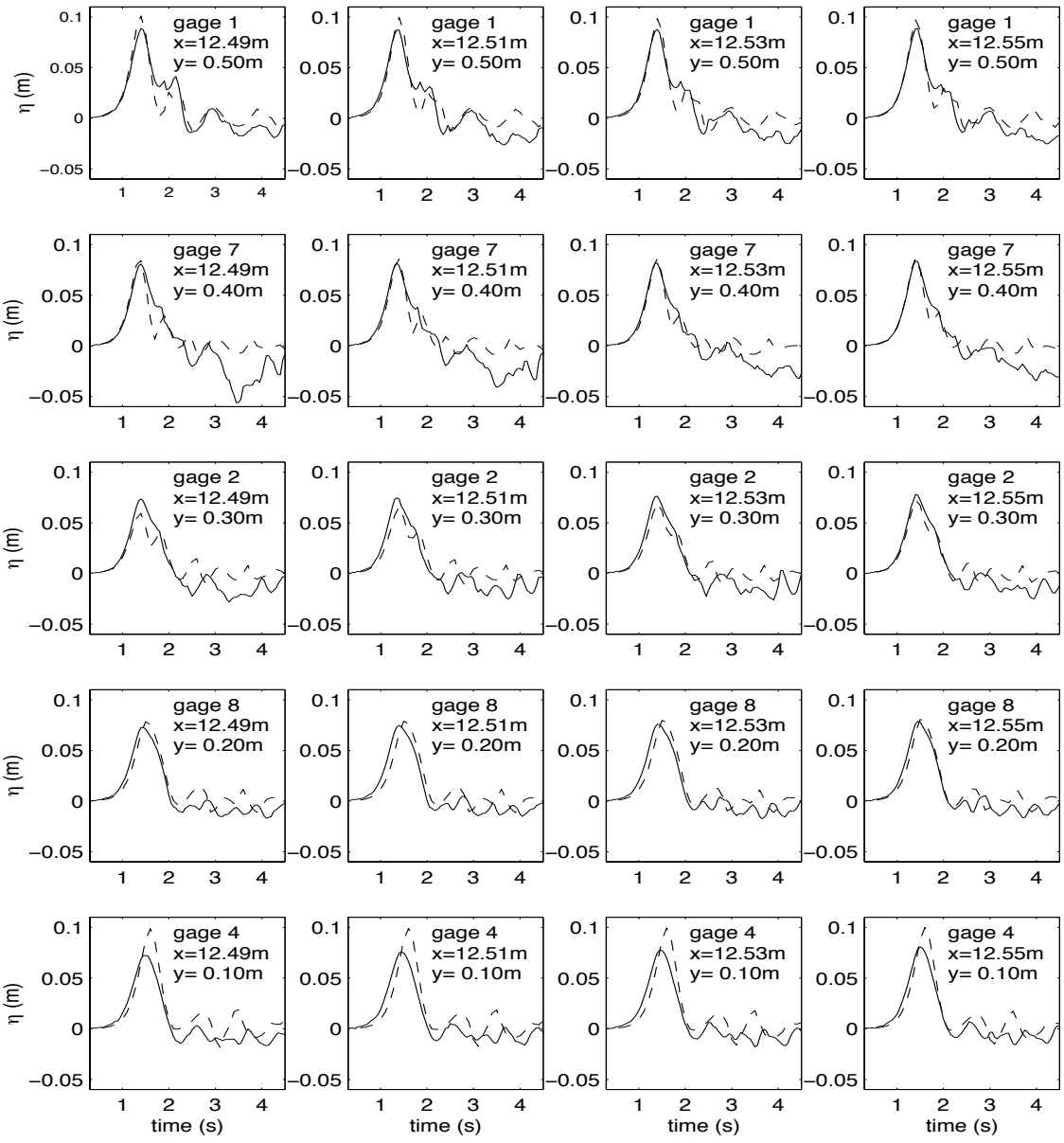


Figure B.1: Time series of surface elevations for $x = 12.49 - 12.55\, m$ and $H = 10.3\, cm$. The solid line is the experimental data and the dashed line is model results.

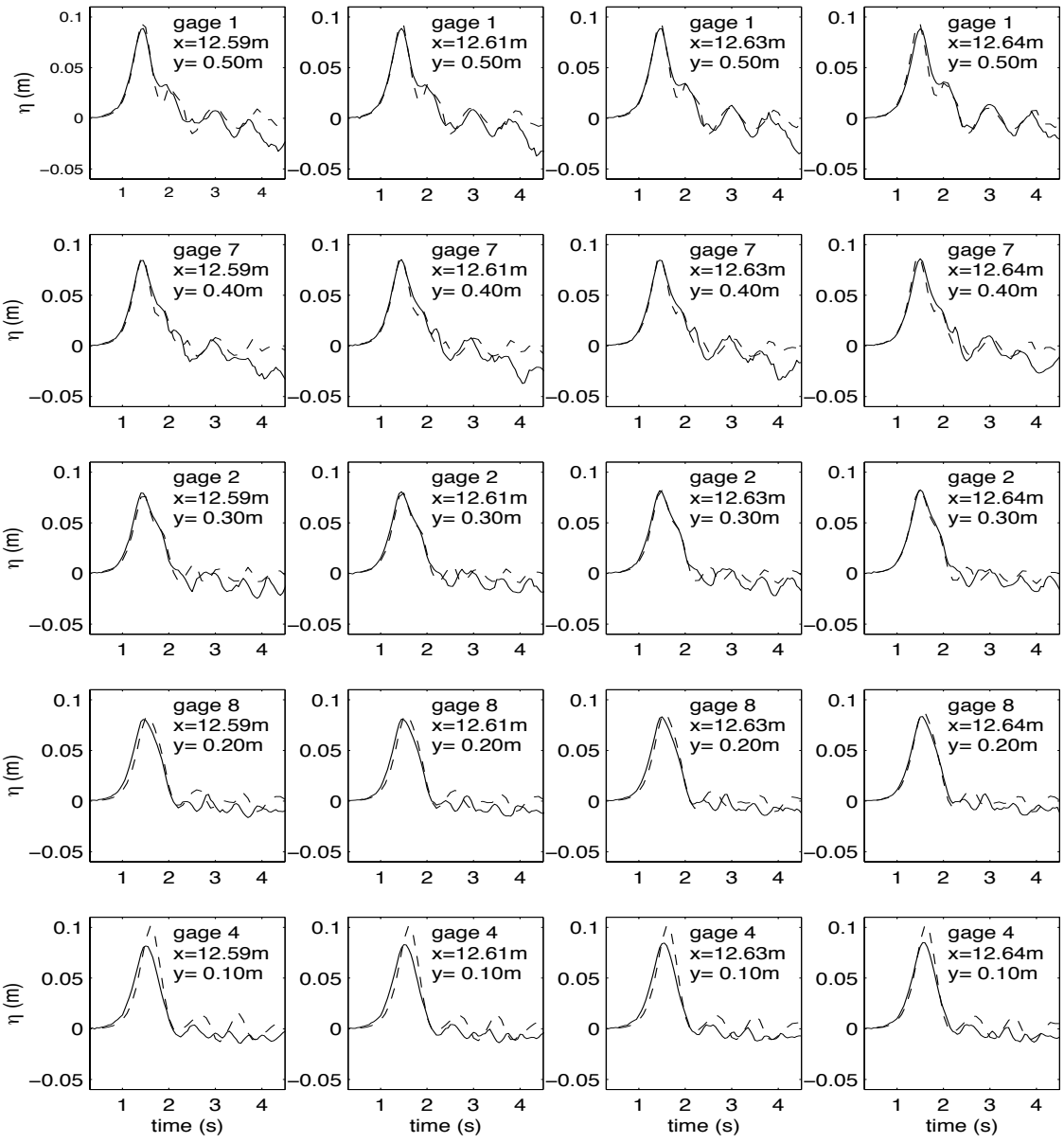


Figure B.2: Time series of surface elevations for $x = 12.59 - 12.64\,m$ and $H = 10.3\,cm$. The solid line is the experimental data and the dashed line is model results.

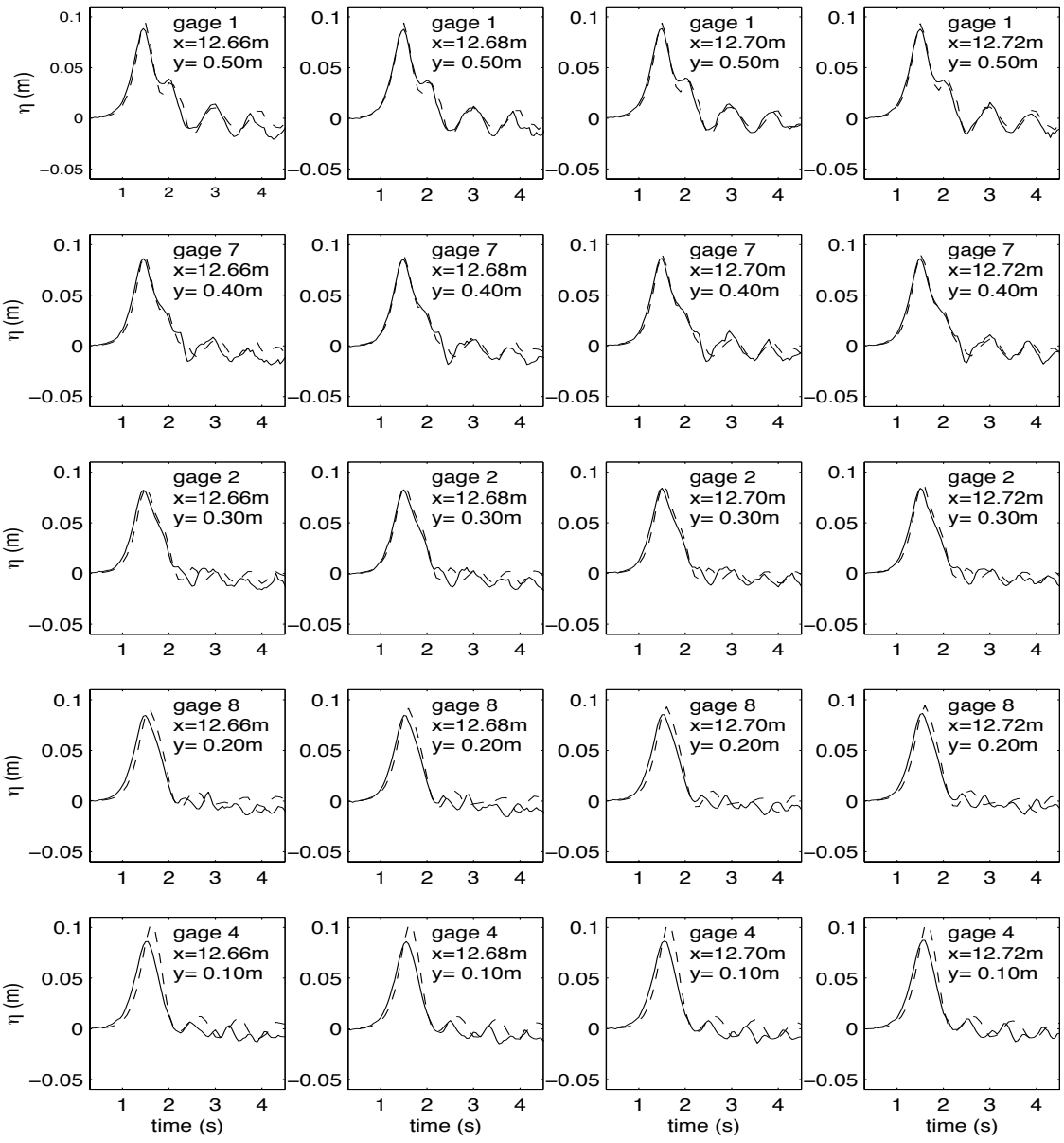


Figure B.3: Time series of surface elevations for $x = 12.66 - 12.72\,m$ and $H = 10.3\,cm$. The solid line is the experimental data and the dashed line is model results.

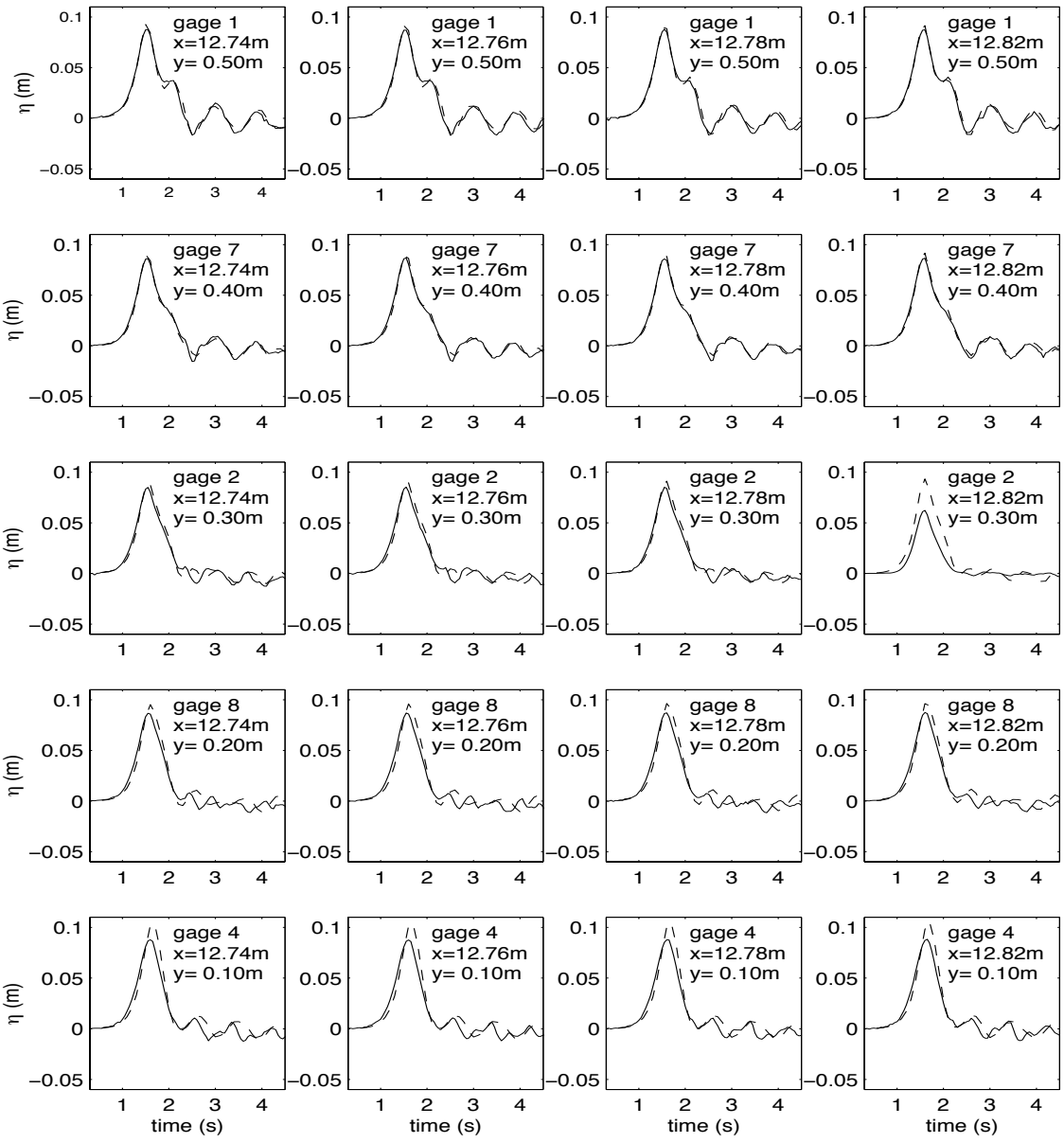


Figure B.4: Time series of surface elevations for $x = 12.74 - 12.82\,m$ and $H = 10.3\,cm$. The solid line is the experimental data and the dashed line is model results.